X, W

DEUTSCHES ELEKTRONEN-SYNCHROTRON

DESY

DESY-THESIS-1998-035
WUB-DIS 98-12
November 1998

$b\bar{b}$ Bound States in Lattice QCD with Dynamical Fermions

by

A. Spitz

ISSN 1435-8085

NOTKESTRASSE 85 - 22607 HAMBURG

To be sure that your reports and preprints are promptly included in the HEP literature database
send them to (if possible by air mail):

DESY
Zentralbibliothek
Notkestraße 85
22603 Hamburg
Germany

DESY
Bibliothek
Platanenallee 6
15738 Zeuthen
Germany

FACHBEREICH PHYSIK
BERGISCHE UNIVERSITÄT
GESAMTHOCHSCHULE WUPPERTAL

$b\bar{b}$ Bound States in Lattice QCD with Dynamical Fermions

Dissertation
zur Erlangung des Doktorgrades
des Fachbereichs Physik
der Bergischen Universität-Gesamthochschule Wuppertal

vorgelegt von

Achim Spitz

aus Neustadt/Wied

WUB-DIS 98-12

September 1998

Für Nuschin

Drei Jahr ist eine kurze Zeit,
Und, Gott! das Feld ist gar zu weit.
Wenn man einen Fingerzeig nur hat,
Läßt sich's schon eher weiter fühlen.

Schüler, in J.W. von Goethe, 'Faust Teil 1'

Abstract

We calculate the bottomonium spectrum in the framework of non-relativistic Lattice QCD beyond the quenched approximation. The NRQCD Lagrangian includes spin-independent interactions of order $m_b v^2$ and $m_b v^4$ as well as spin-dependent terms up to order $m_b v^6$, where m_b is the b-quark mass and v its average velocity. Propagators are evaluated on gauge configurations with two degenerate flavours of dynamical Wilson fermions which naturally may be identified with the up and down quarks. We use lattices of extent $16^3 \times 32$ at $\beta = 5.6$ corresponding to a resolution of somewhat less than 0.1 fm and a box size of approximately 1.4 fm. The analysis includes samples at three values of the sea-quark mass ranging from $m_s/2$ to m_s, m_s being the mass of the strange quark.

We extract ground states and radial excitations for S- and P-wave mesons employing potential model wave functions in the smearing procedure. The light quark mass dependence of radial and spin splittings is studied and we perform 'chiral' extrapolations to $m_s/3$. Our strategy in studying sea-quark effects is to compare the extrapolated results with those obtained from a quenched simulation at equal lattice spacing. Our quenched data for the gross level structure is in clear disagreement with the experimental spectrum which confirms previous studies. Switching on dynamical quarks shifts the data points closer to experiment. The effect is however rather small, so that the accuracy does not suffice to 'measure' the number of active flavours in the sea that enter Υ dynamics. Compared to an earlier NRQCD simulation of bottomonium using staggered dynamical configurations we have managed to reduce the statistical error on spin splittings substantially which permits us to detect very small vacuum polarisation effects. We find that spin splittings remain unaffected by the inclusion of dynamical quarks within errors of a few MeV.

Based on the spectrum results we estimate the strong coupling constant in full QCD from the perturbative expansion of the plaquette in the coupling α_P. We obtain disparate α_P values from the 1P-1S and 2S-1S splittings. They approach each other in the $n_f = 2$ theory and fully merge after extrapolation to three flavours. Conversion to the $\overline{\text{MS}}$-scheme and subsequent evolution to the Z mass scale yield $\alpha^{(5)}_{\overline{\text{MS}}}(m_Z) = 0.1118(26)$.

Contents

Chapter 1

Introduction

QCD colour dynamics is very peculiar. The interaction of two colour charges approaches the Coulomb law at short distances with a weak coupling constant as a consequence of the one gluon exchange. At larger distances, the gluon starts branching, which leads to a remarkable and totally counterintuitive phenomenon known as anti-screening [1, 2, 3]. This behaviour carries the seed of another outstanding property of Quantum Chromodynamics (QCD): when the distance becomes comparable to a certain scale, the branchings of gluons become so intensive that it makes no sense to speak of individual gluons. Rather, an adequate terminology is that of chromoelectric and chromomagnetic fields. It is conjectured that a specific organisation of the QCD vacuum squeezes the chromoelectric field into flux tubes — thus a dual Meissner effect would ensure colour confinement, which provides a dynamical explanation of the experimentally well established fact that neither quarks nor gluons are asymptotic states [4, 5].

Because of asymptotic freedom, the quark-gluon interaction is accessible to perturbative methods in the high energy domain, where one can successfully calculate the cross-sections of many short distance processes. The original, and perhaps one of the most powerful tests of QCD is the breaking of Bjorken scaling in deep inelastic lepton-hadron scattering [6]. However, perturbation theory does not apply at the confinement scale due to the increase of the coupling. To some extent this also spoils predictions of hard scattering processes that have to be connected to initial and final state hadrons. Thus the infra-red behaviour of QCD prevents us from testing the theory to a precision that is achieved in the electroweak sector. Even worse, one may consider it embarrassing that we are still not able to decide whether the observed spectrum of hadronic bound states can indeed be deduced from QCD.

As a consequence, much effort has been put into the development of adequate non-perturbative calculation tools. Quite recently, a breakthrough was achieved in understanding the infra-red dynamics in a theory which might be considered a relative of QCD: in $N = 2$ supersymmetric Yang-Mills theory it was analytically shown that magnetic monopoles do condense in the strong coupling regime, thus providing the basis for the dual superconducter scenario [7, 8]. In QCD, the method of sum rules (Shifman-Vainshtein-Zakharov sum rules) attempts to connect the strongly and weakly interacting sectors by expansion of correlation functions in the vacuum condensates and subsequent matching via dispersion relations [9, 10, 11]. Application of sum rules, however, involves the introduction of various approximations and heuristic procedures that are motivated by an intuition of the underlying physics and are not always rigorous consequences of QCD. The implications of symmetry have been successfully formulated in the effective field theory language both in the limit of small quark masses, where the dynamics of the Goldstone bosons is solely determined by chiral symmetry, as well as in the heavy quark regime. But to improve accuracy one has to cope with an increasing number of new

parameters (the low energy constants in Chiral Perturbation Theory [12, 13, 14]) which limit the predictive power to some extent.

The formulation of QCD on a space-time grid is free of any uncontrolled approximations and heuristic assumptions. Since Wilson's seminal paper in 1974 [15], Lattice Gauge Theory (LGT) has grown into a powerful computational tool which promises – with time – to produce the most accurate results for a significant part of hadronic observables. The lattice approach is remarkable in that it preserves local gauge invariance but abandons Poincaré invariance, which is only restored in the continuum limit. Asymptotic freedom provides a candidate ultraviolet fixed point at $g = 0$, g being the bare lattice coupling, and thus yields the possibility of such a limit. Indeed, for $SU(2)$ and $SU(3)$ gauge groups (with Wilson's action) in four dimensions there is much evidence for the absence of any bulk phase transition and it is widely believed that at weak coupling, a continuum limit with static quark confinement exists as a consequence of the analytic continuation of confinement at strong couplings.

The standard approach in LGT starts off with the Euclidean path integral and regularises it on (mostly) hypercubic lattices of some extent, L and spacing, a [1]. The functional integrals become finite dimensional partition functions of a statistical mechanics system and may be numerically computed by well established Monte Carlo techniques. This implies the sampling of field configurations according to the path integral measure and the subsequent estimation of operator expectation values by sample averages. Because of the procedure's stochastic nature, predictions carry statistical errors and become more precise with increasing sample size. Clearly, in order for a simulation result to be of relevance for continuum physics, the volume has to be large compared to the typical size of the system under investigation and the lattice spacing must be small enough to resolve the important physical length scales.

In recent years, improving the approach to the continuum limit has been at the center of theoretical and numerical investigations. New methods have been built around Symanzik's early idea of including additional operators into the action to systematically remove remaining cut-off effects up to a given power of the lattice spacing. Perturbative improvement, however, is known to be inefficient as long as one sticks to bare lattice expansions, and practical progress only came from the fruitful phenomenological recipe of tadpole renormalisation [18]. To overcome the shortcomings of perturbation theory completely, rather involved techniques have been developed to compute the additional couplings entering the classically improved action non-perturbatively via numerical simulation [19]. A more ambitious program is to construct an almost perfect action in which all terms of $O(a^{2n})$ are absent[20, 21, 22]. Unfortunately, it is still difficult to make decisive statements about the efficiency of improvement, even in the quenched approximation [23]. Concerning dynamical fermions, simulations of improved actions have only been started very recently [24, 25], so it will be a few years before enough data can be generated to determine the advantages and disadvantages of different approaches.

[1] In the past few years there has been rising interest in anisotropic lattices with $a_t \ll a_s$. Such an asymmetric choice becomes particularly important when dealing with improved actions on coarse grids. The technique was successfully applied to the computation of the glueball spectrum which suffers from low signal/noise on symmetric lattices, see for example [16, 17].

The discretisation of fermionic degrees of freedom is complicated by the notorious 'doubling' problem, i.e. the sixteenfold replication of fermion species, coming in pairs of left-handed and right-handed states, in four dimensions, when using the naive lattice Dirac operator. A natural escape, proposed by WILSON [26], is to add a dimension-five term to the action which decouples 15 doublers in the continuum limit leaving a single physical fermion. As a consequence of the Nielsen-Ninomiya no-go theorem [27], the Wilson term breaks chiral symmetry leading to an additive renormalisation of the quark mass.

A further technical problem which has important implications originates from the Grassmann nature of the fermions. Up to now, no direct way exists to handle such anticommuting field variables numerically. Fortunately, there is no need to do so, since quark fields enter the QCD Lagrangian in a quadratic form and hence, can be integrated out analytically leading to an effective bosonic theory. This bosonic theory is non–local, due to the fermion determinant multiplying the exponential of the gauge field action, and therefore its simulation is much more costly. For this reason it has been common to study a simplified theory in which the fermion determinant is set to a constant. In the perturbative language this *quenched* or *valence approximation* amounts to throwing away internal quark loops while keeping the valence quarks that propagate in a purely gluonic background.

Today's lattice calculations are able to give precise results for hadronic bound states within this approximation. High statistics lattice studies of quenched QCD on large physical volumes and fine grained-grids predict the spectrum of light hadrons within a few percent accuracy in the chiral and continuum limits. Whereas the GF11 data reproduced the physical spectrum within errors [28], recent results by CP-PACS [29, 30] reveal clear discrepancies between the quenched prediction and experiment. They suggest that dynamical quark effects on light hadron masses and matrix elements lie within a 10 to 20% range. The inclusion of quarks into the Lagrangian, however, increases the CPU requirements by a factor of $10^2 - 10^3$. Therefore, a comprehensive study of the infinite volume continuum limit in full lattice QCD remains a task for the upcoming TERAcomputers. Nevertheless, vacuum polarisation effects may already show up in simulations on intermediate volumes on the edge of the scaling regime. This surely is a reasonable expectation for quantities with inherent sea-quark dependence such as the πN σ-term, the η'-mass or the spin content of the nucleon. The heavy quark sector, however, may turn out to become of equal importance in this context. One reason is that low-lying quarkonium levels for instance, can be computed with high precision and are much less sensitive to extrapolations in the dynamical quark mass than quantities entirely built up of light quarks. A second argument applies to the particular case of treating the heavy quarks in the framework of an effective non-relativistic formulation of QCD. The effective theory is valid only in a range of cut-off values. It is tuned so as to reproduce QCD within this range and does not require (nor allow) an extrapolation to the continuum limit. Present resolutions of full QCD lattices lie within this *scaling window*. Hence it is hoped that vacuum polarisation effects may be isolated more safely in heavy quark systems though one expects their size to be smaller than in the quantities mentioned above.

Bound states of heavy quarks have attracted considerable interest in the experimental and theoretical study of electroweak interactions. The investigation of their decays allows

one to narrow the constraints on the less-known elements of the Cabibbo-Kobayashi-Maskawa matrix, whose precise knowledge is needed for a stringent test of the Standard Model of particle physics and the possible detection of 'new physics'. The principal uncertainty attached to theoretical estimates of form factors or decay constants is due to the difficulty in quantifying the non-perturbative QCD effects. These may be tackled by lattice simulations of QCD [31, 32]. Prior to facing the full complexity of weak matrix elements, of course, the capability of such an approach can be assessed by computing the mass spectrum. The role of lattice simulations for systems involving heavy quarks, the b quark to be specific, is thus twofold: first, they predict unmeasured quantities such as the B meson decay constant, the mixing parameter B_B and the masses of baryons and mesons containing the b quark; second, they serve to test the validity of other approaches like Heavy Quark Effective Theory (HQET) [33, 34, 35, 36, 37, 38].

Much activity has been in heavy-light systems. Another area of investigation has concentrated on heavy-heavy bound states which have been ignored by the lattice community for a long time. The physics of $Q\bar{Q}$ systems received new interest since it had been reformulated in the modern language of effective field theory. The study of heavy quarkonia benefits from several advantages [39]: first, we have a far more detailed understanding of the internal structure of $Q\bar{Q}$ mesons than we do for other hadrons from potential models, which give us control over systematic errors that arise in simulations. Second, quarkonia are smaller than hadrons containing light quarks, making it unlikely that the finite volume of the lattice has much of an effect upon simulation results. A further advantage comes from the observation that the lowest radial and orbital angular momentum splittings are independent of the heavy quark mass to a very good approximation.

There is a drawback, however: the direct simulation of heavy quark dynamics on the lattice employing the standard Wilson action suffers from serious discretisation errors. Currently typical values of the inverse lattice spacing are in the range of 2-4 GeV which is still below the b mass. To circumvent this problem, the non-relativistic effective theory for QCD (NRQCD) has been successfully applied in the past few years [2]. The NRQCD Lagrangian is written as a series of operators expanded in powers of the mean-squared heavy-quark velocity v^2, $\mathcal{L}_{\rm NRQCD} = \sum_{i,n} c_i(g^2) O_i(m_Q v^{2n})$, where the coefficients c_i are obtained by perturbative matching with QCD. The lattice version of NRQCD [42, 43] allows one to simulate heavy quarks with lattice spacing errors of $O(\mathbf{p}a)$, where $\mathbf{p}$ is a typical momentum of order $\Lambda_{\rm QCD}$, rather than the usual $O(m_Q a)$ for Wilson-type heavy quarks. This makes lattice NRQCD a promising technique to simulate systems containing a b-quark [3].

[2] There are several alternative methods (which are mostly applied to heavy-light systems): An obvious way to avoid large discretisation errors is to perform the simulation around the charm mass, which is considered to be sufficiently light, and then extrapolate to the bottom scale. Of course, lattice artefacts are still sizable for charm if the standard Wilson action is employed. They may be further reduced by using improved actions, most notably the Sheikholeslami-Wohlert action [40], which remove leading finite-a errors. A method that can be viewed as an 'interpolation' between the Wilson-type and the non-relativistic action has been developed by the Fermilab group [41]. None of these methods (including NRQCD for bottom) is entirely satisfactory, but they provide complementary information about the heavy-quark system.

[3] Applying NRQCD to charmonium turns out to be difficult. Each order of relativistic corrections is expected to be only 30% smaller than the previous one. Higher-order terms may contribute as much as 60% to spin splittings as demonstrated by TROTTIER [44]. In addition the lower charm mass requires rather coarse lattices for the effective theory to work, $\beta < 5.85$ in the quenched approximation [45]. This limit implies that we cannot treat charmonium appropriately on a dynamical Wilson lattice with $\beta = 5.6$.

Calculations of the spectrum of the $b\bar{b}$ system have been performed using the quenched approximation by [46, 47, 48]. So far, there has only been one analysis of the Υ with dynamical quarks: DAVIES ET.AL. [49, 50] applied an $O(m_b v^4)$ correct NRQCD action to gauge fields incorporating the effects of two dynamical staggered fermions. It was found that the experimentally known *spin-independent* spectrum could not be reproduced using the quenched approximation, whereas the data with 2 dynamical fermions agrees much better. These measurements were pushed to high statistics (4% statistical errors) in [49, 50] and exploited to obtain precision measurements of the strong coupling constant, α_s. Quenching was concluded to be the largest source of uncertainty in this calculation. The dependence of the splittings on the dynamical quark *mass* was estimated, using just two mass values, to be of the same order as the statistical error. No simulation applying NRQCD to dynamical *Wilson* fermions exists so far

In the *spin-dependent* sector the emerging picture is much less clear. The P-fine structure in the unquenched theory, obtained with the $O(m_b v^4)$-correct action, was found to be in very good agreement with experiment whereas the quenched results, using the same action, predict much smaller splittings. However, recent results of [48, 51, 44] (all of which use the quenched approximation) have exposed the sensitivity of the spin-dependent splittings to the details of the action: several improvements, such as the inclusion of higher order spin-dependent terms in the NRQCD expansion, the addition of lattice-artefact correcting terms of $O(a^2)$ [48, 44] as well as an improved phenomenological estimate of the coefficients c_i [44, 52] were found to have sizable effects of $O(10-20\%)$ for these splittings. Thus, there has recently been strong support in favour of using the $O(m_b v^6)$-correct NRQCD action where, to highest order, all *spin-dependent* corrections are added, as well as for the use of the mean-link Landau-gauge tadpole scheme to estimate the perturbative coefficients c_i. The effects of these improvements for dynamical configurations have not been studied.

In this thesis we attempt to address many of the open issues pin-pointed above. We study in detail the $b\bar{b}$ spectrum on unquenched gauge field configurations, which have been generated within the SESAM project, and present a new lattice estimate for the strong coupling constant $\alpha_{\overline{\rm MS}}(m_Z)$ based on these spectrum results.

SESAM aims to investigate Sea-Quark Effects on Spectrum And Matrix elements [53, 54, 55]. The project involves a large scale Hybrid Monte Carlo simulation of lattice QCD with dynamical Wilson fermions. Our computational platform has been the massively parallel APE100/QH2 with 256 nodes and an approximate peak performance of 13 Gflops. A full QCD simulation with Wilson fermions is particularly expensive, since the fermion propagator carries more degrees of freedom than in the staggered formulation. Hence it is a difficult task to choose simulation parameters in such a way that possible sea-quark effects are not masked by large systematic errors. SESAM was guided in this choice by early exploratory studies by GUPTA ET.AL. [56, 57]. Within the limited compute power of a pre-Tflops machine it is reasonable to accumulate significant statistics at a single value of the gauge coupling rather than to attempt a scaling analysis. Quenched simulations tell us

that scaling sets in at a lattice spacing of $a \approx 0.1$ fm. This corresponds to a bare coupling of $\beta = 5.6$ in the full theory. The mass parameter is constrained by the requirement that finite volume effects remain tolerable. The condition $m_\pi L \geq 4$ limits the smallest m_π/m_ρ ratio to approximately 0.69. SESAM generated samples with four different quark masses, each sample containing 5000 trajectories. The overall computational effort has reached 100 TFlops·h.

The plan of the thesis is as follows:

Hunting for Sea-Quarks

We start with a brief introduction into the subject of lattice regularised Quantum Chromodynamics to provide basic notations. Some aspects of the Hybrid Monte Carlo algorithm and its QCD implementation are discussed. We quote the relevant simulation parameters of SESAM's HMC runs, but refer to [58] for a detailed presentation of various algorithmic improvements and a study of autocorrelation times. Finally we point to some results obtained so far from the study of the static quark-antiquark potential and the light hadron spectrum.

Heavy Quarkonium and NRQCD

Chapter 3 introduces the non-relativistic effective theory for $Q\bar{Q}$ bound states. We describe those aspects that are relevant to the calculation of the bottomonium spectrum, but do not touch the NRQCD factorisation approach.

Lattice-Regularised NRQCD

The discretised version of the NRQCD Lagrangian is formulated in Chapter 4. We develop the evolution equation of the heavy quark propagator, construct correlation functions for S- and P-wave mesons and present our choice of smearing functions. NRQCD and QCD are matched both perturbatively and non-perturbatively. We discuss the simplified matching procedure which is usually applied to get around a laborious one-loop calculation.

Bottomonium Spectroscopy

Using SESAM's large sample of dynamical Wilson-fermion gauge configurations we study both the spin-independent as well as the spin-dependent spectrum of the Υ. Our strategy in searching for sea-quark effects will be to compare our final dynamical results to that of a quenched simulation at equivalent lattice spacing. Thus we hope to consolidate that unquenching brings the spin-independent splittings into good agreement with experiment. As an important new feature we can also study the dependence of mass-splittings on the light sea-quark mass. Following the recent suggestions of [48, 44] we have implemented the NRQCD action including spin-dependent corrections of $\mathcal{O}(m_b v^6)$ and we remove tadpoles using the mean link calculated in Landau gauge. With these ingredients we hope to clarify the effect of unquenching in the spin-dependent splittings.

Investigation of Systematic Errors

In Chapter 6 we turn to an analysis of systematic errors different to those stemming from quenching. We quantify the heavy-quark mass dependence of radial level splittings and spin splittings in heavy quarkonium. Furthermore we study their sensitivity to changes of the non-relativistic action in two respects: the convergence of the velocity expansion is examined by comparing leading order and next-to-leading order results and we test the influence of the tadpole improvement factor by switching from the Landau mean-link to the plaquette prescription.

The Strong Coupling Constant in Unquenched QCD

The accurate determination of the lattice spacing from the bottomonium spectrum can be used in a simple way to estimate the strong coupling constant. Starting with the perturbative expansion of the average plaquette, one calculates the *plaquette coupling* both in the quenched approximation and in the $n_f = 2$ theory. This data is then extrapolated in the number of flavours and converted to the $\overline{\text{MS}}$ scheme of dimensional regularisation. α_S computed within the framework of Lattice NRQCD belongs to the most accurate determinations of the strong coupling constant. We can improve on existing error estimates by an explicit study of the sea-quark mass dependence.

Part of the results presented here have been published prior to this thesis in Refs. [59, 55, 60, 61, 62, 63, 31].

Chapter 2
Hunting for Sea-Quarks

In this introductory chapter we give a brief outline of SESAM collaboration's lattice investigation of QCD with dynamical quarks. The project involves a detailed study of Sea-quark Effects on Spectroscopic quantities And, more general, QCD Matrix elements. It may be considered a 'second generation' Hybrid Monte Carlo simulation of Wilson fermions, in the sense that by improvements of algorithms and increased compute power we have been able to generate a sufficient sample of decorrelated gauge field configurations on reasonable lattices. Section 2.1 recalls the basic concept of lattice regularised QCD and supplies notation and formulae as a background for later chapters. Necessarily, the presentation will be very brief. Detailed introductions into the subject of lattice field theory may be found in [64, 65, 66, 67, 68]. At their core, lattice calculations involve numerical simulations, i.e. stochastic sampling procedures to generate background field configurations. The standard algorithm for simulating QCD is the Hybrid Monte Carlo algorithm (HMC). We outline SESAM's HMC simulation in Section 2.2 and close the chapter with some remarks on important results obtained so far.
The technical issues slightly touched on here are discussed in much more detail in Refs. [69, 58].

2.1 Euclidean Lattice QCD

The formulation of lattice gauge theory (LGT) is generally based on the functional integral representation of Green's functions in Euclidean space-time [1]. The restriction to the Euclidean metric is an algorithmic issue rather than a fundamental one. The integrand of the Minkowski path integral is complex and thus causes strong oscillations which cannot be treated with standard simulation techniques. The QCD action in Minkowski space-time reads

$$S^{(M)}_{\mathrm{QCD}} = \sum_q \int d^4x\ \bar{\Psi}_q(x)\left(i\gamma^\mu_{(M)} D_\mu - m_q\right)\Psi_q(x) - \int d^4x\ \frac{1}{2}\mathrm{Tr}\left[F_{\mu\nu}(x)F^{\mu\nu}(x)\right]\ , \qquad (2.1)$$

where the sum is over quark flavours and Dirac as well as colour indices have been suppressed. We define the covariant derivative through $D_\mu \equiv \partial_\mu + igA_\mu(x)$, $A_\mu(x) = A^a_\mu(x)T^a$. The normalisation of the Lie Algebra basis is chosen to be $\mathrm{Tr}(T^aT^b) = \delta^{ab}/2$. The field strength tensor is

$$igF_{\mu\nu} \equiv [D_\mu, D_\nu] = ig\left(\partial_\mu A_\nu - \partial_\nu A_\mu + ig[A_\mu, A_\nu]\right)\ . \qquad (2.2)$$

[1] There are attempts to tackle the QCD binding problem of the Kogut-Susskind lattice Hamiltonian applying the coupled cluster expansion. Up to now, these are restricted to simplified theories and even then the result is still inconclusive [70, 71, 72, 73].

After Wick rotating to Euclidean times,

$$x^0 \to -ix^4, \quad D_0 \to iD_4, \quad F_{0i} \to iF_{4i}\,, \tag{2.3}$$

the path integral weight $\exp(iS^{(M)}_{\rm QCD})$ becomes a real Boltzmann factor $\exp(-S^{(E)}_{QCD})$ and can be interpreted, if correctly normalised, as a probability density. The Euclidean action reads

$$S^{(E)}_{QCD} = \sum_q \int d^4x\ \bar\Psi_q(x)\left(\gamma^{(E)}_\mu D_\mu + m_q\right)\Psi_q(x) + \int d^4x\ \frac{1}{2}{\rm Tr}\left[F_{\mu\nu}(x)F_{\mu\nu}(x)\right]\,, \tag{2.4}$$

and the hermitian Dirac matrices are defined as

$$\gamma^{(E)}_4 \equiv \gamma^0_{(M)}\,, \quad \gamma^{(E)}_i \equiv -i\gamma^i_{(M)}\,. \tag{2.5}$$

Because of the Euclidean formalism, processes in real time are not directly accessible, whereas static quantities like energies of states or particle decay constants can be successfully calculated. These are obtained by evaluating the Euclidean two-point function

$$C(x_4) = \frac{1}{Z_E}\int [DA][D\bar\Psi][D\Psi]\mathcal{O}^*(x_4)\mathcal{O}(0)e^{-S^{(E)}_{\rm QCD}}\,, \tag{2.6}$$

where $\mathcal{O}$ is a composite field with appropriate transformation properties for the state under consideration. For an action that is Euclidean invariant and leads to reflection positive expectation values, the axioms by OSTERWALDER and SCHRADER [74, 75] guarantee the existence of a Hilbert space $\mathcal{H}$ with positive norm and a hermitian bounded Hamiltonian $\hat H$ defined on $\mathcal{H}$, with the lowest eigenstate having zero energy. Then the correlation function (2.6) equals the time ordered vacuum expectation value

$$\begin{aligned} C(x_4) &= \langle 0|T\left[\hat{\mathcal{O}}^\dagger(x_4)\hat{\mathcal{O}}(0)\right]|0\rangle && (2.7)\\ &= \langle 0|e^{x_4\hat H}\hat{\mathcal{O}}^\dagger e^{-x_4\hat H}\hat{\mathcal{O}}|0\rangle && (2.8)\\ &= \langle 0|\hat{\mathcal{O}}^\dagger e^{-x_4\hat H}\hat{\mathcal{O}}|0\rangle\,, && (2.9)\end{aligned}$$

which may be analytically continued back to Minkowski space. In order to obtain the spectral decomposition, we insert a complete set of energy eigenstates in $C(x_4)$, assuming a finite volume V,

$$\begin{aligned} \langle 0|\hat{\mathcal{O}}^\dagger e^{-x_4\hat H}\hat{\mathcal{O}}|0\rangle &= \langle 0|\hat{\mathcal{O}}^\dagger e^{-x_4\hat H}\sum_n |n\rangle\frac{1}{2E_nV}\langle n|\hat{\mathcal{O}}|0\rangle && (2.10)\\ &= \sum_n |\langle n|\hat{\mathcal{O}}|0\rangle|^2\frac{e^{-x_4E_n}}{2E_nV}\,. && (2.11)\end{aligned}$$

If the lowest state excited from the vacuum by the operator $\hat{\mathcal{O}}$ corresponds to a stable particle, there is no need to rotate back to Minkowski space-time. The energies or masses, as well as the creation amplitudes, can be read off directly from the exponential decay of the Euclidean correlation function Eq.(2.11).

To give the functional integral a mathematical meaning, we discretise QCD on a finite hypercubic lattice with lattice spacing a, spatial extent $L_S = aN_S$ and temporal extent $L_T = aN_T$. The lattice excludes momenta larger than $2\pi/a$ and thus provides a non-perturbative regularisation.

Discretising the gluon field

To maintain local gauge invariance the lattice gauge field is defined as the set of SU(3) parallel transporters along the links between neighbouring grid points

$$\{U_{x,\mu} \equiv U(x, x+a\hat\mu)|(x,\mu) \in \text{lattice}\}\,. \tag{2.12}$$

Here (x,μ) denotes the link that connects x with $x+a\hat\mu$, $\hat\mu$ being the unit vector in μ-direction. The *link variable*, $U_{x,\mu} \in {\rm SU(3)}$, is given in the fundamental representation and maps the spinor fields at point $x+a\hat\mu$ onto parallel fields at point x. Link variables are related to the continuum vector potential via the path-ordered integral

$$U_{x,\mu} = P\exp\left[-ig\int_{x+a\hat\mu}^{x} dzA_\mu(z)\right] \sim 1 + iagA_\mu(x+\frac{a}{2}\hat\mu) + O(a^2)\,. \tag{2.13}$$

Since the curvature associated with the connection A_μ is derived from the parallel transport along an infinitesimal closed path, it is obvious that the lattice analogue will be the product of link variables around an elementary square or *plaquette*,

$$U_{x,\mu\nu} \equiv U_{x,\mu}U_{x+a\hat\mu,\nu}U^\dagger_{x+a\hat\nu,\mu}U^\dagger_{x,\nu} \sim 1 + iga^2F_{\mu\nu} - \frac{g^2}{2}a^4F^2_{\mu\nu} + ia^3L_{\mu\nu} + ia^4M_{\mu\nu} + O(a^5)\,. \tag{2.14}$$

From Eq.(2.14) one obtains the *Wilson gauge action* as

$$S^W_g[U] \equiv \beta\sum_{x,\mu>\nu}\left(1 - \frac{1}{3}\Re\,{\rm Tr}U_{x,\mu\nu}\right) = \int d^4x\,\frac{1}{2}{\rm Tr}\left(F_{\mu\nu}F_{\mu\nu}\right) + O(a^2)\,, \tag{2.15}$$

where $\beta = 6/g^2$. There is nothing special of using the plaquette in the construction of the action. Any other Wilson loop can be chosen provided it has the correct classical continuum limit. The advantages of small loops are typically smaller discretisation errors and higher computational speed.

Discretising the fermion field

The discretisation of the fermionic action [2],

$$S_f = \int d^4x\ \bar\Psi\left(\gamma^{(E)}_\mu D_\mu + m\right)\Psi\,, \tag{2.16}$$

is greatly complicated as a consequence of the Nielsen-Ninomiya theorem [27]. The lattice theory lacks chiral symmetries: Under a set of rather mild assumptions which are translation invariance, locality and hermiticity of the underlying Hamiltonian, the theorem tells us that there are always pairs of left-handed and right-handed fields belonging to the same representation of the gauge group.

[2] We consider only one flavour to simplify notation.

Replacing the covariant derivative by a symmetric difference is the most local choice which preserves the anti-hermitian nature of the continuum operator $\gamma_\mu^{(E)} D_\mu$. One obtains the so-called 'naive' fermion action,

$$S_f^{\text{naive}} = \frac{1}{2a} \sum_{x,\mu} a^4 \bar{\Psi}_x \gamma_\mu^{(E)} \left(U_{x,\mu} \Psi_{x+a\hat{\mu}} - U^\dagger_{x-a\hat{\mu},\mu} \Psi_{x-a\hat{\mu}} \right) + \sum_x a^4 m \bar{\Psi}_x \Psi_x \,, \tag{2.17}$$

which represents 2^d degenerate fermions in d dimensions instead of only one. This is obvious from the free fermion propagator

$$G(k) = \frac{am - i\gamma_\mu^{(E)} \sin(k_\mu)}{(am)^2 + \sum_\mu \sin^2(k_\mu)} \,. \tag{2.18}$$

$G(k)$ has poles near the 16 corners of the Brillouin zone, i.e. if each component of k_μ is either 0 or π.

A prominent way to escape the consequences of the no-go theorem is to break chiral symmetry explicitly right from the start, and aim to recover it only in the continuum limit. Wilson [26] suggested adding a second-order derivative term to the naively discretised action,

$$S_f^W = -\sum_{x,\mu} a^4 \frac{r}{2a} \bar{\Psi}_x \left(U_{x,\mu} \Psi_{x+a\hat{\mu}} - 2\Psi_x + U^\dagger_{x-a\hat{\mu},\mu} \Psi_{x-a\hat{\mu}} \right) \,. \tag{2.19}$$

Such a term implies that the doublers pick up an effective mass $m + 2r/a^{-1}$, so that for finite *Wilson parameter*, r one expects them to decouple from the theory leaving a single physical fermion. Usually the field normalisations are changed to bring the action into a particularly simple form:

$$a^{3/2} (am + 4r)^{1/2} \Psi_x \to \Psi_x \,, \quad a^{3/2} (am + 4r)^{1/2} \bar{\Psi}_x \to \bar{\Psi}_x \,. \tag{2.20}$$

Including the gauge field part, we arrive at the *Wilson action*

$$\begin{aligned} S &= S_g^W + S_f^{\text{naive}} + S_f^W \\ &= S_g^W + \sum_{x,y} \bar{\Psi}_x M_{x,y} \Psi_y \end{aligned} \tag{2.21}$$

with the fermion matrix,

$$M_{x,y} = \delta_{x,y} - \kappa \sum_{\mu=1}^{4} \left[(r - \gamma_\mu^{(E)}) U_{x,\mu} \delta_{x+a\hat{\mu},y} + (r + \gamma_\mu^{(E)}) U^\dagger_{x-a\hat{\mu},\mu} \delta_{x-a\hat{\mu},y} \right] \,. \tag{2.22}$$

We have suppressed Dirac and colour indices in Eq.(2.22) and introduced the *hopping parameter*

$$\kappa \equiv \frac{1}{2am + 8r} \,. \tag{2.23}$$

In numerical simulations one almost always sets $r = 1$. This is in the range of values where the lattice theory satisfies reflection positivity. Furthermore there are no doublers then in the free field limit. Eq.(2.23) defines the bare quark mass as

$$ma = \frac{1}{2\kappa} - 4r \equiv \frac{1}{2\kappa} - \frac{1}{2\kappa_c} \tag{2.24}$$

with $ma = 0$ at $\kappa = \kappa_c = 1/8r$ for the free theory. In the interacting theory one may stick do this definition with the proviso that the *critical hopping parameter*, κ_c, now depends on the lattice spacing as a consequence of the explicit breaking of chiral symmetry. Another severe drawback of Wilson fermions are discretisation errors linear in a rather than $O(a^2)$ for the naive action [3].

The quenched approximation

To complete the definition of the theory one has to specify an integration measure

$$[\mathrm{d}U][\mathrm{d}\bar{\Psi}][\mathrm{d}\Psi] \equiv \prod_{x,\mu} \mathrm{d}U_{x,\mu} \prod_y \mathrm{d}\bar{\Psi}_y \prod_z \mathrm{d}\Psi_z \,, \tag{2.25}$$

where link variables are integrated with the invariant group measure. Then the expectation value of an arbitrary function of the field variables, $\mathcal{O}(\bar{\Psi}, \Psi, U)$ is given by

$$\langle \mathcal{O}(\bar{\Psi}, \Psi, U) \rangle = \frac{\int [\mathrm{d}U][\mathrm{d}\bar{\Psi}][\mathrm{d}\Psi] \mathrm{e}^{-S_{\text{QCD}}^{(E)}} \mathcal{O}(\bar{\Psi}, \Psi, U)}{\int [\mathrm{d}U][\mathrm{d}\bar{\Psi}][\mathrm{d}\Psi] \mathrm{e}^{-S_{\text{QCD}}^{(E)}}} \,. \tag{2.26}$$

Since the action is quadratic in the fermion fields the Grassmann variables can be integrated out,

$$\int [\mathrm{d}\bar{\Psi}][\mathrm{d}\Psi] \mathrm{e}^{-(S_f^{\text{naive}} + S_f^W)} = \det(M[U])^{n_f} \,, \tag{2.27}$$

assuming degenerate flavours. If we choose as an example the function $\mathcal{O}(\bar{\Psi}, \Psi, U) = \Psi_{y_1} \bar{\Psi}_{x_1} \ldots \Psi_{y_n} \bar{\Psi}_{x_n} F[U]$, we arrive at the following form of the expectation value Eq.(2.26)

$$\begin{aligned} &\langle \mathcal{O}(\bar{\Psi}, \Psi, U) \rangle = \\ &\frac{\int [\mathrm{d}U] \det(M[U])^{n_f} \mathrm{e}^{-S_g^W} F[U] \sum_{z_1,\ldots,z_n} \epsilon^{z_1 z_2 \ldots z_n}_{y_1 y_2 \ldots y_n} M[U]^{-1}_{z_1 x_1} M[U]^{-1}_{z_2 x_2} \ldots M[U]^{-1}_{z_n x_n}}{\int [\mathrm{d}U] \det(M[U])^{n_f} \mathrm{e}^{-S_g^W}} \end{aligned} \tag{2.28}$$

In the *quenched* or *valence approximation* the quark determinant is set to a constant, $\det M[U] = \text{const}$, which amounts to neglecting the effects of vacuum polarisation since in perturbation theory the expansion of the determinant generates the closed fermion loops. Quenching reduces the computational costs by several orders of magnitude, because the gauge field updating can be done with the pure gauge action. However, it induces an uncontrolled uncertainty on lattice predictions.

In this thesis we go beyond the quenched approximation and deal with gauge field configurations that include two degenerate flavours of dynamical quarks. The restriction to pairs of equal-mass fermions is necessary to guarantee the positivity of the quark determinant.

[3] An alternative method to fix the doubling problem is the Kogut-Susskind staggered formulation which reduces the 16 fermion species to four by spin-diagonalisation. Staggered fermions have $O(a^2)$ errors and retain a residual axial symmetry.

2.2 HMC Simulation Set-Up

The Hybrid Monte Carlo (HMC) algorithm by DUANE ET.AL. [76] has become the standard tool for practical simulations of full QCD. Detailed discussions of its implementation and characteristics are presented in [58, 77]. SESAM has performed a large-scale HMC simulation of QCD with two degenerate flavours of dynamical Wilson quarks. We have generated lattices of extent $16^3 \times 32$ at four different quark masses corresponding to hopping parameters, $\kappa = 0.1560, 0.1565, 0.1570, 0.1575$. The computational cost of an unquenched simulation only allowed us to study a single value of the bare lattice coupling: $\beta = 5.6$ is appropriate to realise resolutions of $a \sim 0.1$ fm which is at the onset of the scaling regime in the quenched approximation. The choice of these parameters was guided by early exploratory studies of dynamical Wilson fermions by GUPTA ET.AL. [56, 57].
The time consuming part of the HMC is the repeated inversion of the Wilson fermion matrix. It has been accelerated using two different preconditioning techniques: Conventional even-odd decomposition of the fermion matrix [78] was applied in the first stage of the simulation. Later it was replaced by the locally lexicographic SSOR preconditioner [79, 80] which has been shown to offer up to a factor of 2 less computational costs. The use of the chronological start vector guess as proposed in [81] further helps to reduce the inversion time.
Time step size and number of molecular dynamics steps have been chosen so as to guarantee an acceptance rate $> 70\%$. Individual trajectory lengths n_{md} are varied by numbers uniformly distributed in the range $\pm 2\sqrt{\bar{n}_{\mathrm{md}}}$ around a fixed value $\bar{n}_{\mathrm{md}}$ as recommended in Ref. [82]. The relevant parameters of the HMC runs are summarised in Table 2.1.
For each κ value Markov chains with 5000 trajectories have been generated. To control the statistical quality, SESAM has carefully studied the autocorrelation of the time series. Table 2.2, taken from [58], contains estimates of the integrated autocorrelation times

$$\hat{\tau}_{\mathrm{int}} = \frac{1}{2} + \frac{1}{C^A(0)} \sum_{t=1}^{t_{\mathrm{MC}}} C^A(t) \,, \tag{2.29}$$

with

$$C^A(t) = \langle (A(i) - \langle A \rangle)\,(A(i+t) - \langle A \rangle) \rangle \,, \tag{2.30}$$

for the plaquette, the pseudoscalar and the vector mass. For these quantities $\hat{\tau}_{\mathrm{int}}$ is of $O(10)$ or less. Since we cannot afford to skip too many trajectories we choose an average separation of 25 between measurements and arrive at a number of 200 decorrelated configurations.

Metacomputing resources

The computer experiment has been realised on the special purpose machines APE Quadrics QH2 at IfH/DESY Zeuthen and the Universität Bielefeld. It is a single user SIMD computer with a peak performance of 12.8 GFlops. The HMC implementation achieves a sustained rate of about 60%. We have stored all generated trajectories on the data archive at ZAM/FZ Jülich to enable a detailed post-production analysis. The overall

$\beta = 5.6$, $n_f = 2$, $V \times T = 16^3 \times 32$						
κ	0.1560	0.1565	0.1570		0.1575	
Algorithm	o/e	SSOR	o/e	SSOR	o/e	SSOR
n_{md}	100 ± 20	100 ± 20	100 ± 20	100 ± 20	100 ± 20	71 ± 12
n_{csg}	6	7	8	9	11	3
# of iter.	85(3)	89(6)	168(5)	125(3)	317(12)	150(6)
acc. rate[%]	85		84	80	76	73
# of traj.	5000	5000	1500	3500	3000	2000
# of confs.	200	200	200		200	

Table 2.1. *Simulation parameters of SESAM's HMC runs. n_{md} is the number of molecular dynamics steps, n_{csg} denotes the order of the polynomial start vector guess. Also listed are the average number of BiCGStab iterations and the average acceptance rate.*

	$\kappa = 0.156$		$\kappa = 0.157$		$\kappa = 0.1575$	
observable	t_{MC}	$\hat{\tau}_{\mathrm{int}}$	t_{MC}	$\hat{\tau}_{\mathrm{int}}$	t_{MC}	$\hat{\tau}_{\mathrm{int}}$
$\langle \frac{1}{3} \Re \mathrm{Tr} U_{x,\mu\nu} \rangle$	2500	3(1)	3000	4(1)	2500	7(1)
m_π^{sl}	2500	11(1)	2500	13(1)	1700	19(2)
m_π^{ss}	2500	1.8(0.1)	2500	2.6(0.2)	1700	3.6(0.3)
m_ρ^{sl}	2500	6(0.5)	2500	8(1)	1700	10(1)
m_ρ^{ss}	2500	1.6(0.1)	2500	2.3(0.2)	1700	3.4(0.3)

Table 2.2. *Integrated HMC autocorrelation times $\hat{\tau}_{\mathrm{int}}$ for the plaquette, the pseudoscalar and the vector mass [55, 58]. The superscript sl denotes smeared source and local sink whereas ss indicates smearing at both source and sink. t_{MC} is the length of the underlying time series. This table has been taken from [58].*

compute effort has been around 300 days on the QH2 corresponding to 100 TFlops·h. The computation of the heavy quarkonium spectrum on these configurations have been mostly carried out on the Connection Machines CM5 at the Bergische Universität Wuppertal and the Universität Erlangen.

2.3 Sea-Quark Signals

It is a plausible expectation that vacuum polarisation effects show up primarily in quantities containing light quarks, in particular if these quantities are inherently sea-quark dependent. Consequently SESAM has focussed on the light hadronic sector. This, on the other hand, makes the study of heavy quarkonium an important complementary investigation. It is remarkable that simulations of bottomonium have been among the first to present evidence for dynamical quark effects.

Before we enter the details of the heavy quarkonium analysis in the following chapters, we here briefly touch on some of SESAM's results mainly from the light quark sector. Extended discussions of the project may be found in [62, 55].

The calculation of the static quark-antiquark potential is the 'classic' lattice experiment and has also been the first one performed on the dynamical configurations [83]. An exciting property of full QCD, which is not shared by the quenched approximation is the breaking of the colour string that connects quark and antiquark once the separation becomes large enough to produce a meson from the vacuum. As a sign of string breaking in the potential one expects the linear rising part to flatten out eventually. The SESAM data does not exhibit such behaviour up to distances of $r \sim 1.4$ fm. A likely explanation for this result has been pointed out by GÜSKEN [62]: the Wilson loop operator used to compute the potential has insufficient overlap with the state of two static-light mesons which results from string breaking. Very recent observations of the phenomenon in $SU(2)$ Higgs models strongly point in this direction [84, 85]. Except from string breaking SESAM clearly observes the effect of dynamical flavours in the Coulomb coefficient which is increased by more than 10%.

The analysis of the light hadron spectrum faces the problem that, due to the restriction to 2 dynamical flavours, the light and strange quarks cannot be treated on equal footing. It is natural to identify the sea-quarks with the (degenerate) up and down quarks whereas the strange sector is to be handled in a semi-quenched way. SESAM has proposed simultaneous fits to a set of hadron masses that allow access to arbitrary points in the plane spanned by the sea-quark and valence quark mass parameters. Unfortunately, the analysis does not reveal a significant unquenching effect in the light hadron sector. Due to the considerable variation of hadron masses under chiral extrapolation, we are not able to overcome the well-known shortcomings of quenched calculations, namely the underestimation of the $K - K^*$ and $N - \Delta$ spin splittings.

A somewhat puzzling result has been obtained for the quark masses. SESAM's values for the light and strange quarks are

$$m_{\overline{\mathrm{MS}}}^{\mathrm{light}}(2\ \mathrm{GeV}) = 2.7(2)\mathrm{MeV} \tag{2.31}$$

$$m_{\overline{\mathrm{MS}}}^{\mathrm{strange}}(2\ \mathrm{GeV}) = 140(20)\mathrm{MeV}\,. \tag{2.32}$$

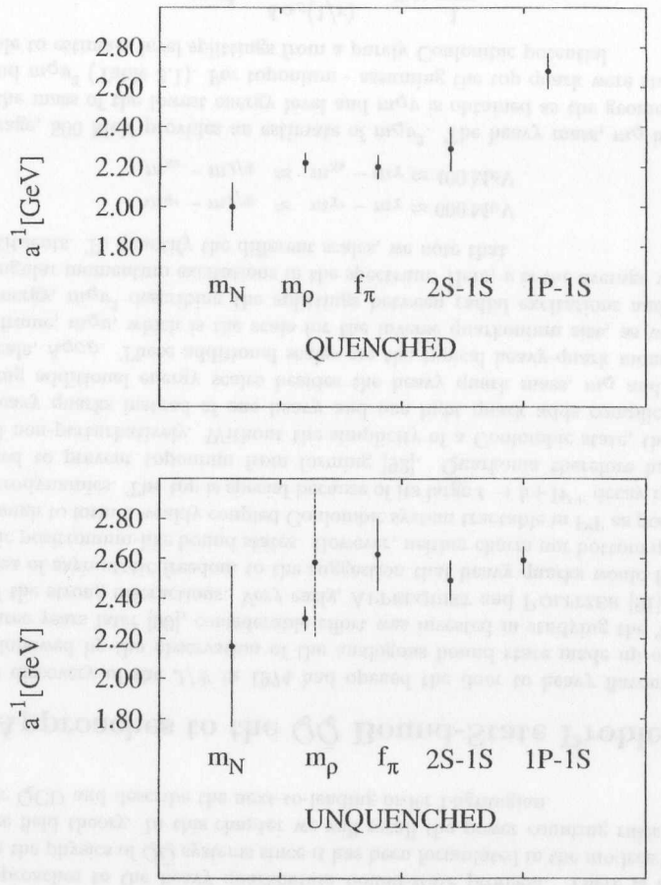

Figure 2.1. *Dependence of the lattice scale on the quantity used to fix it. The lower plot includes two values of a^{-1} from m_ρ. The one with the smaller error bars is taken from a linear chiral extrapolation whereas the second belongs to a quadratic fit.*

The light quark mass is much smaller than in the quenched approximation whereas the strange is compatible within errors. Our dynamical result for the ratio, $m^{\text{strange}}/m^{\text{light}} \approx 52$ differs significantly from chiral perturbation theory estimates [86] and sum rule results [87].

As a consequence of quenching, lattice spacings determined from different quantities will differ. It is therefore expected that the dependence of a^{-1} on the choice of observable will be smoothed out once dynamical quarks are switched on. In Figure 2.1 we compare lattice spacings obtained from a series of quantities that probe different momentum scales. We observe a significant variation in the quenched case. Scales from the nucleon and the P-S bottomonium splitting differ by 50%. The situation looks much better for the unquenched data. Within errors no dependence is seen. Unfortunately, however, these errors are quite large for the nucleon (and the quadratically extrapolated ρ-meson) due to the chiral extrapolation.

2.4 Summary

To nail down vacuum polarisation effects, very accurate simulations and refined analysis methods are needed. We have drawn an outline of SESAM's lattice QCD simulation involving dynamical Wilson quarks. The detailed knowledge of autocorrelation times is essential to provide reliable estimates of physical quantities. We have discussed an (incomplete) list of results obtained so far, which mainly concerned the light hadron sector. In the following we turn to the bound-state problem of heavy quarks and investigate in detail the effect of vacuum polarisation on energy splittings in this system.

Chapter 3

Heavy Quarkonium and NRQCD

We provide the background for later investigations with a discussion of theoretical approaches to the heavy quarkonium bound-state problem. There is a revived interest in the physics of $Q\bar{Q}$ systems since it has been formulated in the modern language of effective field theory. In this chapter we will recall the power counting rules for non-relativistic QCD and describe the next-to-leading order Lagrangian.

3.1 Approaches to the $Q\bar{Q}$ Bound-State Problem

After the discovery of the J/Ψ in 1974 had opened the door to heavy flavour physics [88, 89], followed by the observation of the analogous bound state made up of bottom quarks three years later [90], considerable effort was invested in studying the 'hydrogen atoms' of the strong interactions. Very early, Appelquist and Politzer [91] were led by the idea of asymptotic freedom to the suggestion that heavy quarks would form non-relativistic positronium-like bound states. However, neither charm nor bottom quarks are heavy enough to form a weakly coupled Coulombic system tractable in PT as positronium is in electrodynamics. The top is special because of its large $t \to b + W^+$ decay rate which is expected to prevent toponium from forming [92]. Quarkonia therefore have to be described non-perturbatively. Without the simplicity of a Coulombic state, the binding of two heavy quarks instead of one heavy and one light quark adds complications by introducing additional energy scales besides the heavy quark mass, m_Q and the low-energy scale, Λ_{QCD}. These additional scales are the typical heavy-quark momentum in the rest frame, $m_Q v$, which is the scale for the inverse quarkonium size, as well as the kinetic energy, $m_Q v^2$ describing the splittings between radial excitations and between orbital angular momentum excitations in the spectrum. Here, v is the average velocity of the constituents. To quantify the different scales, we note that

$$\begin{aligned} m_{\Psi'} - m_{J/\Psi} &\approx m_{\Upsilon'} - m_{\Upsilon} \approx 600\,\text{MeV} \\ m_{\chi_c} - m_{J/\Psi} &\approx m_{\chi_b} - m_{\Upsilon} \approx 400\,\text{MeV}\,. \end{aligned} \tag{3.1}$$

The average, 500 MeV provides an estimate of $m_Q v^2$. The heavy mass, m_Q is taken to be half the mass of the lowest energy level and $m_Q v$ is obtained as the geometric mean of m_Q and $m_Q v^2$ (Table 3.1). For toponium - assuming the top quark were stable - it is reasonable to estimate level splittings from a purely Coulombic potential

$$m_t v^2 \sim \frac{4}{3}\frac{\alpha_S(1/r)}{r}\,, \quad r \sim \frac{1}{m_t v}\,. \tag{3.2}$$

Then the difference between the ground state and the first excitation is

$$E' - E = \frac{\alpha_s^2}{3} m_t\,. \tag{3.3}$$

	$c\bar{c}$	$b\bar{b}$	$t\bar{t}$	e^+e^-
M	1.5 GeV	4.7 GeV	175 GeV	0.5 MeV
Mv	0.9 GeV	1.5 GeV	16 GeV	3.6 keV
Mv^2	0.5 GeV	0.5 GeV	1.5 GeV	25 eV
v^2	0.3	0.1	0.009	$5 \cdot 10^{-5}$
$\alpha(m_Q)/\pi$	0.1	0.07	0.04	$2 \cdot 10^{-3}$

Table 3.1. *Scales in quarkonium and positronium and the expansion parameters of the non-relativistic approximation [93, 94].*

For $m_t = 175$ GeV this splitting is approximately 1.5 GeV corresponding to $v \approx 0.09$. Low quark velocities have two important implications: first, the bound state will be dominantly $Q\bar{Q}$ as the radiation of a low-energy gluon from a quark is suppressed [1]. Second, the gluon exchange will appear instantaneous as the gluon kinetic energy is larger by a factor $1/v$ compared to the quark kinetic energy [42]. Both features taken together suggest a non-relativistic quark-model picture of heavy-quark bound states. In the infinite-mass limit the spin interaction vanishes and one is left with a static central potential. A good description of the observed $c\bar{c}$ and $b\bar{b}$ spectra can be obtained using a potential that is Coulombic at short distances and confining at large separations, the Cornell potential [95]

$$V(r) = -\frac{4}{3}\frac{\alpha_S}{r} + \sigma r \,. \tag{3.4}$$

However, other choices work equally well like the RICHARDSON potential [96], the MARTIN potential [97] or the potential of BUCHMÜLLER and TYE [98] which satisfies the asymptotic properties of (3.4) but includes the effects of two-loop running at small distances. Even a logarithmic form manages to work, although it has no motivation from QCD [99]. The reason is that the Υ and Ψ families of resonances probe a quark-antiquark distance of 0.1 - 0.8 fm and all the above potentials can be made to agree in this range by a proper choice of parameters, although they may differ significantly for shorter and larger separations [2].

Although the usefulness of the potential model picture is undoubted, it misses the link to QCD. A much more involved and computationally demanding approach is to extract the instantaneous $Q\bar{Q}$ potential in lattice QCD and subsequently use it in a Schrödinger equation to compute the spectrum. Precise lattice simulations have been performed by BALI and SCHILLING [101, 102]. This technique is, of course, not restricted to the central potential. The complete set of spin-dependent interactions (EICHTEN and FEINBERG [103]) is accessible to the lattice method by expressing the additional potentials as correlation functions of the chromofields in the presence of Wilson loops [104, 105]. A thorough investigation is presented in Refs. [106, 107].

In the following we pursue a third approach which, in contrast to the ones mentioned above, allows for a direct computation of $Q\bar{Q}$ bound states from QCD cast into the form of an equivalent non-relativistic effective theory. The effective theory is realised as a systematic expansion in the heavy-quark velocity about the non-relativistic limit. According

[1] The virial theorem applied to a Coulombic potential implies $v \sim \alpha_S(m_Q v)$.

[2] For a recent review of the history of the heavy-quark potential see [100]

to the estimates in Table 3.1, such an expansion seems well justified for bottomonium and may still yield good results for charmonium. It does not invoke the existence of a potential and can in principle be fully matched to QCD.

3.2 Non-Relativistic Effective Theory of Heavy Quarkonium

Extracting the quarkonium spectrum on the lattice from the QCD Lagrangian itself would involve the full range of scales in Table 3.1 which are well separated when the velocity is small. The grid size L and the lattice resolution a would have to fulfill

$$L \gg \frac{1}{m_Q v^2} \gg \frac{1}{m_Q v} \gg \frac{1}{m_Q} \gg a \,, \tag{3.5}$$

which is beyond present computing capabilities. On the other hand, the situation of well separated scales can be used to get rid of the major obstacle, the heavy-quark mass m_Q, by integrating out all momentum modes larger than a suitable cut-off Λ_c. Given that the physics of the meson is dominated by momenta of order $m_Q v$, a physically sensible choice is

$$m_Q v \ll \Lambda_c \ll m_Q \,. \tag{3.6}$$

The result of such a renormalisation group transformation is a non-local effective theory. However, it is crucial that the effects of modes of order m_Q can be reproduced by local interactions among the lower-momentum modes realised as an infinite series in the heavy-quark velocity, v^2. Relativistic intermediate states are highly virtual and cannot propagate large distances. Thus they are point-like on the scale of the quarkonium structure. The additional interactions come with couplings that depend on the cut-off. These couplings have to be tuned in order that observables computed in the effective theory match those computed in QCD. At tree level, the velocity expansion can be obtained by a Foldy-Wouthuysen-Tani transformation, generalised to the non-abelian case, that decouples the quark and antiquark fields in the Lagrangian [108],

$$\Psi \longrightarrow \exp(-i\vec{\gamma}\cdot\mathbf{D}/2m_Q)\Psi \,, \tag{3.7}$$

where $\mathbf{D}$ is the spatial covariant derivative. The terms generated this way are bilinear in the quark fields. In addition, the cut-off theory includes quartic and higher-order terms. The easiest way to derive the general non-relativistic Lagrangian is to use the effective field theory strategy [93]:

(a) Identify the low-energy degrees of freedom.
(b) Identify the symmetries of the original Lagrangian that can be maintained in the cut-off theory.
(c) Write down the most general Lagrangian that is consistent with the symmetries including all operators required to achieve a specified accuracy.
(d) Calculate the coefficients of these operators by matching low-energy observables in the effective theory with those in the full theory.

The resulting Lagrangian defines the effective theory of the low-energy sector of systems containing two heavy quarks and is called Non-Relativistic QCD (NRQCD). The approach was first introduced by CASWELL and LEPAGE [109] to handle bound states in QED and has been formulated in QCD by THACKER ET.AL. [42, 39, 43]. Combined with the methods of perturbative factorisation, it provides a tool to calculate inclusive quarkonium production cross sections as a double expansion in v^2 and α_S (BODWIN, BRAATEN and LEPAGE [110]). The rest of this section will be devoted to the derivation of the NRQCD-Lagrangian in the continuum, based on the velocity-scaling rules quoted in [43].

3.2.1 Low-Energy Degrees of Freedom and Symmetries

The degrees of freedom relevant for the low-energy $Q\bar{Q}$ sector are the heavy quark and antiquark fields, ψ and χ, which are Pauli-spinors representing the upper and lower components of the Dirac-spinor, $\Psi_Q = (\psi, \chi)$. Further, we have the gauge field A_μ and the Dirac fields for the light quarks. The Lagrangian should have the following symmetries

(i) SU(3) gauge symmetry
(ii) rotation symmetry
(iii) charge conjugation

$$\mathcal{C}\psi = -i\sigma_2\chi^*\,, \quad \mathcal{C}\chi = i\sigma_2\psi^*\,. \tag{3.8}$$

(iv) parity

$$\mathcal{P}\psi(\mathbf{x},t) = \psi(-\mathbf{x},t)\,, \quad \mathcal{P}\chi(\mathbf{x},t) = -\chi(-\mathbf{x},t)\,. \tag{3.9}$$

The NRQCD Lagrangian is formulated in the heavy-quark rest frame and therefore necessarily breaks Lorentz symmetry down to its rotational subgroup. The lattice regulator introduced in the next chapter reduces this symmetry further to the cubic group.

3.2.2 Velocity-Scaling Rules

The rules of power counting in NRQCD, also denoted as *velocity-scaling rules*, have been established in [43]. We follow the arguments given there.

The magnitude of the quark and antiquark fields is estimated from the expectation value of the number operator in a quarkonium state which is close to 1,

$$\langle H| \int d^3x\; \psi^\dagger\psi |\, H\rangle \approx 1, \quad \langle H|H\rangle = 1\,. \tag{3.10}$$

We assume the quarkonium size to be $\sim 1/m_Q v$. The quark has to be localised within this region

$$\int d^3x\; \psi^\dagger\psi \approx \frac{1}{(m_Q v)^3}\,\psi^\dagger\psi \quad \Longrightarrow \quad [\psi] \sim (m_Q v)^{\frac{3}{2}}\,. \tag{3.11}$$

Operator	Magnitude	
ψ	$(m_Q v)^{\frac{3}{2}}$	quark annihilation operator
χ	$(m_Q v)^{\frac{3}{2}}$	antiquark creation operator
D_t	$m_Q v^2$	time derivative
$\mathbf{D}$	$m_Q v$	spatial derivative
$g\phi$	$m_Q v^2$	scalar potential
$g\mathbf{A}$	$m_Q v^3$	vector potential
$g\mathbf{E}$	$m_Q^2 v^3$	chromoelectric field
$g\mathbf{B}$	$m_Q^2 v^4$	chromomagnetic field

Table 3.2. *Estimates of magnitude of the degrees of freedom in NRQCD in terms of the heavy-quark mass, m_Q and the velocity, v. The important content here is the scaling with v. The factors of m_Q just follow from dimensional analysis.*

The kinetic energy operator scales like $m_Q v^2$. Eq.(3.10) then implies the following estimate for the spatial covariant derivative

$$\langle H| \int d^3x\; \psi^\dagger \frac{\mathbf{D}^2}{2m_Q}\psi |\, H\rangle \approx m_Q v^2 \quad \Longrightarrow \quad [\mathbf{D}] \sim m_Q v\,. \tag{3.12}$$

The scaling of the time component of the covariant derivative follows from the last equation if one invokes the lowest-order field equation,

$$\left(iD_0 + \frac{\mathbf{D}^2}{2m_Q}\right)\psi = 0\,, \tag{3.13}$$

therefore $[D_0] = [\mathbf{D}^2/2m_Q] \sim m_Q v^2$ as one would have expected. Estimates for the gauge fields can be obtained from the field equations for ψ and A_0 in the Coulomb gauge,

$$\left(i\partial_0 - gA_0 + \frac{\nabla^2}{2m_Q}\right)\psi \;\approx\; 0\,, \tag{3.14}$$

$$\nabla^2 gA_0 + g^2\psi^\dagger\psi \;\approx\; 0\,, \tag{3.15}$$

neglecting the vector potential. Eq.(3.14) requires gA_0 to scale like $\nabla^2/2m_Q$, i.e. $[gA_0] \sim m_Q v^2$. Eq.(3.15) suggests that $g^2 \sim v$. Finally, one considers the equation of motion for the Coulomb-gauge vector potential

$$\left(\partial_0^2 - \nabla^2\right) g\mathbf{A} \approx \partial_0 \nabla gA_0 - \frac{ig^2}{m_Q}\psi^\dagger\nabla\psi\,, \tag{3.16}$$

providing the scaling rule $[g\mathbf{A}] \sim m_Q v^3$. The scaling of the chromoelectric and chromomagnetic fields then follows from

$$g\mathbf{E} = -\nabla gA_0 + \ldots\,, \quad g\mathbf{B} = \nabla \times g\mathbf{A} + \ldots\,. \tag{3.17}$$

Table 3.2 summarises the velocity scaling properties obtained by the above heuristic considerations. They will be used as a guide in the construction of the effective Lagrangian. Whether they hold non-perturbatively has to be checked in the simulation.

3.2.3 The NRQCD Lagrangian at Next-To-Leading Order

We will build up the effective Lagrangian including spin-independent interactions that scale like $m_Q v^4$ and spin-dependent terms of order $m_Q v^6$, i.e. next-to-leading order in both cases. The NRQCD Lagrangian takes the form

$$\mathcal{L}_{\rm NRQCD} = \mathcal{L}_q + \mathcal{L}_g + \mathcal{L}_Q + \mathcal{L}_{\bar{Q}} \,, \tag{3.18}$$

where $\mathcal{L}_q$ and $\mathcal{L}_g$ are the light quark and gluon parts of the QCD Lagrangian that remain unchanged, and $\mathcal{L}_Q, \mathcal{L}_{\bar{Q}}$ denote the heavy quark and antiquark parts in the effective theory[3]. Interaction terms within $\mathcal{L}_Q$ are ordered according to the powers of v^2 they carry,

$$\mathcal{L}_Q = \mathcal{L}_Q^{(2)} + \mathcal{L}_Q^{(4)} + \mathcal{L}_Q^{(6)} + \dots \,, \tag{3.19}$$

and similar for the antiquark Lagrangian. The leading order contribution is the Lagrangian of a Schrödinger field theory

$$\mathcal{L}_Q^{(2)} = \psi^\dagger \left(iD_0 + \frac{\mathbf{D}^2}{2m_Q} \right) \psi \,. \tag{3.20}$$

The overall scale in minimal NRQCD is thus $m_Q^4 v^5$. We will, however, divide out a factor $m_Q^3 v^3$ coming from the spinors and talk about the Lagrangian of order $m_Q v^2$. The next order adds 4 bilinear terms

$$\begin{aligned} \mathcal{L}_Q^{(4)} \;=\; & c_1 \frac{1}{m_Q^3} \psi^\dagger \left(\mathbf{D}^2\right)^2 \psi \\ & + c_2 \frac{g}{m_Q^2} \psi^\dagger \left(\mathbf{D}\cdot\mathbf{E} - \mathbf{E}\cdot\mathbf{D}\right) \psi \\ & + c_3 \frac{ig}{m_Q^2} \psi^\dagger \vec{\sigma}\cdot\left(\mathbf{D}\times\mathbf{E} - \mathbf{E}\times\mathbf{D}\right) \psi \\ & + c_4 \frac{g}{m_Q} \psi^\dagger \vec{\sigma}\cdot\mathbf{B}\psi \end{aligned} \tag{3.21}$$

We have not included a term $1/m_Q \psi^\dagger D_0^2 \psi$ in $\mathcal{L}^{(4)}$, although it contributes to this order and has the right symmetry properties. Higher powers in the time derivative will spoil the simple numerical calculation of quark propagators to be discussed below. However, employing the lowest-order equation of motion one can replace each factor of iD_0 by $-\mathbf{D}^2/2m_Q$ after a suitable redefinition of the quark field.

The bilinear interactions Eq.(3.21) are not the whole story. There are, of course, quartic and higher-order terms that account for Green's functions with a larger number of external legs. The generic form of the four-quark contact interaction is

$$\mathcal{L}_{\rm contact} = \sum_j \frac{d_j}{m_Q^2} \left(\psi^\dagger T_j \chi\right)\left(\chi^\dagger T_j \psi\right) \,, \tag{3.22}$$

[3] We have not indicated those higher dimension gluon field operators that result from integrating out the relativistic degrees of freedom analogous to the Euler-Heisenberg effective Lagrangian in QED. They have no relevance for the $Q\bar{Q}$ bound state problem.

coupling	c_1	c_2	c_3	c_4	f_1	f_2	f_3
tree level	1/8	-1/8	-1/8	1/2	1/8	-3/64	-1/8

Table 3.3. *Tree level values of the NRQCD couplings c_i and f_i,*

where T_j is a spin-colour matrix. The couplings d_j have imaginary parts that determine the decay rates. Since for the Υ the latter are 10^4 times smaller than the excitation energies, we may safely neglect all interactions leading to quark-antiquark annihilation in the study of spectral quantities and work with a Lagrangian that strictly conserves the numbers of heavy quarks and antiquarks. Among the terms of order $m_Q v^6$ we take into account only the spin dependent ones. This way we consider spin splittings at next-to-leading order corresponding to an accuracy on the few percent level from naive power counting [43].

$$\begin{aligned} \mathcal{L}_Q^{(6)} \;=\; & f_1 \frac{g}{m_Q^3} \psi^\dagger \left\{\mathbf{D}^2, \vec{\sigma}\cdot\mathbf{B}\right\} \psi \\ & + f_2 \frac{ig}{m_Q^4} \psi^\dagger \left\{\mathbf{D}^2, \vec{\sigma}\cdot\left(\mathbf{D}\times\mathbf{E} - \mathbf{E}\times\mathbf{D}\right)\right\} \psi \\ & + f_3 \frac{ig^2}{m_Q^3} \psi^\dagger \vec{\sigma}\cdot\mathbf{E}\times\mathbf{E}\psi \,. \end{aligned} \tag{3.23}$$

The NRQCD Lagrangian coincides with the Lagrangian of the Heavy Quark Effective Theory (HQET). The difference between both effective theories lies in the power counting schemes. This is particularly obvious in the lowest-order part $\mathcal{L}^{(2)}$. Whereas operators in HQET may be ordered by dimension and therefore the static case yields a sensible limit, in NRQCD D_0 and $\mathbf{D}^2$ are of equal order which reflects the balancing of kinetic energy against potential energy. The static limit is inappropriate for heavy quarkonium. This further implies that NRQCD only shares heavy quark spin symmetry with HQET, but breaks flavour symmetry already at leading order.

The higher dimension operators in $\mathcal{L}_{\rm NRQCD}$ introduce new coupling constants. Item (d) of the recipe requires that they have to be tuned so that predictions in the effective theory match those of the underlying QCD. The tree level values given in Table 3.3 are provided by the Foldy-Wouthuysen-Tani transformation (see Appendix A). Generally, these coefficients depend on the cut-off, Λ_c and the coupling, $\alpha_S(m_Q)$. The estimates of α_S in Table 3.1 suggest that bottomonium really is perturbative at the b-quark scale. Therefore the matching may be done perturbatively by calculating low-energy scattering processes. The final choice of couplings will be discussed in 4.5, after the lattice cut-off will have been introduced.

3.2.4 The NRQCD Lagrangian in Euclidean Space-Time

In view of the lattice formulation to be introduced in the next chapter we Wick-rotate the coordinates, momenta and fields to obtain the NRQCD Lagrangian in Euclidean space-

time. This is accomplished by the following assignments

$$x_4^{(E)} = x_{(E)}^4 \equiv ix_{(M)}^0 = ix_0^{(M)} \tag{3.24}$$

$$x_j^{(E)} = x_{(E)}^j \equiv x_{(M)}^j = -x_j^{(M)} , \tag{3.25}$$

that imply

$$\partial_{(E)}^4 = \partial_4^{(E)} = -i\partial_0^{(M)} = -i\partial_{(M)}^0 \tag{3.26}$$

$$\partial_{(E)}^j = \partial_j^{(E)} = \partial_j^{(M)} = -\partial_{(M)}^j \tag{3.27}$$

$$A_{(E)}^4 = A_4^{(E)} = -iA_0^{(M)} = -iA_{(M)}^0 \tag{3.28}$$

$$A_{(E)}^j = A_j^{(E)} = A_j^{(M)} = -A_{(M)}^j \tag{3.29}$$

The rotation of the field strength tensor is determined from that of the covariant derivative

$$igF_{4i}^{(E)} = \left[D_4^{(E)}, D_i^{(E)}\right] = -i\left[D_0^{(M)}, D_i^{(M)}\right] = -i\left(igF_{0i}^{(M)}\right) , \tag{3.30}$$

$$igF_{ij}^{(E)} = \left[D_i^{(E)}, D_j^{(E)}\right] = \left[D_i^{(M)}, D_j^{(M)}\right] = igF_{ij}^{(M)} . \tag{3.31}$$

The chromoelectric field therefore transforms like $E_i^{(E)} \equiv F_{i4}^{(E)} = -iF_{i0}^{(M)} = -iE_i^{(M)}$, and the chromomagnetic field remains unaltered. The non-relativistic heavy quark Lagrangian in Euclidean space-time now reads

$$\begin{aligned}
\mathcal{L}_Q^{(E)} = & \\
& \psi^\dagger \Big[-D_4 + \frac{1}{2m_Q}\mathbf{D}^2 \\
& + \frac{g}{2m_Q}\vec{\sigma}\cdot\mathbf{B} - \frac{ig}{8m_Q^2}\left(\mathbf{D}\cdot\mathbf{E} - \mathbf{E}\cdot\mathbf{D}\right) + \frac{g}{8m_Q^2}\vec{\sigma}\cdot\left(\mathbf{D}\times\mathbf{E} - \mathbf{E}\times\mathbf{D}\right) + \frac{1}{8m_Q^3}(\mathbf{D}^2)^2 \\
& + \frac{1}{8m_Q^3}\{\mathbf{D}^2, g\vec{\sigma}\cdot\mathbf{B}\} + \frac{ig^2}{8m_Q^3}\vec{\sigma}\cdot(\mathbf{E}\times\mathbf{E}) + \frac{3g}{64m_Q^4}\{\mathbf{D}^2, \vec{\sigma}\cdot(\mathbf{D}\times\mathbf{E} - \mathbf{E}\times\mathbf{D})\} \\
& + \text{higher orders} \Big] \psi .
\end{aligned} \tag{3.32}$$

The antiquark Lagrangian is readily obtained as the charge conjugate of (3.32). With $\mathcal{C}\psi = -i\sigma_2\chi^*$ and $\mathcal{C}K_Q\mathcal{C}^{-1} = -\sigma_2 K_Q^*\sigma_2$ we have

$$\mathcal{L}_{\bar{Q}} \equiv \chi^\dagger K_{\bar{Q}}\chi = -\chi^\dagger K_Q^\dagger \chi , \tag{3.33}$$

hence

$$\begin{aligned}
\mathcal{L}_{\bar{Q}}^{(E)} = & \\
& \chi^\dagger \Big[-D_4 - \frac{1}{2m_Q}\mathbf{D}^2 \\
& - \frac{g}{2m_Q}\vec{\sigma}\cdot\mathbf{B} - \frac{ig}{8m_Q^2}\left(\mathbf{D}\cdot\mathbf{E} - \mathbf{E}\cdot\mathbf{D}\right) + \frac{g}{8m_Q^2}\vec{\sigma}\cdot\left(\mathbf{D}\times\mathbf{E} - \mathbf{E}\times\mathbf{D}\right) - \frac{1}{8m_Q^3}(\mathbf{D}^2)^2 \\
& - \frac{1}{8m_Q^3}\{\mathbf{D}^2, g\vec{\sigma}\cdot\mathbf{B}\} - \frac{ig^2}{8m_Q^3}\vec{\sigma}\cdot(\mathbf{E}\times\mathbf{E}) + \frac{3g}{64m_Q^4}\{\mathbf{D}^2, \vec{\sigma}\cdot(\mathbf{D}\times\mathbf{E} - \mathbf{E}\times\mathbf{D})\} \\
& + \text{higher orders} \Big] \chi .
\end{aligned} \tag{3.34}$$

3.3 Summary

We have introduced the NRQCD Lagrangian at next-to-leading order, i.e. with spin-independent interactions of order $O(m_b v^2)$ and $O(m_b v^4)$ and spin-dependent terms up to order $m_b v^6$. We anticipate that the non-relativistic theory is well suited for a non-perturbative treatment using a lattice regulator, since the heavy quark mass no longer appears as a dynamical scale. In the next chapter we shall discretise the above Lagrangian on a hypercubic lattice.

$\diamond$

Chapter 4

Lattice-Regularised NRQCD

In this chapter we formulate the lattice regularised version of NRQCD. The lattice spacing provides the cut-off which is required for the definition of the effective theory. As discussed in the previous chapter, a consistent choice requires $am_Q \sim 1$ which limits the resolution of lattices suited for NRQCD spectroscopy. In Section 4.1 we introduce the basic lattice operators that are building blocks of the discretised action. We subsequently develop the evolution equation of the heavy-quark propagator and discuss various approximations. Hereafter, meson correlation functions are constructed both for S- and P-wave states. In Section 4.4 we present our choice of wave function smearing as a crucial technical ingredient for extraction of excited-state signals. The chapter concludes with a discussion of the matching procedure to relate the effective theory and QCD. We shall apply a simple recipe known as tadpole renormalisation to circumvent a complicated perturbative calculation. This leaves us with two parameters, the bare coupling and heavy-quark mass, which are fixed through experimental input.

4.1 Basic Lattice Operators

The improved version of non-relativistic QCD for use in lattice simulations has been developed by LEPAGE ET.AL [43]. We repeat the main steps of their construction. To discretise the non-relativistic Lagrangian we define the following finite-difference operators

$$a\Delta_\mu^{(+)}\psi_x \equiv U_{x,\mu}\psi_{x+a\hat{\mu}} - \psi_x \,, \tag{4.1}$$

$$a\Delta_\mu^{(-)}\psi_x \equiv \psi_x - U^\dagger_{x-a\hat{\mu},\mu}\psi_{x-a\hat{\mu}} \,, \tag{4.2}$$

$$\Delta_\mu^{(\pm)} \equiv \frac{1}{2}\left(\Delta_\mu^{(+)} + \Delta_\mu^{(-)}\right) \,, \tag{4.3}$$

$$\Delta^{(2)} \equiv \sum_{i=1}^{3}\Delta_i^{(+)}\Delta_i^{(-)} = \sum_{i=1}^{3}\Delta_i^{(-)}\Delta_i^{(+)} \,. \tag{4.4}$$

As before, a denotes the lattice spacing, $U_{x,\mu}$ the link variable at x in μ-direction and ψ the fermionic degrees of freedom.
Invoking the connection of the link variable to the gluon field Eq.(2.13), we can relate the lattice difference operators with the continuum covariant derivatives

$$\Delta_\mu^{(+)} = \frac{1}{a}\left(\mathrm{e}^{aD_\mu} - 1\right) = \frac{1}{a}\sum_{n=1}^{\infty}\frac{(aD_\mu)^n}{n!} \,, \tag{4.5}$$

$$\Delta_\mu^{(-)} = \frac{1}{a}\left(1 - \mathrm{e}^{-aD_\mu}\right) = \frac{1}{a}\sum_{n=1}^{\infty}\frac{(-1)^{n-1}}{n!}(aD_\mu)^n \,, \tag{4.6}$$

$$\Delta_\mu^{(\pm)} = \frac{1}{a}\sum_{n=0}^{\infty}\frac{(aD_\mu)^{2n+1}}{(2n+1)!}\,, \tag{4.7}$$

$$\Delta_\mu^{(+)}\Delta_\mu^{(-)} = \frac{1}{a^2}\sum_{n,m=1}^{\infty}\frac{(-1)^{m-1}}{n!m!}(aD_\mu)^{n+m} \quad \text{no summation over } \mu\,. \tag{4.8}$$

It can immediately be checked that the symmetric difference and the Laplacian reproduce their continuum counterparts up to $O(a^2)$:

$$\begin{aligned}\Delta_\mu^{(\pm)} &= D_\mu + O(a^2)\,,\\ \Delta^{(2)} &= \mathbf{D}^2 + O(a^2)\,.\end{aligned} \tag{4.9}$$

Expansions 4.5-4.8 can be used to remove leading cut-off effects on a classical level. We have, for instance,

$$\Delta_\mu^{(\pm)} = D_\mu + \frac{a^2}{6}D_\mu^3 + O(a^4)\,. \tag{4.10}$$

To remove the cubic term we observe that

$$\Delta_\mu^{(+)}\Delta_\mu^{(\pm)}\Delta_\mu^{(-)} = D_\mu^3 + O(a^2)\,, \tag{4.11}$$

so that an improved derivative can be defined as

$$\tilde{\Delta}_\mu^{(\pm)} \equiv \Delta_\mu^{(\pm)} - \frac{a^2}{6}\Delta_\mu^{(+)}\Delta_\mu^{(\pm)}\Delta_\mu^{(-)} = D_\mu + O(a^4)\,. \tag{4.12}$$

Analogously

$$\begin{aligned}\Delta_i^{(+)}\Delta_i^{(-)} &= \frac{1}{a^2}\sum_{n,m=1}^{\infty}\frac{(-1)^{m-1}}{n!m!}(aD_i)^{n+m}\\ &= D_i^2 + \frac{a^2}{12}D_i^4 + O(a^4)\,,\end{aligned} \tag{4.13}$$

hence

$$\tilde{\Delta}^{(2)} \equiv \Delta^{(2)} - \frac{a^2}{12}\sum_{i=1}^{3}\left(\Delta_i^{(+)}\Delta_i^{(-)}\right)^2 + O(a^4)\,. \tag{4.14}$$

Field strength tensor

A symmetric representation of the field strength tensor on the lattice is the cloverleaf operator that is defined on the grid points

$$F_{\mu\nu,x}^{(c)} \equiv \frac{1}{4a^2 g}\left[\frac{1}{2i}\left(M_{\mu\nu,x} - M_{\mu\nu,x}^\dagger\right) - \frac{1}{3}\Im\,\mathrm{Tr}\,M_{\mu\nu,x}\right] \tag{4.15}$$

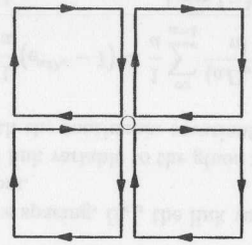

Figure 4.1. *Cloverleaf representation of the lattice field strength tensor.*

and

$$M_{\mu\nu,x} \equiv \sum_{(\alpha,\beta)_{\mu\nu}} U_{\alpha\beta,x}\,. \tag{4.16}$$

The sum covers the four plaquettes in the $\mu\nu$-plane surrounding the space-time point x as indicated in Figure 4.1. The field strength tensor defined this way carries discretisation errors of $O(a^2)$. It will prove useful to introduce an improved version of $F_{\mu\nu}^{(c)}$ which is correct through order a^4:

$$\tilde{F}_{\mu\nu,x}^{(c)} \equiv \frac{5}{3}F_{\mu\nu}^{(c)} - \frac{1}{6}\left[U_{x,\mu}F_{\mu\nu,x+a\hat{\mu}}^{(c)}U_{x,\mu}^\dagger + U_{x-a\hat{\mu},\mu}^\dagger F_{\mu\nu,x-a\hat{\mu}}^{(c)}U_{x-a\hat{\mu},\mu} - (\mu\leftrightarrow\nu)\right]\,. \tag{4.17}$$

4.2 Quark Propagator Evolution

The Lagrangian Eq.(3.32) yields the following Schrödinger evolution equation of the heavy quark propagator

$$\partial_4 G(x,y) = \left(-igA_4 + \frac{\mathbf{D}^2}{2m_Q} - \delta\mathcal{L}\right)G(x,y)\,, \tag{4.18}$$

where $\delta\mathcal{L}$ includes the relativistic corrections. The solution to the initial value problem

$$G(x,y)|_{x_4=y_4} = \delta^3(\mathbf{x}-\mathbf{y}) \tag{4.19}$$

is given by

$$G(x,y) = \mathrm{T}\exp\left[\int_{y_4}^{x_4} dt\left(-igA_4 + \frac{\mathbf{D}^2}{2m_Q} - \delta\mathcal{L}\right)\right]\delta^3(\mathbf{x}-\mathbf{y})\,. \tag{4.20}$$

Temporal discretisation

We will compute G with a simple, fully explicit integration scheme in a single pass through the lattice. This is a big advantage compared to the iterative solution of the boundary

value problem in the relativistic theory. On a discrete time axis with lattice spacing a, Eq.(4.20) induces the following recursion formula

$$G(\mathbf{x}, x_4 + a; y) = \exp\left(a\left[-igA_4 + \frac{\mathbf{D}^2}{2m_Q} - \delta\mathcal{L}\right]\right) G(\mathbf{x}, x_4; y)\,, \tag{4.21}$$

with the lattice gluon field evaluated at mid-link. As an immediate consequence of the Baker-Campbell-Hausdorff formula, we have for sufficiently small lattice spacing

$$\exp(aX_1)\ldots\exp(aX_k) = \exp\left(a\sum_{l=1}^{k} X_l + \frac{1}{2}a^2\sum_{l<m}[X_l, X_m] + R(a)\right) \tag{4.22}$$

with the rest vanishing like $\lim_{a\to 0} a^{-2}R(a) = 0$. Using Eq.(4.22) we obtain a simplified evolution equation

$$G(\mathbf{x}, x_4 + a; y) = \exp\left(\frac{a\mathbf{D}^2}{4m_Q}\right)\exp\left(-\frac{a\delta\mathcal{L}}{2}\right)U^\dagger_{x,4}\exp\left(-\frac{a\delta\mathcal{L}}{2}\right)\exp\left(\frac{a\mathbf{D}^2}{4m_Q}\right)G(\mathbf{x}, x_4; y)\,. \tag{4.23}$$

Note that by the symmetric choice in Eq.(4.23), the commutators in Eq.(4.22) vanish and the error introduced in the Lagrangian is due to double commutators that are at least of order v^6 for spin-independent terms and of order v^8 for spin-dependent ones. With the same reasoning one can neglect quadratic terms in $\delta\mathcal{L}$

$$\exp\left(-\frac{a\delta\mathcal{L}}{2}\right) \to 1 - \frac{a}{2}\delta\mathcal{L}\,. \tag{4.24}$$

Finally let us replace the remaining exponentials by a fixed power

$$\exp\left(\frac{a\mathbf{D}^2}{4m_Q}\right) \to \left(1 + \frac{a\mathbf{D}^2}{4nm_Q}\right)^n\,. \tag{4.25}$$

This way we introduce an error that has to be corrected for by adding a term $a\,(\mathbf{D}^2)^2/(32\,n\,m_Q^2)$, so that

$$\exp\left(\frac{a\mathbf{D}^2}{4m_Q}\right) = \left(1 + \frac{a}{n}\left(\frac{\mathbf{D}^2}{4m_Q} + \frac{a}{2n}\frac{(\mathbf{D}^2)^2}{16m_Q^2}\right)\right)^n + O(v^6)\,. \tag{4.26}$$

Spatial discretisation

We adopt the notation that is widely used in the Lattice NRQCD literature and denote the lowest-order discretisation of the kinetic term by H_0,

$$H_0 = -\frac{\Delta^{(2)}}{2m_Q}\,, \tag{4.27}$$

the corrected version, including the compensation of the leading temporal discretisation error, by $\tilde{H}_0$,

$$\tilde{H}_0 = -\frac{\tilde{\Delta}^{(2)}}{2m_Q} - \frac{a}{4n}\frac{(\Delta^{(2)})^2}{4m_Q^2}\,. \tag{4.28}$$

The continuum operators belonging to the relativistic corrections of order $m_Q v^4$ are easily transcribed using the formulae Eqs.(4.1)-(4.4) or their improved versions

$$V_1 = -c_1\frac{(\Delta^{(2)})^2}{8m_Q^3}\,, \tag{4.29}$$

$$V_2 = c_2\frac{ig}{8m_Q^2}\left(\Delta^{(\pm)}\cdot\mathbf{E}^{(c)} - \mathbf{E}^{(c)}\cdot\Delta^{(\pm)}\right)\,, \tag{4.30}$$

$$V_3 = -c_3\frac{g}{8m_Q^2}\vec{\sigma}\cdot\left(\tilde{\Delta}^{(\pm)}\times\tilde{\mathbf{E}}^{(c)} - \tilde{\mathbf{E}}^{(c)}\times\tilde{\Delta}^{(\pm)}\right)\,, \tag{4.31}$$

$$V_4 = -c_4\frac{g}{2m_Q}\vec{\sigma}\cdot\tilde{\mathbf{B}}^{(c)}\,. \tag{4.32}$$

Difference operators act on all fields to their right. Finite-a corrections have been included in the spin-dependent terms only, since they can be of the same order as $O(m_Q v^6)$ relativistic corrections. Note that we have redefined the coefficients c_i, so that they equal one at tree level. The chromoelectric and chromomagnetic fields are defined in analogy to their continuum counterparts: $E_k^{(c)} \equiv F_{k4}^{(c)}$ and $B_k^{(c)} \equiv -\frac{1}{2}\epsilon_{kij}F_{ij}^{(c)}$. Finally the $O(m_Q v^6)$ corrections are

$$V_5 = -c_5\frac{g}{8m_Q^3}\left\{\Delta^{(2)}, \vec{\sigma}\cdot\mathbf{B}^{(c)}\right\}\,, \tag{4.33}$$

$$V_6 = -c_6\frac{3g}{64m_Q^4}\left\{\Delta^{(2)}, \vec{\sigma}\cdot\left(\Delta^{(\pm)}\times\mathbf{E}^{(c)} - \mathbf{E}^{(c)}\times\Delta^{(\pm)}\right)\right\}\,, \tag{4.34}$$

$$V_7 = -c_7\frac{ig^2}{8m_Q^3}\vec{\sigma}\cdot\mathbf{E}^{(c)}\times\mathbf{E}^{(c)}\,. \tag{4.35}$$

With these transcriptions we arrive at a heavy quark evolution that is consistently discretised: all remaining cut-off effects are moved to higher orders in the effective Lagrangian:

$$G_{\mathbf{x},x_4+a;y} = \left(1 - \frac{a\tilde{H}_0}{2n}\right)^n\left(1 - \frac{a}{2}\sum_{k=1}^{7}c_kV_k\right)U^\dagger_{x,4}\left(1 - \frac{a}{2}\sum_{k=1}^{7}c_kV_k\right)\left(1 - \frac{a\tilde{H}_0}{2n}\right)^n G_{\mathbf{x},x_4;y}\,. \tag{4.36}$$

The use of Eq.(4.36) as it stands will be rather costly in practice. The complete set of relativistic correction terms is twice applied which slows down the evolution significantly. Therefore we have implemented a modified version in the actual simulation:

$$G_{\mathbf{x},x_4+a;y} = \left(1 - \frac{aH_0}{2n}\right)^n U^\dagger_{x,4}\left(1 - \frac{aH_0}{2n}\right)^n\left(1 - a\sum_{k=1}^{9}c_kV_k\right)G_{\mathbf{x},x_4;y}\,. \tag{4.37}$$

The modifications are: (i) in the first factor $\tilde{H}_0$ is replaced by H_0; (ii) $\delta\mathcal{L}$ is applied only once and commuted with the last factor; (ii) the finite a corrections are moved from $\tilde{H}_0$ into $\delta\mathcal{L}$:

$$V_8 = c_8 \frac{a^2\Delta^{(4)}}{24m_Q}, \tag{4.38}$$

$$V_9 = -c_9 \frac{a(\Delta^{(2)})^2}{16nm_Q^2}, \tag{4.39}$$

where $\Delta^{(4)} \equiv \sum_{i=1}^{3} \left(\Delta_i^{(+)}\Delta_i^{(-)}\right)^2$.

Numerical stability

The forward time integration scheme becomes unstable if the temporal lattice spacing is too large. Consider the lowest-order, free field limit of Eq.(4.37),

$$G_{\mathbf{x},x_4+a;y} = \left(1 + \frac{a\Delta^{(2)}_{\text{free}}}{2nm_Q}\right)^n G_{\mathbf{x},x_4;y}\,. \tag{4.40}$$

For $n = 1$, the von Neumann analysis leads to an amplification factor of

$$\xi = 1 - \frac{4}{2m_Q a}\sum_{i=1}^{3}\sin^2\left(\frac{ap_i}{2}\right), \tag{4.41}$$

which implies the stability criterion

$$\left|\frac{4}{2m_Q a}\sum_{i=1}^{3}\sin^2\left(\frac{ap_i}{2}\right)\right| \leq \frac{12}{2m_Q a} < 2\,. \tag{4.42}$$

This is the well-known result for the diffusion equation with diffusion coefficient $D = a/2m_Q$ and equal temporal and spatial discretisation steps. Eq.(4.42) constrains the mass to $am_Q > 3$. To study quarks with smaller masses one might either reduce the temporal lattice spacing or improve the integration scheme. By choosing $n > 1$ in Eq.(4.40) one obtains a better approximation of the exponential and the mass constraint is weakened to $am_Q > 3/n$. This amounts to an effective reduction of the time step which is incomplete, however, since the gauge fields are not evaluated on the intermediate points.

4.3 Building up Meson Correlation Functions

We proceed by constructing two-point functions from quark propagators through a generic time-slice operator [1]

$$H(t) \equiv \sum_{\mathbf{x}_1,\mathbf{x}_2} \bar{h}_{\mathbf{x}_1 t}\,\Omega\,\Phi_{\mathbf{x}_1,\mathbf{x}_2}\,h_{\mathbf{x}_2 t}\,. \tag{4.43}$$

[1] In the following we will mainly use t instead of x_4 for the time coordinate.

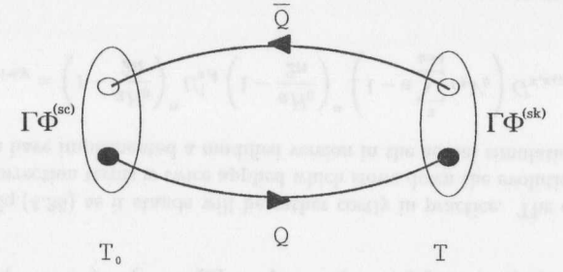

Figure 4.2. *Sketch of quark lines for a general non-local flavour non-singlet meson two-point function.*

h is the heavy quark spinor, Ω a 4-by-4 spin matrix and Φ smears the quark fields over the lattice to increase the overlap with a certain radial or orbital momentum state. In the non-relativistic theory, h really is a Pauli spinor hence

$$\begin{aligned} H(t) &= \sum_{\mathbf{x}_1,\mathbf{x}_2}\left(0, \chi^\dagger_{\mathbf{x}_1 t}\right)\gamma_4\,\Omega\,\Phi_{\mathbf{x}_1,\mathbf{x}_2}\begin{pmatrix}\psi_{\mathbf{x}_2 t}\\ 0\end{pmatrix} \\ &= -\sum_{\mathbf{x}_1,\mathbf{x}_2}\chi^\dagger_{\mathbf{x}_1 t}\,\Gamma^\dagger\,\Phi_{\mathbf{x}_1,\mathbf{x}_2}\,\psi_{\mathbf{x}_2 t}\,, \end{aligned} \tag{4.44}$$

where $\Gamma^\dagger \equiv \Omega_{21}$ is now a 2-by-2 matrix in spin space. We use the decomposition of the relativistic spinor as in 3.2.1, i.e. ψ annihilates a quark state whereas χ creates an antiquark state. The opposite holds for the hermitian-conjugate fields. An obvious advantage of heavy quarkonium is that potential models can provide very accurate wave functions as input for the *smearing function* Φ. With 4.44 we compute the two-point correlator

$$\begin{aligned} \left\langle H(t)H^\dagger(t_0)\right\rangle &= \sum\left\langle \chi^\dagger_{\alpha a x_1 t}\,\Gamma^\dagger_{\alpha\beta}\,\Phi^{(sk)}_{\mathbf{x}_1,\mathbf{x}_2}\,\psi_{\beta a x_2 t}\,\psi^\dagger_{\gamma b y_2 t_0}\,\Phi^{(sc)*}_{y_1,y_2}\,\Gamma_{\gamma\delta}\,\chi_{\delta b y_1 t_0}\right\rangle \\ &= \sum\left\langle \chi^\dagger_{\alpha a x_1 t}\,\chi_{\delta b y_1 t_0}\right\rangle\Gamma^\dagger_{\alpha\beta}\,\Phi^{(sk)}_{\mathbf{x}_1,\mathbf{x}_2}\left\langle \psi_{\beta a x_2 t}\,\psi^\dagger_{\gamma b y_2 t_0}\right\rangle\Phi^{(sc)*}_{y_1,y_2}\,\Gamma_{\gamma\delta} \\ &= \sum G^{\bar{Q}}_{\alpha a x_1 t,\delta b y_1 t_0}\,\Gamma^\dagger_{\alpha\beta}\,\Phi^{(sk)}_{\mathbf{x}_1,\mathbf{x}_2}\,G^{Q}_{\beta a x_2 t,\gamma b y_2 t_0}\,\Phi^{(sc)*}_{y_1,y_2}\,\Gamma_{\gamma\delta} \\ &= \sum G^{Q\dagger}_{\delta b x_1 t,\alpha a y_1 t_0}\,\Gamma^\dagger_{\alpha\beta}\,\Phi^{(sk)}_{\mathbf{x}_1,\mathbf{x}_2}\,G^{Q}_{\beta a x_2 t,\gamma b y_2 t_0}\,\Phi^{(sc)*}_{y_1,y_2}\,\Gamma_{\gamma\delta} \end{aligned} \tag{4.45}$$

The last expression can be simplified using the translational invariance of the quark propagator,

$$\begin{aligned} \left\langle H(t)H^\dagger(t_0)\right\rangle &= \sum_{\mathbf{x}_1,\mathbf{x}_2,y_1,y_2}\mathrm{Tr}_{c\otimes s}\left[G^{Q\dagger}_{\mathbf{x}_1 t,y_1 t_0}\,\Gamma^\dagger\,\Phi^{(sk)}_{\mathbf{x}_1,\mathbf{x}_2}\,G^{Q}_{\mathbf{x}_2 t,y_2 t_0}\,\Phi^{(sc)*}_{y_1,y_2}\,\Gamma\right] \\ &= L^3\sum_{\mathbf{x}_1,\mathbf{x}_2,y_2}\mathrm{Tr}_{c\otimes s}\left[G^{Q\dagger}_{\mathbf{x}_1 t,y_1 t_0}\,\Gamma^\dagger\,\Phi^{(sk)}_{\mathbf{x}_1-\mathbf{x}_2}\,G^{Q}_{\mathbf{x}_2+y_1-y_2 t,y_1 t_0}\,\Phi^{(sc)*}_{y_1-y_2}\,\Gamma\right] \\ &= L^3\sum_{\mathbf{x}_1,\mathbf{x}_2}\mathrm{Tr}_{c\otimes s}\left[G^{Q\dagger}_{\mathbf{x}_1 t,y_1 t_0}\,\Gamma^\dagger\,\Phi^{(sk)}_{\mathbf{x}_1-\mathbf{x}_2}\,\tilde{G}^{Q}_{\mathbf{x}_2 t,y_1 t_0}\right]. \end{aligned} \tag{4.46}$$

non-relativistic notation	lowest continuum irrep	lattice irrep	operator Γ
$^1S_0$	0^{-+}	A_1^{-+}	$\hat{1}$
$^3S_1$	1^{--}	$T_{1(i)}^{--}$	σ_i
$^1P_1$	1^{+-}	$T_{1(i)}^{+-}$	Δ_i
$^3P_0$	0^{++}	A_1^{++}	$\sum_{j=1}^{3}\Delta_j\sigma_j$
$^3P_1$	1^{++}	$T_{1(k)}^{++}$	$\Delta_i\sigma_j-\Delta_j\sigma_i$
$^3P_2$	2^{++}	$E_{(k)}^{++}$	$\Delta_i\sigma_i-\Delta_j\sigma_j$
		$T_{2(ij)}^{++}$	$\Delta_i\sigma_j+\Delta_j\sigma_i$

Table 4.1. *Spin operators for different lattice irreducible representations.*

with the initial antiquark position, $\mathbf{y}_1$, fixed. The source-smeared propagator reads

$$\tilde{G}^Q_{\mathbf{x}_2 t,\mathbf{y}_1 t_0}=\sum_{\mathbf{z}} G^Q_{\mathbf{x}_2-\mathbf{z}t,\mathbf{y}_1 t_0}\,\Gamma\,\Phi^{(sc)}_{\mathbf{z}}\,. \tag{4.47}$$

It is obtained directly from the NRQCD evolution by replacing the delta function source with the extended source $\Phi^{(sc)}_{\mathbf{x}}$.

4.4 Smearing Technique

Since we are not only interested in ground states but in one or two radially excited levels, special care has to be taken in choosing the spatial distribution of quark and antiquark fields in the hadron operator as given by the smearing function, Φ. Fortunately, we have a detailed picture of what the wave function of a heavy-heavy bound state should look like from the study of non-relativistic quark models, which is a considerable advantage compared to light hadron calculations. Richardson potential wave functions, for example, have proven successful in earlier simulations [47]. Even simple hydrogen wave functions have been applied in charmonium spectroscopy and are the natural choice for heavy-light systems.

Here, we will pursue a somewhat more refined strategy to obtain adequate smearing functions: We use Schrödunger wave functions computed from a radial potential which is extracted from a lattice simulation. We benefit from a recent lattice determination of the $b\bar{b}$ potential including relativistic corrections [107, 106, 111]. The authors start from the $O(v^4)$ effective Breit-Fermi Hamiltonian [112, 113], which in the center-of-mass frame of the quark and antiquark, has the form

$$\begin{aligned} H &= \sum_{i=1,2}\left[m_i+\frac{\mathbf{p}^2}{2m_i}-\frac{\mathbf{p}^4}{8m_i^3}+\frac{1}{8m_i^2}\Delta\left(V_0(r)+V_a(r)\right)\right] \\ &\quad +V_0(r)+V_{SD}(r,\mathbf{L},\mathbf{S_1},\mathbf{S_2})+V_{VD}(r,\mathbf{p})\,. \end{aligned} \tag{4.48}$$

It contains the central potential of Cornell type:

$$V_0(r)=V_{\text{self}}+\sigma r-\frac{e}{r}\,, \tag{4.49}$$

spin-dependent interactions with spin-orbit, tensor and spin-spin structure:

$$V_{SD}(r,\mathbf{L},\mathbf{S_1},\mathbf{S_2})=V_{LS}(r)+V_T(r)+V_{SS}(r)\,, \tag{4.50}$$

velocity-dependent potentials, V_{VD}, and V_a as part of the Darwin term. We have to refer the reader to Refs. [107, 106, 111] for a detailed description of the form of these potentials as well as their computation from Wilson loop expectation values with colour field insertions. Following [111], we numerically integrate the radial Schrödinger equation[2]

$$\frac{d^2g_{E,l}(r)}{dr^2}=F(r,E,l,\alpha,m,\sigma)g_{E,l}(r) \tag{4.51}$$

for definite radial quantum number and angular momentum , where

$$F(r,E,l,\alpha,m,\sigma)\equiv\frac{l(l+1)}{r^2}-m\left(E-\sigma r+\frac{\alpha}{r}\right)\,. \tag{4.52}$$

The term $-\alpha/r$ contains the Coulomb term of the central potential, the $1/r$ contribution to the Darwin interaction, and the leading $1/r$ contribution from V_{VD}:

$$\alpha=\frac{12m^2e+3h-4\sigma}{12m^2}\,. \tag{4.53}$$

We leave m and σ as free parameters which are determined by a fit to the experimental spectrum. The contributions of the terms not coming from the central potential are fixed to the lattice values found in [111]. The Coulomb coefficient, e is that of the quenched simulation in [111] augmented by 20% to take into account the different running at short distances observed in [83]. Figs. (4.3) and (4.4) display the solutions of (4.51) corresponding to the three smallest eigenvalues with $L=0$ and the two lowest $L=1$ states, respectively.

The continuum wave functions are converted to the lattice using the scales obtained from SESAM's ρ masses for each hopping parameter. We average correlators over different polarisations corresponding to the cartesian projections of wave functions

$$\Phi_1=\frac{g_{E,l}(r)}{r}\frac{x}{r}\,,\quad \Phi_2=\frac{g_{E,l}(r)}{r}\frac{y}{r}\,,\quad \Phi_3=\frac{g_{E,l}(r)}{r}\frac{z}{r}\,. \tag{4.54}$$

Note, that the finite-difference operators included in Table 4.1 for the P states are only applied in the case of δ-function smearing.

Contrary to gauge-invariant smearing procedures like iterative WUPPERTAL smearing [114, 115], the use of wave functions as described above requires a fixed gauge. The appropriate choice is Coulomb gauge which minimises the spatial gluon field. The configurations are numerically fixed to that gauge using the algorithm described in [116]. We benefit from an efficient parallel implementation on the Connection Machine CM5 which is discussed in [117, 118] [3].

[2] In Ref. [111] the Numerov method is applied to integrate the differential equation. It introduces step size errors of $O((\Delta r)^5)$. The analytic expression for the regular solution in the limit $r\to 0$ provides the starting point for the integration. We thank A. Wachter for the kind donation of these routines.

[3] We thank H. Suman, who kindly provided the gauge fixing routines.

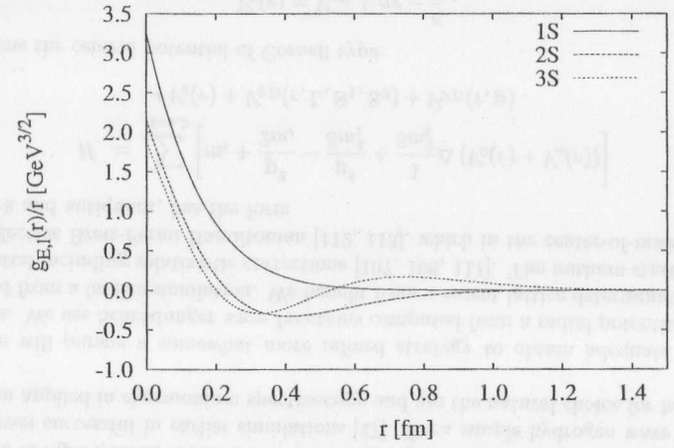

Figure 4.3. *Normalised radial eigenfunctions for S-wave $b\bar{b}$ bound states.*

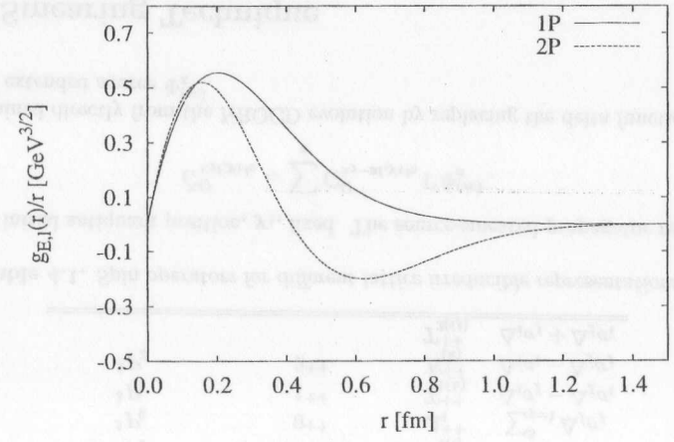

Figure 4.4. *Normalised radial eigenfunctions for P-wave $b\bar{b}$ bound states .*

For each wave function a separate quark propagator has to be calculated since the fastest way to implement source smearing is to use Φ as the start vector for the evolution of G_T. Sink smearing is realised by convoluting the local antiquark propagator with the smearing function and combining it with G_T according to the given Dirac structure. The convolution is efficiently computed via a parallelised version of the FFT algorithm[4]. It is reasonable to use the same smearing function for states that differ only in spin orientation: spin-interactions are relativistic corrections and will not change the wave function significantly. Nevertheless, we are left with as many as 13 propagators to evolve: four different smearings for S states using the ground state, the first and second excited state wave functions as well as the delta function (local operator); nine smearings for P states including the ground state, the first excitation and the local propagator for each polarisation. All cross correlators are calculated resulting in the following 4-by-4 matrix of correlation functions in the case of S states (3-by-3 for P states)

$$(C_{\mathrm{sc,sk}}) = \begin{bmatrix} (l|l) & (l|1) & (l|2) & (l|3) \\ (1|l) & (1|1) & (1|2) & (1|3) \\ (2|l) & (2|1) & (2|2) & (2|3) \\ (3|l) & (3|1) & (3|2) & (3|3) \end{bmatrix}, \tag{4.55}$$

where the type of smearing is indicated by indices *sc* and *sk* that may have the values l for $\Phi = \delta$, 1 for the ground state wave function $\Phi = \Phi^{(1)}$, etc. . Clearly, one is restricted to a small number of levels compared to the potential model approach. A reliable estimate of the second radial excitation turns out to be rather hard, for obvious reasons: first, the correlation function will eventually be dominated by the ground state; second, the signal to noise exponentially decreases with the energy difference.

4.5 Matching NRQCD and QCD

The couplings in the NRQCD Lagrangian have to be adjusted in order that predictions for low-energy observables in the effective theory match those of QCD. In lowest order NRQCD there are two parameters: the bare gauge coupling, g and the bare heavy quark mass, m_Q. The v^2-improved Lagrangian adds the five couplings $c_1, \ldots c_5$. Finally, in the $O(m_Q v^6)$ accurate form we have to cope with 11 couplings.

An obvious way to fix the unknown parameters is by non-perturbatively matching the two theories: for a number of bound states require the mass calculated in NRQCD to equal that predicted by QCD. To make things easier, the latter is usually replaced by the experimental mass. However, as we include more interaction terms to improve accuracy non-perturbative matching clearly will spoil the predictive power of the method. This is avoided if the matching is done perturbatively. The use of PT may be justified if the heavy quark mass which serves as the cut-off is large enough. Perturbative matching proceeds by computing physical observables, like scattering amplitudes, between asymptotic $Q,\bar{Q}$ and gluon states both in QCD and NRQCD. The result is expanded in powers of $\mathbf{p}/m_Q$ and the couplings are tuned so that the series coincide to the desired order.

[4] We make use of the CMSSL library routines supplied for the CMFortran compiler.

In Lattice NRQCD we combine the perturbative and non-perturbative matching techniques: while g and $M_Q = am_Q$ are fixed using level splittings of onium states and the kinetic mass of the ground state respectively, the remaining parameters, c_i are determined perturbatively. However, perturbative series in the bare lattice coupling are known to be poorly convergent. A large renormalisation is needed to connect g to some physical coupling. This is due to tadpole contributions caused by the nonlinear mapping of the lattice gauge field onto the continuum, as was anticipated by PARISI [119] and worked out in detail by LEPAGE and MACKENZIE [18, 120].

4.5.1 Tadpole Improvement

The naive connection between the link variable and the continuum gauge field,

$$U_{x,\mu} \to 1 + iagA_\mu\left(x + \frac{a}{2}\hat{\mu}\right) , \tag{4.56}$$

suggests that higher order corrections vanish as powers of the lattice spacing which is not true in the quantum theory. For instance, the tadpole contribution to the link expectation value, $\langle A_\mu A_\mu \rangle$ is suppressed only by g^2 (i.e. $(\ln a)^{-1}$ and not a) as the quadratic divergence cancels two powers of the lattice spacing. This correction is large at intermediate a and leads to a vacuum expectation value of the link variable in Landau gauge which is considerably smaller than 1. A simple way to account for the bulk of the effect is to divide every link by a *mean-field parameter* u_0, a number between 0 and 1, that contains the averaged ultraviolet modes

$$U_{x,\mu} \to U_{x,\mu}/u_0 . \tag{4.57}$$

Practically, u_0 is measured in the simulation . Its definition is, of course, not unique. [5] A simple, gauge invariant prescription uses the plaquette value

$$u_0^P \equiv \sqrt[4]{\langle \frac{1}{3}\mathrm{Tr}\, U_{\mu\nu}\rangle} . \tag{4.58}$$

A better motivated choice is to calculate u_0 directly from the single link expectation value in Landau gauge

$$u_0^L \equiv \langle \frac{1}{3}\mathrm{Tr}\, U_\mu \rangle_{LG} . \tag{4.59}$$

Landau gauge maximises $\langle \mathrm{Tr}\, U_\mu \rangle$, i.e. pushes it as close to 1 as possible, and thus isolates the gauge-independent tadpole contribution. A recent NRQCD lattice calculation of the hyperfine splitting in $c\bar{c}$, $b\bar{c}$ and $b\bar{b}$ bound states over a variety of lattice spacings suggests that this choice improves the scaling behaviour of spectroscopic quantities [121, 44]. This view is also endorsed in Refs. [51, 122] where the authors have studied the scaling behaviour in the quenched $b\bar{b}$ spectrum using three values of the coupling ($\beta = 5.7, 6.0, 6.2$), an $O(m_b v^4)$-correct action and the plaquette tadpole value (defined below). They find

[5] Other choices than those discussed here are based upon extended Wilson loops or the critical hopping parameter for Wilson quarks [18].

u_0	$\kappa = 0.156$	$\kappa = 0.157$	$\kappa = 0.1575$	quenched
$u_0^P = \sqrt[4]{\langle \frac{1}{3}\mathrm{Tr}\, U_{\mu\nu}\rangle}$	0.8688	0.8695	0.8697	0.8778
$u_0^L = \langle \frac{1}{3}\mathrm{Tr}\, U_\mu \rangle_{\mathrm{LG}}$	0.8499	0.8519	0.8529	0.8608

Table 4.2. *Comparison of tadpole schemes for different gauge field samples.*

the spin-independent spectrum to display insignificant scaling violations whereas the hyperfine splittings do not scale that well. This is attributed partly to $O(a^2)$ errors in the B field [6] arising in the term $\sigma \cdot B$ but partly also to the choice of plaquette tadpole improvement not capturing the tadpole effects sufficiently well. Additionally, two more arguments in favour of u_0^L are given in [52]: firstly, the static potential shows less violation of rotational invariance using a u_0^L-tadpole improved gluonic action and, secondly, the non-perturbative determination of the clover coefficient c_{SW} for Sheikholeslami-Wohlert quarks [19] is in good agreement with the u_0^L-tadpole improved perturbative result. On a fine lattice, $a \approx 0.1$fm, u_0^P and u_0^L differ by about 2%, Table 4.2. Note, however that u_0 weights the field strength tensor with four powers,

$$\mathbf{E} \to \mathbf{E}/u_0^4 , \qquad \mathbf{B} \to \mathbf{B}/u_0^4 \tag{4.60}$$

so that, naively, using u_0^P instead of u_0^L may change the hyperfine splittings by as much as 8%.

The tadpole-improved operators may be considered an efficient starting point for a perturbative expansion of the couplings c_i,

$$c_i(g, M_Q) = c_i^0 + c_i^1 g^2 + \ldots , \tag{4.61}$$

in the sense that radiative corrections are now expected to be small. This has been demonstrated for those terms in the NRQCD action which contribute to the heavy quark self-energy by MORNINGSTAR [123]. Therefore we feel justified to neglect the higher order corrections: all calculations presented in the following have been obtained with tadpole improvement and tree-level values $c_i = 1$. We are then left with only two parameters, g and M_Q, which are the ones in the QCD Lagrangian.

4.5.2 Setting the Scale

The lattice spacing is fixed using the lowest radial and orbital angular momentum splittings in the bottomonium system. Empirically, they are independent of the the heavy quark mass to a very good approximation which allows for a determination of a^{-1} without carefully tuning the bare b-quark mass. Invoking a phenomenological assumption for the typical momentum transfer within $b\bar{b}$ bound states, one may conclude that these splittings are insensitive to vacuum polarisation effects too. These statements will be numerically validated in later chapters.

[6] which was obtained fom the unimproved field strength tensor, Eq.(4.15).

state	J^{PC}	mass
$\Upsilon(1S)$	1^{--}	9460.37 ± 0.21 MeV
$\chi_{b0}(1P)$	0^{++}	9859.8 ± 1.3 MeV
$\chi_{b1}(1P)$	1^{++}	9891.9 ± 0.7 MeV
$\chi_{b2}(1P)$	2^{++}	9913.2 ± 0.6 MeV
$\Upsilon(2S)$	1^{--}	10023.30 ± 0.31 MeV

Table 4.3. *Experimental masses used in the lattice scale determination.*

Practically, we will use the average of two spacings to convert lattice data into physical units:

$$a^{-1}(2^3S_1 - 1^3S_1) \equiv \frac{m(\Upsilon') - m(\Upsilon)}{am(2^3S_1) - am(1^3S_1)} = \frac{0.5629 \text{ GeV}}{am(2^3S_1) - am(1^3S_1)}, \quad (4.62)$$

$$a^{-1}(1^3\bar{P} - 1^3S_1) \equiv \frac{m(\bar{\chi}_b) - m(\Upsilon)}{am(1^3\bar{P}) - am(1^3S_1)} = \frac{0.4398 \text{ GeV}}{am(1^3\bar{P}) - am(1^3S_1)}, \quad (4.63)$$

where

$$\bar{\chi}_b \equiv \frac{1}{9}(5\chi_{b2} + 3\chi_{b1} + \chi_{b0}) \quad (4.64)$$

is the spin-averaged triplet-P state[7]. Table 4.3 summarises the relevant experimental data

4.5.3 Fixing the Bare Quark Mass

It is not possible to convert simulation energies directly into hadron masses as the heavy quark mass term has been discarded from the Lagrangian. To quote absolute meson masses the energy shift needs to be known. It may be computed by tuning the bare quark mass, M_Q until the kinetic energy of a meson equals its experimental value. The kinetic mass M_{kin} is defined through the non-relativistic dispersion relation

$$aE(\mathbf{p}) = aE(0) + \frac{(a\mathbf{p})^2}{2M_{\text{kin}}} - C_1\frac{((a\mathbf{p})^2)^2}{8M_{\text{kin}}^3} + \dots . \quad (4.65)$$

Practically, one determines M_{kin} by fitting Eq. (4.65) to a set of finite momentum correlators. For a relativistic theory $C_1 = 1$, but in NRQCD one expects deviations from this of $O(v^2)$. To fix the correct bare b-quark mass one adjusts M_b until $m_{\text{kin}}(\Upsilon) = 9.46\ GeV$ within statistical errors.

4.5.4 The NRQCD Scaling Window

Since NRQCD is an effective theory, trying to remove the cut-off will cause the couplings in the Lagrangian to diverge, reflecting the non-renormalisability. Therefore, no continuum extrapolation can be done for Lattice NRQCD. But, of course, the essential idea

[7]For charmonium one would prefer to use the spin-averaged S state, too. In the case of $b\bar{b}$, however, the singlet state, η_b has not yet been observed experimentally.

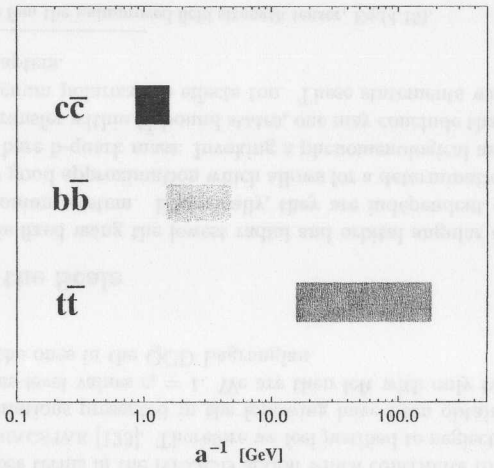

Figure 4.5. *Approximate scaling windows for charmonium, bottomonium and hypothetical toponium. The interval limits come from the estimates in Table 3.1 and thus have to be taken cum grano salis.*

in formulating an effective theory is, that physical results up to a given accuracy can be obtained at fixed cut-off, provided the Lagrangian is carefully calibrated. The range of admissible values of the cut-off, i.e. the range of validity of the effective theory, depends on the specific heavy quark system one is considering. This is indicated in Figure 4.5 for charmonium, bottomonium and hypothetical toponium. Within these intervals the couplings are expected to change only mildly with the cut-off whereas at the right margins they start to blow up and more and more terms would be needed to compensate for the lack of relativistic modes, rendering the theory useless. The left interval limit is set by increasing discretisation errors. We have argued above that a reasonable and practical procedure is to stay with tree-level couplings once the tadpole improvement has been applied. We may argue further that we really measure continuum quantities if this choice is a good approximation in the whole interval of possible cut-offs. In this case there is no need to tune the couplings at all and one would observe that – within reasonable accuracy – results in physical units are independent of the lattice spacing. For charmonium and bottomonium, scaling is expected to show up in the following *windows*

$$c\bar{c} \quad 5.6 \le \beta \le 5.8, \quad (4.66)$$

$$b\bar{b} \quad 5.8 \le \beta \le 6.5, \quad (4.67)$$

where we have simply related lattice spacings to quenched β-values. These numbers imply that our $\beta = 5.6$ dynamical lattices are well suited for bottomonium spectroscopy but too fine to treat the charm quark.

4.6 Summary

In this chapter we have outlined the formulation of non-relativistic QCD suited for numerical simulations on a lattice. We reviewed the discretisation of the next-to-leading order NRQCD Lagrangian which - from naive power counting - is expected to yield both radial and spin splittings with an accuracy below 10%. An advantage of NRQCD is that quark propagators can be obtained from a fully explicit integration scheme allowing for a fast computation. We have discussed in some detail the smearing procedure that involves potential model wave functions. A proper choice is crucial to achieve clean signals for excited states. Finally, we have covered the simplified matching procedure between QCD and NRQCD based on the recipe of tadpole improvement.

◇

Chapter 5

Bottomonium Spectroscopy

In this chapter we present the details of our NRQCD simulation of bottomonium. The investigation of dynamical quark effects will be of primary interest. It is accomplished by a direct comparison of unquenched data with results obtained in the quenched approximation on lattices of similar spacing. From the study of the light hadron spectrum [124] we anticipate that the effect of vacuum polarisation is likely to be small within the range of quark masses considered here, so that high statistical precision seems to be mandatory. Section 5.1 provides detailed information on parameters used in our NRQCD runs. As an illustration of the signal quality obtained for non-relativistic propagators, we give some examples of effective mass plots in Section 5.2. We then turn to a discussion of error analysis which involves the blocking of measurements in Monte Carlo time and the binning of propagators computed from different source points, Section 5.3. Hereafter, results for S- and P-wave mesons are presented including radial excitations as well as spin splittings. With three dynamical quark masses at our disposal we can reliably study the dependence of these states on the light quark mass. In Section 5.5 we determine the lattice scale and give numbers in physical units. Finally, we compute the Υ and η_b kinetic masses from the non-relativistic dispersion relation.

5.1 Simulation Set-Up

Our investigation involves several NRQCD runs whose parameters are listed in Table 5.1. The lattice volume is fixed to $16^3 \times 32$ in all simulations. With a gauge coupling of $\beta = 5.6$ the SESAM lattices realise a physical box of about 1.2-1.4 fm in the spatial direction (depending on the physical quantity used to set the scale) which guarantees negligible finite volume effects on the bottomonium ground state and the first radial and angular momentum excitation. Hence the box size is not a primary issue here and we do not investigate its effect within this study.[1] We use SESAM lattices at three different quark masses corresponding to hopping parameters $\kappa = 0.1560, 0.1570, 0.1575$ and ratios $m_\pi/m_\rho = 0.839(4), 0.755(7), 0.69(1)$. This enables us to calculate the *sea-quark mass dependence* of bottomonium splittings and to perform a 'chiral' extrapolation.
Evidence of an *unquenching effect* can be obtained from a direct comparison of full QCD and quenched simulations at the same lattice spacing. To this end, quenched configurations with $\beta = 6.0$ are generated using the hybrid over-relaxation algorithm [126, 127]. Over-relaxation steps are randomly mixed with Cabibbo-Marinari pseudo-heatbath steps where the latter have a probability of 1/5 [128, 129]. The lattices are thermalised with 2000 sweeps and we perform measurements on configurations separated by 250 sweeps.[2]
The study of dynamical quark effects in the quarkonium spectrum and the dependence of

[1] Higher $b\bar{b}$ excitations have larger extensions and certainly will feel the boundary. An analysis of finite volume effects therefore will be valuable to judge how the 3S and 2P states are affected by the box size.

n_f	β	κ	M_b	TR	action	n	$n^S_{\rm conf}/n^P_{\rm conf}$	$n^S_{\rm sp}/n^P_{\rm sp}$
2	5.6	0.1560	1.7	u_0^L	$O(m_b v^6)$	2	206/206	4/4
2	5.6	0.1570	1.7	u_0^L	$O(m_b v^6)$	2	192/192	13/8
2	5.6	0.1575	1.6	u_0^L	$O(m_b v^6)$	2	203/203	4/0
2	5.6	0.1575	1.7	u_0^L	$O(m_b v^6)$	2	203/203	12/12
2	5.6	0.1575	1.7	u_0^L	$O(m_b v^6)$	3	203/0	4/0
2	5.6	0.1575	1.7	u_0^L	$O(m_b v^6)$	5	203/0	4/0
2	5.6	0.1575	1.8	u_0^L	$O(m_b v^6)$	2	203/0	4/0
2	5.6	0.1575	1.9	u_0^L	$O(m_b v^6)$	2	203/0	4/0
2	5.6	0.1575	2.0	u_0^L	$O(m_b v^6)$	2	203/0	4/0
0	6.0		1.7	u_0^L	$O(m_b v^6)$	2	811/520	4/4
0	6.0		1.7	u_0^L	$O(m_b v^4)$	2	150/0	4/0
0	6.0		1.7	u_0^P	$O(m_b v^4)$	2	350/150	4/4

Table 5.1. *NRQCD run parameters. We separately quote sample size and number of source points for S- and P-state measurements. TR denotes the tadpole renormalisation scheme and n is the stabilisation parameter appearing in the propagator evolution equation.*

spectral quantities on the sea-quark mass are the main objectives for the present investigation. Therefore we have accumulated large statistics - several thousand measurements of $L = 0$ and $L = 1$ states for each sample - using the $O(m_b v^6)$ action in the Landau mean-link tadpole scheme with a fixed bare heavy quark mass, $M_b = 1.7$. The latter value of the b-quark mass was found to yield the correct kinetic Υ mass in a quenched calculation by DAVIES ET.AL.[47]. We will demonstrate in Section 5.6 that it is also adequate for the unquenched samples, so that a costly tuning is avoided.

The dependence on the bare b-quark mass, M_b, is investigated in a series of smaller runs at fixed $\kappa = 0.1575$ with restriction to S states only. The bare mass parameter is varied in the range $1.6 \leq M_b \leq 2.0$. To estimate the relevance of relativistic corrections, we repeat the quenched simulation with fewer measurements applying the NRQCD action of order $m_b v^4$. Additional runs are performed with the plaquette tadpole prescription and with different choices of the stabilisation parameter, n that appears in the evolution equation. The parameters of these investigations of systematic errors are also included in Table 5.1, although their discussion is postponed until Chapter 6.

All simulations involve gauge fields that have been fixed to Coulomb gauge, as mentioned in the previous chapter.

Due to the fact that low-lying $b\bar{b}$ bound states have a tiny spatial extent, one may exploit gauge configurations more than once by starting the quark propagator evolution at different source points separated in space and time. Note, that we do not use a multi-source, but evolve each starting point separately. Simultaneous evolution of different spatial origins by using Z(2) noise has also proven to work, though with somewhat larger errors on radially excited levels [51]. In the quenched runs we restrict ourselves to 4 source

The TχL simulation at $\kappa = 0.1575$ [125, 55] yields the possibility for such an investigation.

[2]We thank G. Bali for providing the SU(3) program.

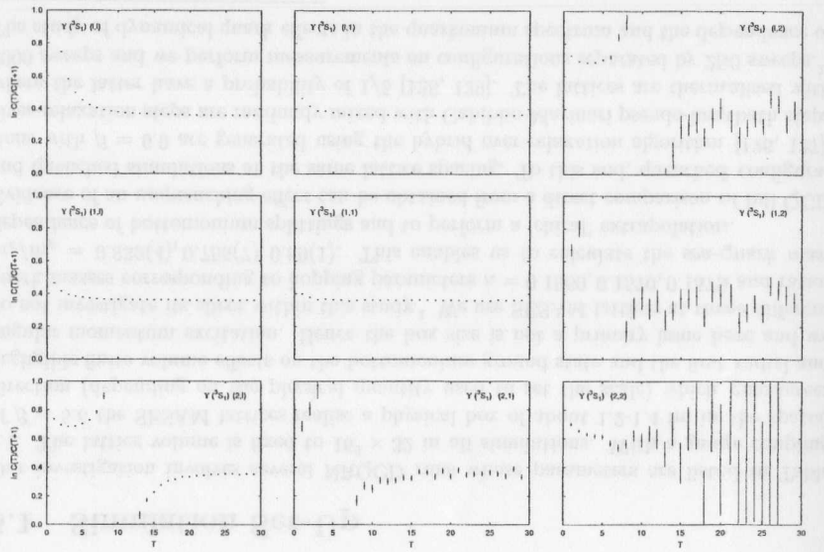

Figure 5.1. *$^3S_1$ effective masses from correlators with smearing combinations $sc/sk = l, 1, 2$ involving 2496 measurements on the sample at $\kappa = 0.1570$.*

points located at $\{(1,1,1,1),(1,1,1,17),(9,9,9,1),(9,9,9,17)\}$ as new configurations can be generated with comparatively little effort. About three times as many origins are used for $n_f = 2$ lattices. Below we give evidence that using many sources really does improve statistics. For the Υ and η_b we calculate a 4×4 matrix of correlators with four different smearings at source and sink, $sc/sk = l, 1, 2, 3$, corresponding to a point source (l), the ground state (1), the first (2) and second (3) excited states, respectively. For the $L = 1$ states we restrict ourselves to the ground state and the first excitation as signals deteriorate. Correlators with momenta up to $|\mathbf{p}| = 2$ are also calculated.

5.2 Signal Quality

To illustrate the quality of our data we display in Figures 5.1 and 5.2 effective masses, defined by $M_{\rm eff} = \ln(C(T)/C(T+1))$, for the triplet-S and singlet-P state arranged as a 3×3 matrix according to the nine smearing combinations with sc/sk = 1,1,2. We always average over all possible polarisations. $C(T)$ denotes the meson correlator at time $T \equiv t/a$. Note that smeared-local $^3S_1$ correlators rise sharply for $(sc, sk) = (2, l), (3, l)$ indicating the sudden decay of the dominant excited state to the ground state. The change in sign is caused by negative values of the correlation function that may occur for hadron operators with mixed smearing. Although we have not tuned the smearing functions, we generally find good plateaus for ground and excited states. For $L = 0$ the radially excited

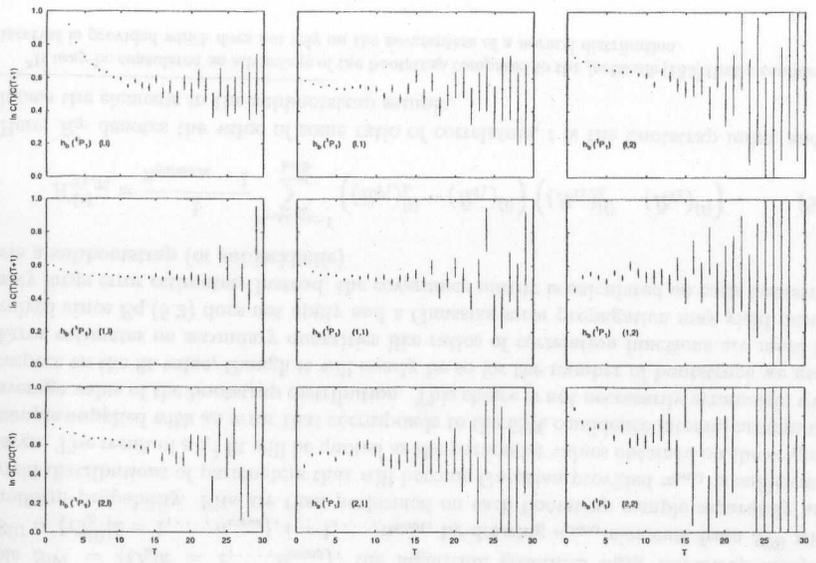

Figure 5.2. 1^1P_1 *effective masses from correlators with smearing combinations* $sc/sk = l, 1, 2$ *involving 2436 measurements on the sample at* $\kappa = 0.1575$.

correlators remain in the first and second excitation for about ten time steps which is apparent from Figures 5.3 and 5.4. Signal/noise stays constant for $^3S_1$ and $^1S_0$ ground states whereas it decays exponentially in time for excited states with a rate determined by the excitation energy [130]. P-state signals are much noisier and vanish from time slice 15 to 20 onwards.

5.3 Data Analysis

The standard way to obtain masses and amplitudes of a hadron correlation function is to fit the measured data to a suitable exponential ansatz invoking the spectral representation Eq.(2.10). We employ two different fitting procedures: The first is a simultaneous fit of many hadron correlators to a multi-exponential function. The second involves the ratio of hadron correlators and fits it to a single exponential. These methods will be discussed in detail below. In either case the maximum likelihood estimate of the model function $C^{\text{model}}(A_i, E_i)$ which depends on a set of amplitudes, A_i and energies, E_i is obtained by minimising

$$\chi^2_C = \sum_{s_1,s_2=1}^{n_{\text{corr}}} \sum_{T_1,T_2=T_{\text{min}}}^{T_{\text{max}}} \left(C - C^{\text{model}}\right)_{s_1T_1} K^{-1}_{s_1T_1,s_2T_2} \left(C - C^{\text{model}}\right)_{s_2T_2} . \qquad (5.1)$$

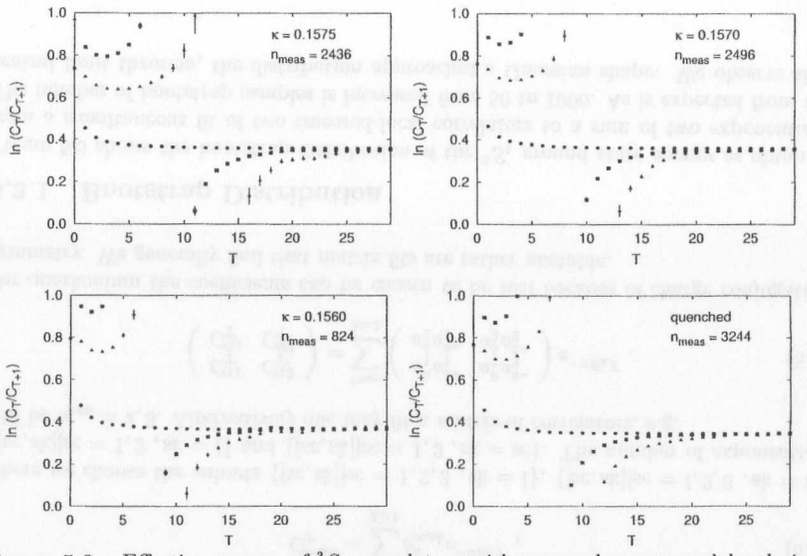

Figure 5.3. *Effective masses of* $^3S_1$ *correlators with smeared source and local sink. Circles, triangles and squares correspond to (1,l), (2,l) and (3,l) respectively.*

Indices T_1, T_2 label time slices, whereas indices s_1, s_2 denote different radial channels. The covariance matrix, K accounts for correlations between data on different time slices obtained from the same sample of gauge configurations. The sample itself is used to determine the covariance matrix for quantities that are directly measured on single configurations like hadron correlation functions:

$$K_{s_1T_1,s_2T_2} = \frac{1}{n_{\text{meas}}\left(n_{\text{meas}}-1\right)} \sum_{k=0}^{n_{\text{meas}}-1} \left(C^k_{s_1T_1} - \bar{C}_{s_1T_1}\right)\left(C^k_{s_2T_2} - \bar{C}_{s_2T_2}\right) , \qquad (5.2)$$

where $\bar{C}_{sT}$ is the sample average

$$\bar{C}_{sT} = \frac{1}{n_{\text{meas}}} \sum_{k=0}^{n_{\text{meas}}-1} C^k_{sT} . \qquad (5.3)$$

The inverse in Eq.(5.1) is computed by singular value decomposition and the minimisation is done using the Levenberg-Marquardt algorithm [131]. In practice, our samples are large enough to fulfil $n_{\text{meas}} \gg 10\ (n_{\text{corrs}}\, n_T{+}1)$ with n_T being the fit range. Therefore the inverse of the covariance matrix generally will exist and χ^2_C as given in Eq.(5.1) provides a reliable goodness-of-fit estimator [132, 133].
Statistical errors on fit parameters are computed by the *bootstrap method* [134] which may be outlined as follows:

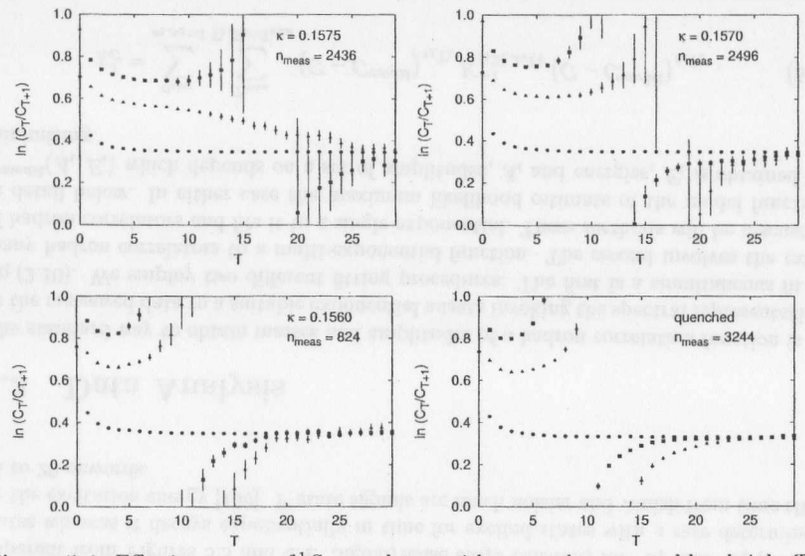

Figure 5.4. *Effective masses of* $^1S_0$ *correlators with smeared source and local sink. The labeling is that of Figure 5.3.*

Consider a quantity O, e.g. a meson correlation function on a specified time slice, that has been measured on a number of gauge configurations. From the original sample $S^{(0)} = \{O_k | k = 1, \ldots, n_{\text{meas}}\}$, the algorithm generates n_{boot} bootstrap samples $S^{(i)} = \{O_k^{(i)} | k = 1, \ldots, n_{\text{meas}}\}, i = 1, \ldots, n_{\text{boot}}$, by drawing n_{meas} elements from $S^{(0)}$ with uniform probability. Fits are then performed on each bootstrap sample separately and yield distributions of parameters that will become Gaussian provided n_{boot} is sufficiently large. The result of a χ^2 fit will be quoted as the parameter values obtained on the original sample supplied with an error that corresponds to the 68% confidence interval around the average value of the bootstrap distribution. This choice is not necessarily symmetric with respect to the fit value, though it will nearly be so for the number of bootstraps we use.[3] Error estimates on secondary quantities like ratios of correlation functions are more involved since Eq.(5.2) does not apply and a Gaussian error propagation may yield unreliably large error estimates. Instead, the covariance matrix is calculated on each bootstrap via a subbootstrap (or subjackknife)

$$K^{(i)}_{T_1,T_2} = \frac{1}{n_{\text{subboot}} - 1} \sum_{k=0}^{n_{\text{subboot}}-1} \left((R_{T_1})^{(i)}_k - (\bar{R}_{T_1})^{(i)} \right) \left((R_{T_2})^{(i)}_k - (\bar{R}_{T_2})^{(i)} \right) . \qquad (5.4)$$

Here, R_T denotes the value of some ratio of correlators, i is the bootstrap index and k labels the elements in the subbootstrap sample.

[3] It may be considered an advantage of the bootstrap compared to the *jackknife* [135] that a confidence interval is provided which does not rely on the assumption of a normal distribution.

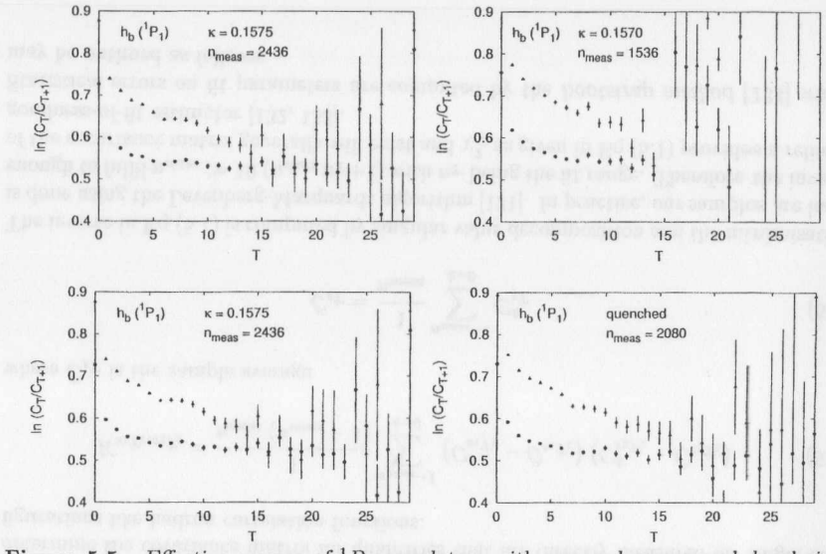

Figure 5.5. *Effective masses of* $^1P_1$ *correlators with smeared source and local sink. Circles correspond to (1,l), triangles to (2,l).*

Following [47], we make use of *vector fits* to extract spectroscopic quantities from meson correlators. A vector of correlators is simultaneously fitted to a sum of exponentials,

$$C_T^{\text{sc,sk}} = \sum_{k=1}^{n_{\text{exp}}} b^k_{\text{sc,sk}} \mathrm{e}^{-aE_k T} , \qquad (5.5)$$

where we choose the subsets $\{[\text{sc}, \text{sk}] | \text{sc} = 1, 2, 3\ , \text{sk} = l\}$, $\{[\text{sc}, \text{sk}] | \text{sc} = l, 2, 3\ , \text{sk} = l\}$, $\{[\text{sc}, \text{sk}] | \text{sc} = 1, 2\ , \text{sk} = l\}$ and $\{[\text{sc}, \text{sk}] | \text{sc} = 1, 2\ , \text{sk} = \text{sc}\}$. The number of exponentials will be $n_{\text{exp}} = 2, 3$. Alternatively one may fit a *matrix* of correlators, e.g.

$$\begin{pmatrix} C_T^{11} & C_T^{12} \\ C_T^{21} & C_T^{22} \end{pmatrix} = \sum_{k=1}^{n_{\text{exp}}} \begin{pmatrix} a_1^k a_1^{k*} & a_1^k a_2^{k*} \\ a_2^k a_1^{k*} & a_2^k a_2^{k*} \end{pmatrix} \mathrm{e}^{-aE_k T} . \qquad (5.6)$$

For quarkonium the coefficients can be chosen to be real because of charge conjugation symmetry. We generally find that matrix fits are rather unstable.

5.3.1 Bootstrap Distribution

Figure 5.6 shows the bootstrap distribution of the $^3S_1$ ground state energy as obtained from a simultaneous fit of two smeared-local correlators to a sum of two exponentials. The number of bootstrap samples is increased from 50 to 1000. As is expected from the central limit theorem, the distribution approaches a Gaussian shape. We observe that

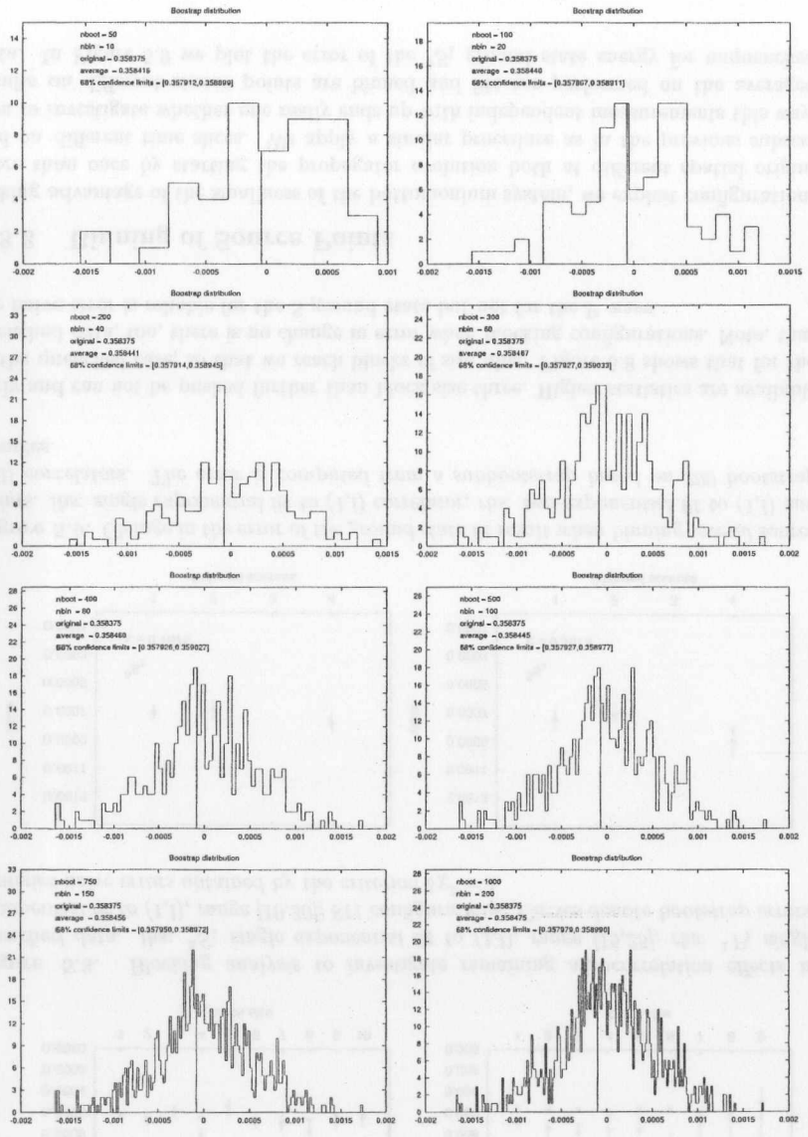

Figure 5.6. *Bootstrap distribution of the fit parameter aE_1 relative to the average value. The data is taken from a $^3S_1$ two-exponential fit to (1,1) and (2,1) correlators using the configurations with $\kappa = 0.1575$. The bootstrap sample size is varied from 50 to 1000. The line indicates the fit value on the original sample.*

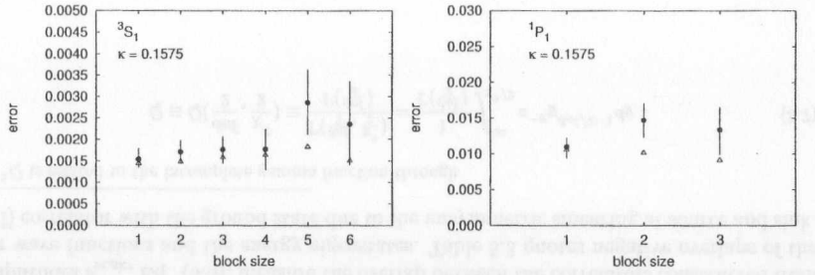

Figure 5.7. *Blocking analysis to investigate remaining autocorrelation effects: $\kappa = 0.1575$, 203 configurations; lhs: $^3S_1$ single exponential fit to (1,1), range [20,30], rhs: $^1P_1$ single exponential fit to (1,1), range [10,30]. Circles denote bootstrap errors, triangles naive errors obtained by the criterion $\delta\chi^2 = 1$. Errors are estimated from a subbootstrap sample of size 200.*

the error is perfectly stable for $n_{\text{boot}} > 200$. Hence, we find it reasonable to choose a bootstrap ensemble of 300 samples throughout the analysis.

5.3.2 Blocking in MC Time

The results of the autocorrelation analysis of the HMC time series [58] have been summarised in Chapter 2. We were led to the conclusion that a MC time separation of about 25 trajectories between subsequent measurements would be adequate for hadronic observables. A simple way to estimate the correlation within the Markov chain is a standard blocking procedure. This is less involved than the direct computation of integrated autocorrelation times and is applicable with smaller statistics. Gauge field configurations are chronologically ordered and the data is binned into blocks of successive measurements. Fits are then performed on the blocked data. We restrict ourselves to single exponential fits, as two-exponential fits become unstable with increasing block size [4]. In Figure 5.7 we plot the error of the fit result for the ground state energy as a function of block size for both the triplet-S and singlet-P states. The data has been taken from the $\kappa = 0.1575$ sample and the source point for propagator evolution was $(1, 1, 1, 1)$. The error of the error is estimated from a subbootstrap within each bootstrap. We find no variation in the fit error although the block size is varied significantly. This confirms the result of a similar analysis in the light sector which applies the analogue jackknife procedure [124] and indicates that the dynamical configurations are indeed decorrelated with respect to hadronic observables. The comparison of the bootstrap error with the naive error obtained from a single fit by the criterion $\delta\chi^2 = 1$ reveals that the latter generally underestimates the true error. However, this difference is not much pronounced for the one-exponential fits considered here. The limited number of configurations in the unquenched case prevents going to large block sizes. In particular, the fit to the P state becomes unstable rather

[4] We include measurements for one source point only.

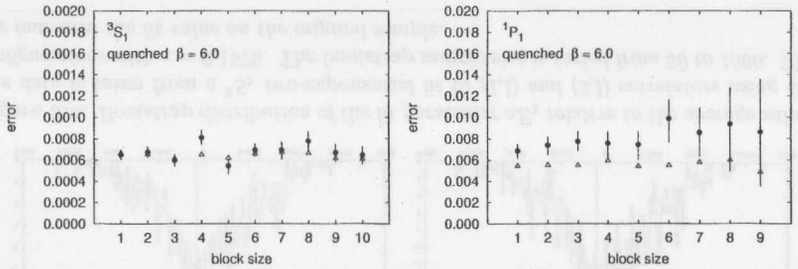

Figure 5.8. *Blocking analysis to investigate remaining autocorrelation effects in quenched data. lhs: $^3S_1$ single exponential fit to (1,l), range [15,25], rhs: $^1P_1$ single exponential fit to (1,l), range [10,30]; 811 configurations. Circles denote bootstrap errors, triangles naive errors obtained by the criterion $\delta\chi^2 = 1$.*

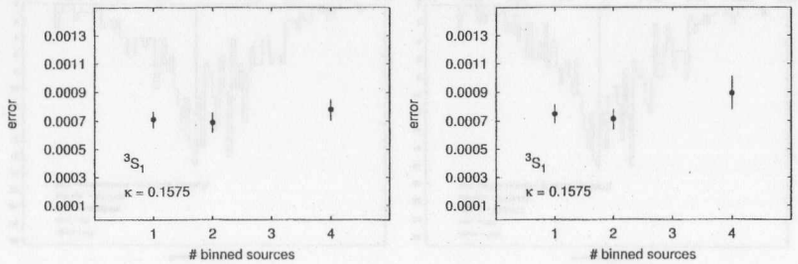

Figure 5.9. *Change in the error of the ground state fit result when binning several source points. lhs: single exponential fit to (1,l) correlator; rhs: two-exponential fit to (1,l) and (2,l) correlators. The error is computed from a subbootstrap based on 200 bootstrap samples.*

early and can not be pushed further than block size three. Higher statistics are available in the quenched case, so that we reach blocks of size nine. Figure 5.8 shows that for the quenched data, too, there is no change in error when blocking configurations. Note, that the naive error is reliable for the S ground state but not for the P wave.

5.3.3 Binning of Source Points

Taking advantage of the smallness of the bottomonium system, we exploit configurations more than once by starting the propagator evolution both at different spatial origins and on different time slices. We apply a similar procedure as in the previous subsection to investigate whether one really ends up with independent measurements this way: results on different source points are binned and fits are performed on the averaged data. In Figure 5.9 we plot the error of the $^3S_1$ ground state energy for unquenched

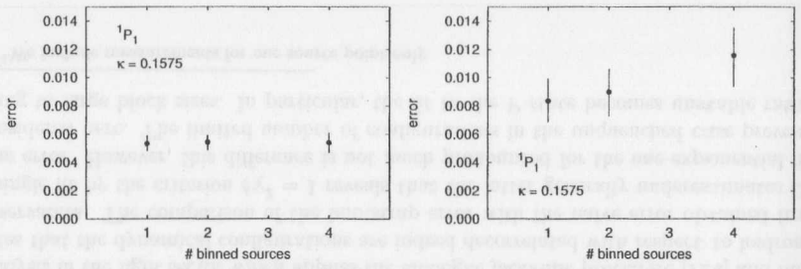

Figure 5.10. *Same as Figure 5.9 for the $^1P_1$ correlator.*

($\kappa = 0.1575$) data comparing single exponential and two-exponential fits. We include four sources, $\{(1,1,1,1),(9,9,9,1),(1,1,1,17),(9,9,9,17)\}$ and either average over all of these (# binned sources = 4), split them in two sets, or do not average at all. We do not observe a significant change of the fit error on the number of binned sources, indicating that measurements are indeed independent. The same conclusion can be drawn in the case of P waves as shown in Figure 5.10. Practically, our fits turn out to be very stable even when binning all available sources. This is the case for results presented in the following.

5.4 Simulation Results

5.4.1 Radial and Orbital Angular Momentum Excitations

We use the multi-exponential fit ansatz to extract the ground state as well as radial excitations and orbital angular momentum levels. Keeping a fixed upper limit of the fit interval, $T_{\max}$, the lower limit is varied and the goodness of fit is monitored by the Q value, i.e. the probability that fluctuations in adequately modelled data will generate a χ^2 greater than that of the fit.[5] Our decision on final results is based on the requirements of stability and a reasonable value of Q which is as usual desired to be larger than 0.1. Notice from Table 5.2, that two-exponential fits to S-state correlators are perfectly stable for a very large range of $T_{\min}$. The Q value increases sharply until it reaches a plateau. Smaller values of the goodness of fit such as for $^1P_1$ do not necessarily rule out a fit, since the χ^2/dof is still reasonable and here, too, results are fairly stable, Table 5.4. The amplitudes $b^k_{\mathrm{sc,sk}}$, Eq. (5.5), measure the overlap between the correlators constructed from our wave functions and the energy eigenstates. Table 5.3 quotes negative overlaps of the (2,l) correlator with the ground state due to the unsymmetric smearing at source and sink.

[5] Q is related to the incomplete gamma function through

$$Q \equiv Q(\frac{\mathrm{dof}}{2}, \frac{\chi^2}{2}) \equiv \frac{\Gamma(\frac{\mathrm{dof}}{2}, \frac{\chi^2}{2})}{\Gamma(\frac{\mathrm{dof}}{2})} = \frac{1}{\Gamma(\frac{\mathrm{dof}}{2})} \int_{\chi^2/2}^{\infty} \mathrm{e}^{-y} y^{\mathrm{dof}/2-1} dy \,. \tag{5.7}$$

n_{exp}	T_{min}	T_{max}	aE_1	aE_2	aE_3	χ^2/dof	Q
2	2	30	$0.3605^{+0.0010}_{-0.0010}$	$0.6439^{+0.0049}_{-0.0055}$		450.8/52	0.000
(1,1),(2,1)	4	30	$0.3585^{+0.0006}_{-0.0006}$	$0.6116^{+0.0035}_{-0.0035}$		74.4/48	0.009
	6	30	$0.3585^{+0.0006}_{-0.0006}$	$0.5986^{+0.0047}_{-0.0049}$		42.0/44	0.559
	8	30	$0.3584^{+0.0006}_{-0.0006}$	$0.5965^{+0.0075}_{-0.0070}$		36.9/40	0.609
	10	30	$0.3584^{+0.0006}_{-0.0005}$	$0.5944^{+0.0099}_{-0.0098}$		30.0/36	0.749
	12	30	$0.3584^{+0.0006}_{-0.0005}$	$0.5930^{+0.0148}_{-0.0154}$		27.6/32	0.687
	14	30	$0.3584^{+0.0006}_{-0.0006}$	$0.5969^{+0.0269}_{-0.0277}$		27.2/28	0.507
3	6	25	$0.3587^{+0.0006}_{-0.0006}$	$0.5958^{+0.0071}_{-0.0063}$	$1.49^{+0.30}_{-0.41}$	30.1/31	0.515
(1,1),(2,1)	7	25	$0.3586^{+0.0006}_{-0.0007}$	$0.5950^{+0.0090}_{-0.0092}$	$1.42^{+0.23}_{-0.46}$	30.0/29	0.413
	8	25	$0.3588^{+0.0007}_{-0.0007}$	$0.5869^{+0.0130}_{-0.0127}$	$1.07^{+0.16}_{-0.23}$	25.6/27	0.541
	10	25	$0.3588^{+0.0007}_{-0.0008}$	$0.5868^{+0.0180}_{-0.0197}$	$1.00^{+0.22}_{-0.14}$	23.4/23	0.437
3	4	25	$0.3617^{+0.0011}_{-0.0010}$	$0.6059^{+0.0059}_{-0.0056}$	$0.8561^{+0.0195}_{-0.0195}$	308.3/54	0.000
(1,1),(2,1)	5	25	$0.3600^{+0.0009}_{-0.0009}$	$0.5958^{+0.0047}_{-0.0051}$	$0.7877^{+0.0182}_{-0.0178}$	118.1/51	0.000
(3,1)	6	25	$0.3597^{+0.0008}_{-0.0008}$	$0.5942^{+0.0050}_{-0.0050}$	$0.7597^{+0.0215}_{-0.0218}$	52.0/48	0.321
	7	25	$0.3594^{+0.0008}_{-0.0008}$	$0.5930^{+0.0059}_{-0.0056}$	$0.7719^{+0.0359}_{-0.0386}$	48.4/45	0.336
	8	25	$0.3594^{+0.0008}_{-0.0008}$	$0.5953^{+0.0080}_{-0.0071}$	$0.8276^{+0.0616}_{-0.0678}$	45.9/42	0.315
	9	25	$0.3591^{+0.0009}_{-0.0009}$	$0.5894^{+0.0084}_{-0.0087}$	$0.7346^{+0.0743}_{-0.0793}$	39.6/39	0.444

Table 5.2. *Examples of simultaneous multi-exponential fits to smeared-local and local-local $^3S_1$ correlators. The data belongs to $\kappa = 0.1575$ and is based on a total of $12 \times 203 = 2436$ measurements.*

The relative magnitude of non-diagonal to diagonal amplitudes indicates that smearing functions are well chosen.

Results for radial and orbital splittings that are used in further analysis are taken from two-exponential fits to (1,1) and (2,1) correlators. These have the cleanest signals and exhibit very stable fits. The complete results for each hopping parameter and the quenched simulation are contained in Table 5.5. In addition, Figures 5.11-5.13 present the fitted values as a function of T_{min}, together with the selected final number. Note that our choice does not correspond to the smallest T_{min} with acceptable χ^2, but to a value which is well inside the plateau and thus carries somewhat larger errors. These errors then cover the systematic uncertainty from varying the fit interval.

A drawback of using smeared-local correlators is the potential danger of overestimating energy levels, since they usually approximate the asymptotic value from above. It has been observed that the radial 2S-1S splittings are particularly sensitive to such a shift [136]. We therefore repeat the analysis using two-exponential fits to (1,1) and (2,2) correlators. Sink smearing produces noisier signals but does not necessarily induce larger errors on the fitted parameters as a consequence of a better decorrelation of the data. This is reflected by the smeared-smeared results included into Table 5.5: ground state energies carry similar errors as the corresponding smeared-local numbers. The excited state, however, comes with significantly larger errors. A careful inspection of these results reveals that the smeared-smeared and smeared-local data are consistent. The worst case is a shift by one standard deviation.

We have also applied vector fits involving two correlators but three exponentials. The third exponential accounts for contamination from higher radial excitations and provides

n_{exp}	T_{min}	T_{max}	k	$b_{1,k}$	$b_{2,k}$
2	2	30	1	$0.5330^{+0.0064}_{-0.0063}$	$-0.0042^{+0.0057}_{-0.0057}$
(1,1),(2,1)			2	$0.1658^{+0.0099}_{-0.0098}$	$0.6942^{+0.0050}_{-0.0052}$
	4	30	1	$0.5249^{+0.0046}_{-0.0051}$	$-0.0189^{+0.0033}_{-0.0031}$
			2	$0.1370^{+0.0080}_{-0.0088}$	$0.6463^{+0.0055}_{-0.0053}$
	6	30	1	$0.5243^{+0.0049}_{-0.0048}$	$-0.0231^{+0.0032}_{-0.0029}$
			2	$0.1257^{+0.0114}_{-0.0107}$	$0.6171^{+0.0092}_{-0.0096}$
	8	30	1	$0.5213^{+0.0046}_{-0.0054}$	$-0.0226^{+0.0037}_{-0.0031}$
			2	$0.1412^{+0.0209}_{-0.0206}$	$0.6068^{+0.0210}_{-0.0197}$
	10	30	1	$0.5223^{+0.0053}_{-0.0056}$	$-0.0235^{+0.0034}_{-0.0030}$
			2	$0.1412^{+0.0274}_{-0.0302}$	$0.6029^{+0.0381}_{-0.0391}$
	12	30	1	$0.5232^{+0.0055}_{-0.0054}$	$-0.0240^{+0.0034}_{-0.0033}$
			2	$0.1233^{+0.0330}_{-0.0349}$	$0.5993^{+0.0882}_{-0.0856}$
	14	30	1	$0.5235^{+0.0062}_{-0.0065}$	$-0.0239^{+0.0033}_{-0.0037}$
			2	$0.1280^{+0.0715}_{-0.0665}$	$0.6296^{+0.1926}_{-0.1906}$

Table 5.3. *Amplitudes for $^3S_1$ two-exponential fits to (1,1) and (2,1) correlators.*

n_{exp}	T_{min}	T_{max}	aE_1	aE_2	aE_3	χ^2/dof	Q
	4	30	$0.5409^{+0.0037}_{-0.0036}$	$0.7215^{+0.0074}_{-0.0077}$		232.0/48	0.000
	5	30	$0.5304^{+0.0043}_{-0.0045}$	$0.7209^{+0.0105}_{-0.0103}$		71.7/46	0.009
	6	30	$0.5299^{+0.0047}_{-0.0046}$	$0.7172^{+0.0130}_{-0.0137}$		71.2/44	0.006
	7	30	$0.5273^{+0.0063}_{-0.0055}$	$0.7295^{+0.0192}_{-0.0183}$		68.3/42	0.006
	8	30	$0.5244^{+0.0052}_{-0.0057}$	$0.7475^{+0.0286}_{-0.0296}$		64.7/40	0.008

Table 5.4. *Simultaneous two-exponential fits to two smeared-local $^1P_1$ correlators.*

a more reliable 2S state. Examples of such fits have been added to Table 5.2. We have not encountered any discrepancies with the two-exponential results: ground state and first excited state energies generally agree within errors. These fits also provide an estimate of the second excited state which, however, is not reliable since no correlator with a good overlap with 3S has been used. Including the (3,1) turns out to be difficult. We have not succeeded in obtaining fit results that are stable on more than three subsequent $T_{\min}$ values using (1,1),(2,1) and (3,1) correlators at the same time. The situation is significantly improved if we exchange (1,1) for the local-local correlator. Three-exponential fits to this set perform much better, see once more Table 5.2. Again we observe complete agreement of the result for 2S with previous fits, whereas now a more reliable estimate of the second excitation is achieved. Notice also, that the ground state comes out slightly higher as a consequence of replacing the (1,1) correlator. Results of three-exponential fits for all κ-values and the quenched approximation are collected in Table 5.6. Clearly, 3S states extracted this way have to be treated with care: The fitting uncertainty is more severe and a fourth exponential is not taken into account. In addition the potential model wave functions point at sizable finite-volume effects for the second radial excitation on a 1.4 fm lattice.

We have already mentioned that matrix fits have not been sufficiently stable, so we do not quote any results here.

For illustration of the quality of the two-exponential fits we plot in Figure 5.14 the effective amplitude $\mathrm{e}^{aE_1T}C_T$ together with the lowest-order functional form

$$\mathrm{e}^{aE_1T} \cdot C_T = A_1 + A_2 \mathrm{e}^{-a(E_2-E_1)T}\,, \tag{5.8}$$

with parameters taken from the fit.

We summarise the final results for radial and orbital angular momentum energy levels in Table 5.7.

5.4.2 Extrapolation in the Sea-Quark Mass

Grinstein and Rothstein [137] have calculated the pion mass dependence of radial and orbital splittings in quarkonia up to order m_π^4 from a chiral Lagrangian. In lowest order they find a linear dependence on the quark mass, which may be parametrised as (see Ref. [138])

$$a\Delta E = a\Delta E_0 + \text{constant} \cdot \sum_{u,d,s} \frac{am_q}{ap_\Upsilon} + \dots\,. \tag{5.9}$$

Inside an Υ the typical momentum transfer, p_Υ is between 0.5 and 1 GeV, i.e. $m_l, m_s \ll p_\Upsilon < m_c$. This indicates that the physically relevant number of dynamical quark flavours is $n_f^{\text{phys}} = 3$. The effect of heavy quark vacuum polarisation is thus likely to be negligible. Assuming this, we have restricted the flavour sum in (5.9) to the light quarks only. The second important issue concerns the value of m_q to which energy splittings are to be extrapolated. Phenomenologically, one expects little variation as a function of dynamical quark mass and, since all light quarks are substantially smaller than p_Υ, it has been

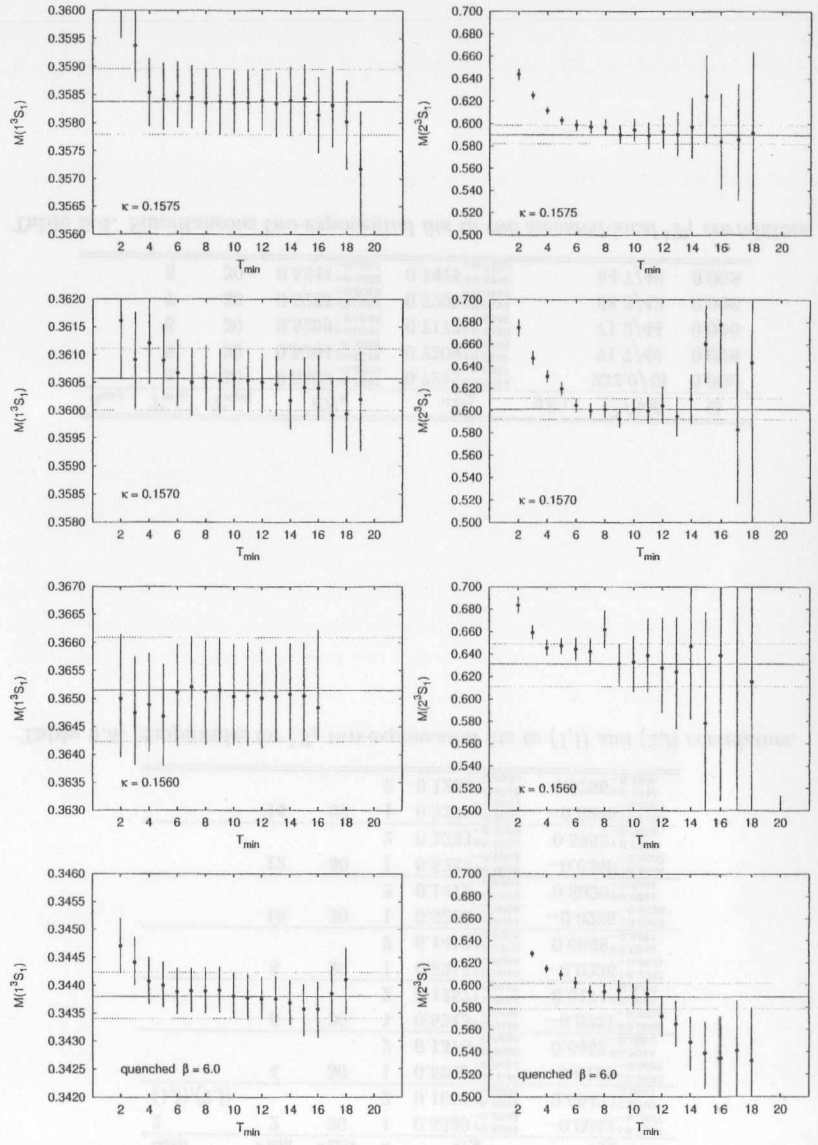

Figure 5.11. *Fitted $^3S_1$ ground state (left column) and first radial excitation (right column) as a function of the lower limit of the fit range, $T_{\min}$. We applied a two-exponential fit involving correlators (1,1) and (2,1). The upper limit of the fit range is fixed to $T_{\max} = 30$ for $\kappa = 0.1575, 0.1570$ and $T_{\max} = 31$ for $\kappa = 0.1560$ and the quenched sample. Note that the excited state in the quenched background drops to the ground state very early restricting the plateau to four or five points and indicating that smearing is less efficient in this case.*

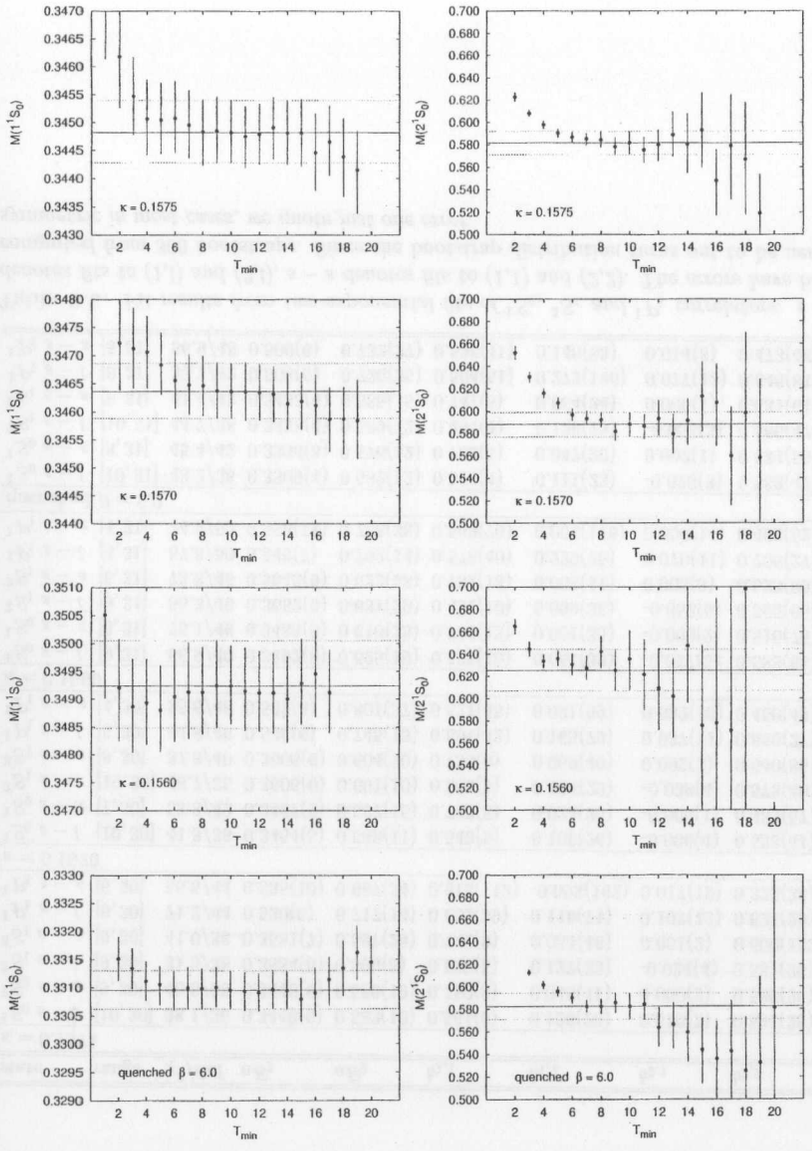

Figure 5.12. *Same as Figure 5.11 for singlet-S correlator. The data looks very similar to the previous plot as a consequence of the strong correlation between* $^1S_0$ *and* $^3S_1$.

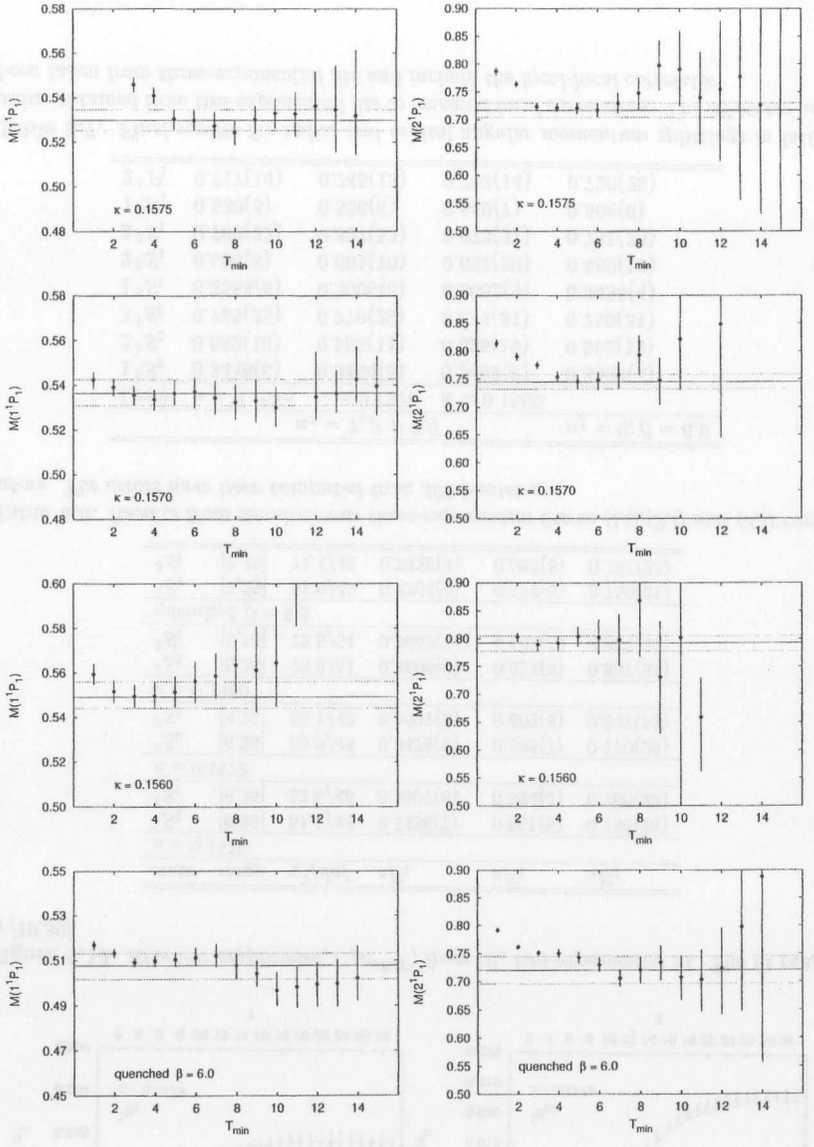

Figure 5.13. *Same as Fig. 5.11 for singlet-P correlator. P state signals rapidly vanish into noise. Note the change in scale compared to Figures 5.11 and 5.12.*

state	range	χ^2/dof	aE_1	aE_2	$b_{1,1}$	$b_{1,2}$	$b_{2,1}$	$b_{2,2}$
$\kappa = 0.1575$								
$^1S_0$ $s-l$	[10,30]	38.1/36	0.3448(6)	0.582(10)	0.564(6)	0.126(28)	0.010(3)	0.591(38)
$^1S_0$ $s-s$	[9,30]	40.8/38	0.3446(6)	0.586(19)	0.750(8)	0.048(41)	0.000(2)	0.586(98)
$^3S_1$ $s-l$	[9,30]	31.9/38	0.3584(6)	0.590(8)	0.522(5)	0.127(23)	-0.024(4)	0.581(26)
$^3S_1$ $s-s$	[9,30]	41.0/38	0.3581(7)	0.597(24)	0.742(9)	0.054(46)	0.001(2)	0.600(123)
$^1P_1$ $s-l$	[6,30]	71.2/44	0.530(5)	0.717(14)	0.652(39)	0.119(71)	0.107(13)	0.621(29)
$^1P_1$ $s-s$	[6,30]	56.5/44	0.535(10)	0.687(34)	0.613(112)	-0.093(162)	0.017(19)	0.323(38)
$\kappa = 0.1570$								
$^1S_0$ $s-l$	[10,30]	41.3/36	0.3464(5)	0.588(11)	0.543(5)	0.106(26)	-0.006(4)	0.553(41)
$^1S_0$ $s-s$	[7,30]	53.8/42	0.3467(6)	0.587(15)	0.747(8)	0.024(26)	-0.000(1)	0.489(57)
$^3S_1$ $s-l$	[10,30]	48.7/36	0.3606(6)	0.601(10)	0.503(5)	0.124(29)	-0.039(4)	0.573(40)
$^3S_1$ $s-s$	[8,30]	37.3/40	0.3606(6)	0.604(20)	0.734(8)	0.069(40)	0.002(2)	0.540(85)
$^1P_1$ $s-l$	[5,30]	44.8/46	0.536(6)	0.745(13)	0.601(42)	0.165(79)	0.087(11)	0.640(27)
$^1P_1$ $s-s$	[4,30]	55.6/48	0.532(8)	0.801(37)	0.521(45)	0.091(99)	0.032(10)	0.450(49)
$\kappa = 0.1560$								
$^1S_0$ $s-l$	[9,31]	66.9/40	0.3492(8)	0.625(19)	0.525(10)	0.061(38)	-0.017(5)	0.588(68)
$^1S_0$ $s-s$	[6,31]	76.1/46	0.3483(8)	0.610(23)	0.736(13)	0.001(35)	-0.000(2)	0.516(75)
$^3S_1$ $s-l$	[9,31]	55.3/40	0.3652(9)	0.631(20)	0.491(10)	0.069(38)	-0.052(6)	0.565(66)
$^3S_1$ $s-s$	[6,31]	73.8/46	0.3643(9)	0.623(28)	0.731(13)	0.008(41)	0.002(3)	0.523(89)
$^1P_1$ $s-l$	[4,31]	57.8/50	0.549(7)	0.792(14)	0.578(40)	0.229(75)	0.070(11)	0.705(27)
$^1P_1$ $s-s$	[4,31]	74.9/50	0.553(11)	0.786(38)	0.562(70)	0.052(146)	0.006(14)	0.463(52)
quenched $\beta = 6.0$								
$^1S_0$ $s-l$	[10,31]	43.2/38	0.3309(4)	0.582(12)	0.516(4)	0.111(23)	-0.028(3)	0.582(47)
$^1S_0$ $s-s$	[8,31]	45.4/42	0.3306(3)	0.576(12)	0.758(5)	0.047(20)	0.002(1)	0.534(55)
$^3S_1$ $s-l$	[10,31]	44.7/38	0.3438(4)	0.589(12)	0.481(4)	0.126(23)	-0.056(3)	0.566(47)
$^3S_1$ $s-s$	[8,31]	41.4/42	0.3433(4)	0.585(15)	0.747(5)	0.064(24)	0.006(1)	0.531(61)
$^1P_1$ $s-l$	[8,31]	33.2/42	0.508(6)	0.720(25)	0.564(51)	0.273(146)	0.077(13)	0.646(81)
$^1P_1$ $s-s$	[5,31]	56.9/48	0.509(6)	0.732(27)	0.538(41)	0.140(83)	0.014(8)	0.473(46)

Table 5.5. *Fit results from two-exponential fits of $^1S_0$, $^3S_1$ and $^1P_1$ correlators. $s-l$ denotes fits to (1,l) and (2,l), $s-s$ denotes fits to (1,1) and (2,2). The errors have been computed from 300 bootstraps. Since the bootstrap distribution turns out to be nearly symmetric in most cases, we quote just one error.*

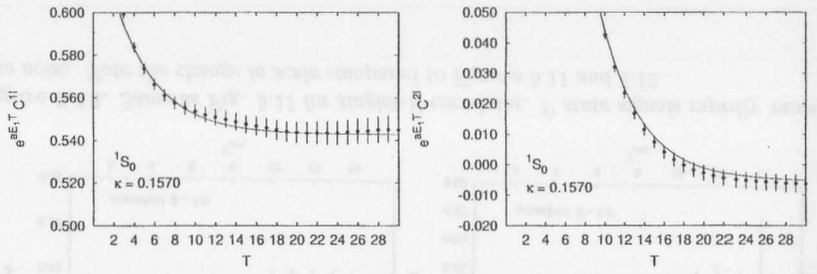

Figure 5.14. *Effective amplitudes, $C_T e^{aE_1 T}$, from $^1S_0$ two-exponential fit. The fit range is [10.30].*

state	range	χ^2/dof	aE_1	aE_2	aE_3
$\kappa = 0.1575$					
$^1S_0$	[6,25]	51.5/48	0.3456(7)	0.581(5)	0.755(25)
$^3S_1$	[6,25]	52.0/48	0.3597(8)	0.594(5)	0.760(22)
$\kappa = 0.1570$					
$^1S_0$	[6,25]	86.9/48	0.3478(6)	0.595(7)	0.770(29)
$^3S_1$	[8,25]	68.1/42	0.3607(8)	0.602(8)	0.827(53)
$\kappa = 0.1560$					
$^1S_0$	[5,25]	73.8/51	0.3500(9)	0.624(8)	0.837(31)
$^3S_1$	[5,25]	72.5/51	0.3662(11)	0.643(8)	0.873(37)
quenched $\beta = 6.0$					
$^1S_0$	[7,25]	51.9/45	0.3304(4)	0.579(5)	0.750(31)
$^3S_1$	[7,25]	71.1/45	0.3436(4)	0.593(5)	0.781(33)

Table 5.6. *Results from simultaneous three-exponential fits to (1,l),(2,l) and (3,l) correlators. The errors have been computed from 300 bootstraps.*

	$n_f = 2, \beta = 5.6$			$n_f = 0, \beta = 6.0$
Level	$\kappa = 0.1575$	$\kappa = 0.1570$	$\kappa = 0.1560$	
$1\,^1S_0$	0.3448(6)	0.3464(5)	0.3492(8)	0.3309(4)
$2\,^1S_0$	0.582(10)	0.588(11)	0.625(19)	0.582(12)
$3\,^1S_0$	0.755(25)	0.770(29)	0.837(31)	0.750(31)
$1\,^3S_1$	0.3584(6)	0.3606(6)	0.3652(9)	0.3438(4)
$2\,^3S_1$	0.590(8)	0.601(10)	0.631(20)	0.589(12)
$3\,^3S_1$	0.760(22)	0.827(53)	0.873(37)	0.781(33)
$1\,^1P_1$	0.530(5)	0.536(6)	0.549(7)	0.508(6)
$2\,^1P_1$	0.717(14)	0.745(13)	0.792(14)	0.720(25)

Table 5.7. *Final results for radial and orbital angular momentum splittings in lattice units, obtained from two-exponential fits to smeared-local correlators. The 3S states have been taken from three-exponential fits and include the local-local correlator.*

κ_c	κ_l	$\kappa_s(K)$	$\kappa_s(K^*)$	$\kappa_s(\Phi)$
0.158507(44)	0.158462(42)	0.15654(11)	0.15561(14)	0.15563(14)

Table 5.8. *Hopping parameter values in the light and strange sector [124].*

argued that the effect of three unequal mass quarks may be adequately reproduced by three degenerate light flavours of average mass [139],

$$m_{\text{eff}} = \frac{1}{3}(m_u + m_d + m_s) \sim \frac{m_s}{3} . \tag{5.10}$$

Hence we choose to extrapolate linearly to am_{eff} according to

$$a\Delta E = a\Delta E_0 + c \cdot am_q . \tag{5.11}$$

A 'chiral limit' at $m_s/3$ and not beyond represents a major advantage of working with the Υ system. Unquenching effects, though probably less important than in light hadrons, can be nailed down more reliably due to the relative insensitivity to the $m_l - m_s$ mass difference.

In this context we point out that there is an uncertainty in the strange quark mass stemming from the fact that we have generated only two (degenerate) dynamical flavours. These are identified with the up and down quarks, so that, effectively, m_s is defined in the two-flavour theory in a 'partially quenched' way only. A consistent approach to analyse this 'partially quenched' data has been presented in Ref.[140, 141], where hadronic correlators with valence quark content both equal to and different from that of the underlying sea quark are considered in order to determine the light quark masses. In Table 5.8 we list the hopping parameter values belonging to the chiral limit, κ_c, the non-strange quark mass, κ_l and the strange quark mass, κ_s obtained from the analysis of the light hadron spectrum [142]. Note the disagreement of κ_s determined using the kaon mass as input with the corresponding value calculated from the K^* or Φ mesons. Here, we choose the average of these, $\bar{\kappa}_s$, corresponding to

$$M_{\text{eff}} = \frac{1}{3}\bar{M}_s = \frac{1}{6}\left(\frac{1}{\bar{\kappa}_s} - \frac{1}{\kappa_c}\right) \sim 0.0159 . \tag{5.12}$$

This is somewhat smaller than our lightest sea-quark mass $M_q(\kappa = 0.1575) \sim 0.0202$. The results of the uncorrelated linear fits are shown in Figure 5.15. Fit parameters are listed in Table 5.9 together with the energy splittings at the effective and the light quark mass. No significant deviation from the linear parameterisation is apparent in the data. We find the difference between $\Delta E(m_s/3)$ and ΔE_0, which may be taken as an upper limit of the uncertainty in m_{eff}, to vary from 4 to 14%. In this context it is illustrative to compare the dependence on the sea-quark mass calculated here with the one found in the light hadron sector. There it is customary to fix the lattice scale through the ρ-meson mass [6]. In Figure 5.16 we compare the quark-mass extrapolations of the bottomonium $1^1P_1 - 1^3S_1$ splitting and the ρ-meson. The slope in the light vector meson mass turns

[6] Obviously, in the full theory the ρ-mass is a poor choice. The nucleon mass should be preferred, though it is subject to larger statistical errors.

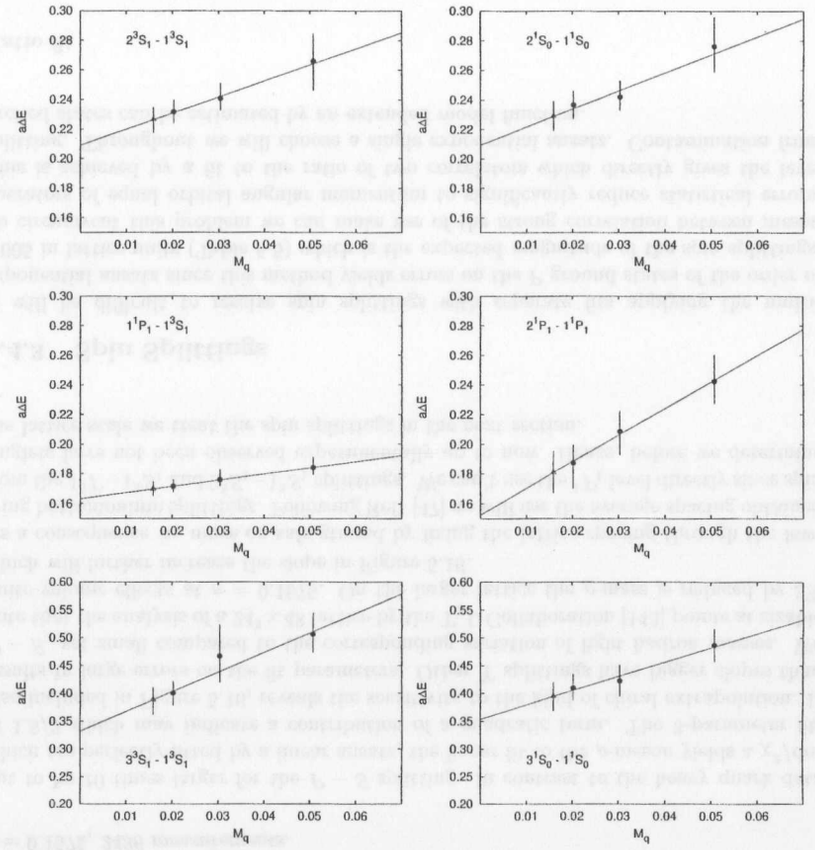

Figure 5.15. *Extrapolation of splittings between ground states and radial as well as orbital angular momentum excitations in dynamical quark mass to the relevant effective quark mass $m_s/3$. Filled circles are the measured data, open triangles mark the extrapolated values at am_{eff}.*

splitting	ΔE_0	c	$\Delta E(m_s/3)$	$\Delta E(m_l)$
$2^1S_0 - 1^1S_0$	0.209(21)	1.2(7)	0.229(10)	0.212(19)
$3^1S_0 - 1^1S_0$	0.354(43)	2.6(1.5)	0.394(27)	0.359(41)
$2^3S_1 - 1^3S_1$	0.209(18)	1.1(7)	0.226(9)	0.211(17)
$3^3S_1 - 1^3S_1$	0.332(41)	3.5(1.3)	0.388(27)	0.339(39)
$1^1P_1 - 1^3S_1$	0.163(9)	0.4(3)	0.170(5)	0.164(8)
$2^1P_1 - 1^1P_1$	0.152(24)	1.8(7)	0.181(15)	0.156(23)

Table 5.9. *Radial level splittings extrapolated to $m_s/3$ and the light quark mass m_l.*

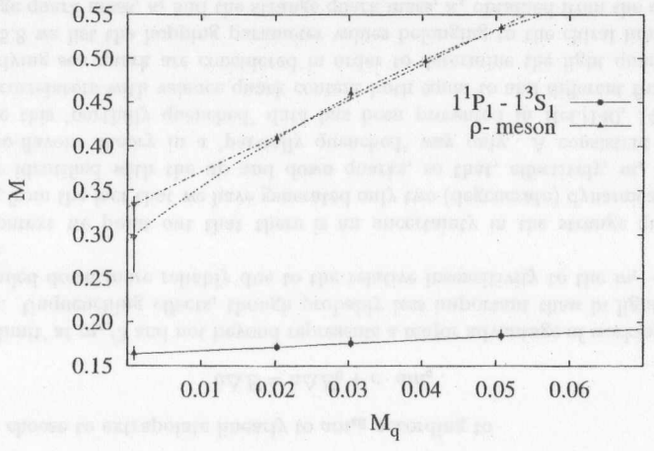

Figure 5.16. *Variation with sea-quark mass: The ρ-meson is compared to the $1^1P_1 - 1^3S_1$-splitting. The dotted line corresponds to a quadratic fit, the dashed-dotted line to a linear fit and open triangles mark the extrapolated values at κ_l. The data is taken from [124].*

$T_{\min}$	$T_{\max}$	ΔE	A	χ^2/dof	Q
10	30	$0.0135^{+0.0001}_{-0.0001}$	$0.9909^{+0.0013}_{-0.0013}$	20.3/19	0.379
12	30	$0.0135^{+0.0001}_{-0.0001}$	$0.9912^{+0.0013}_{-0.0014}$	20.0/17	0.272
14	30	$0.0134^{+0.0001}_{-0.0001}$	$0.9907^{+0.0017}_{-0.0017}$	19.6/15	0.186
16	30	$0.0134^{+0.0001}_{-0.0001}$	$0.9905^{+0.0020}_{-0.0020}$	19.0/13	0.123
18	30	$0.0135^{+0.0001}_{-0.0001}$	$0.9907^{+0.0026}_{-0.0025}$	14.6/11	0.204
20	30	$0.0135^{+0.0001}_{-0.0001}$	$0.9918^{+0.0032}_{-0.0029}$	14.1/9	0.118
22	30	$0.0134^{+0.0002}_{-0.0002}$	$0.9880^{+0.0037}_{-0.0037}$	8.6/7	0.282
24	30	$0.0132^{+0.0002}_{-0.0002}$	$0.9848^{+0.0052}_{-0.0048}$	6.0/5	0.305

Table 5.10. *Example of a ratio fit of the S hyperfine splitting, $\Delta E = \Delta E(1^3S_1 - 1^1S_0)$; $\kappa = 0.1575$, 2436 measurements.*

out to be 10 times larger for the $P - S$ splitting. In contrast to the heavy quark data which are perfectly fitted by a linear ansatz, the linear fit to the ρ-meson yields a χ^2/dof of 1.5/2 which may indicate a contribution of a quadratic term. The 3-parameter fit, also included in Figure 5.16, reveals the sensitivity to the kind of chiral extrapolation. It results in large errors on the fit parameters. Other Υ splittings have bigger slopes than $P - S$, yet small compared to the corresponding variation of light hadron masses. We note that the analysis of a $24^3 \times 48$ lattice by the $T_\chi L$ Collaboration [143] points at sizable finite-volume effects at $\kappa = 0.1575$. On the larger lattice the ρ-mass is reduced by 3% which will further increase the slope in Figure 5.16.

As a consequence we move on safe ground by fixing the lattice spacing through the low-lying bottomonium splittings. Following Ref. [47] we will use the average spacing obtained from the $1^3\bar{P} - 1^3S_1$ and $2^3S_1 - 1^3S_1$ splittings. We can't use the $^1P_1$ level directly since spin singlets have not been observed experimentally up to now. Hence, before we determine the lattice scale we treat the spin splittings in the next section.

5.4.3 Spin Splittings

It will be difficult to resolve spin splittings with separate fits applying the multi-exponential ansatz since this method yields errors on the P ground states of the order of 0.005 in lattice units (Table 5.5) which is the expected magnitude of the spin splittings. To circumvent this problem we can make use of the strong correlation between meson operators of equal orbital angular momentum to significantly reduce statistical errors. This is achieved by a fit to the ratio of two correlators which directly gives the level splitting. Throughout we will choose a single exponential ansatz. Contamination from excited states can be estimated by an extended model function.

Ratio fit

$$\frac{C_T^1}{C_T^2} = A \exp(-\Delta E T) \,, \tag{5.13}$$

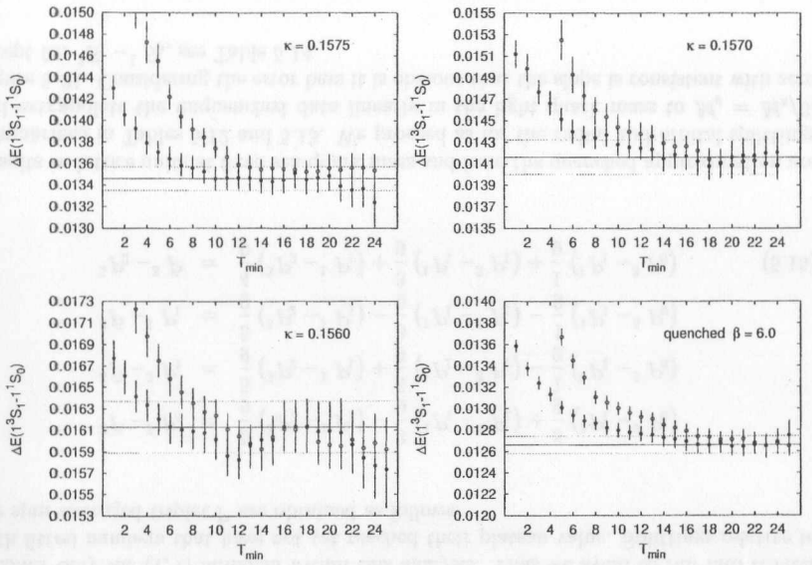

Figure 5.17. *Dependence of the fit result for the energy splitting $\Delta E(1^3S_1 - 1^1S_0)$ on the lower limit of the fit range, $T_{\min}$. The upper limit is fixed to $T_{\max} = 30$ for $\kappa = 0.1575, 0.1570$ and to $T_{\max} = 31$ for $\kappa = 0.1560$ and the quenched case. The splitting is obtained from a single exponential fit to the ratio of correlators $C_T(1^3S_1)/C_T(1^1S_0)$. Open circles indicate smeared-local data, filled circles smeared-smeared data. The solid line represents the selected value, the dashed line its 1σ-band.*

Extended ratio fit

$$\frac{C_T^1}{C_T^2} = A_1 \exp(-\Delta E_{12} T) \frac{1 + A_2 \exp(-\Delta E_1 T)}{1 + A_3 \exp(-\Delta E_2 T)} \,. \tag{5.14}$$

In Figure 5.17 we plot the $T_{\min}$ dependence of the fit result for the $1^3S_1 - 1^1S_0$ splitting. We show the result from both the smeared-local and smeared-smeared correlators, although we shall use only the smeared-smeared data. The fit is absolutely stable for $T_{\min} > 10 - 12$ (see also Table 5.10). Note that the total scale in Figure 5.17 is around 5 MeV! The corrected ratio fit confirms the single exponential ansatz. As is obvious from Table 5.11 the additional terms are zero within errors and the splitting δE_{12} is consistent with δE. For the fine structure in the $L = 1$ sector we compute the energy difference of each ^3P_J state relative to the singlet P. In Figures 5.18-5.20 we show $T_{\min}$ plots for $\Delta E(^1P_1 - ^3P_0)$, $\Delta E(^1P_1 - ^3P_1)$ and $\Delta E(^3P_2 - ^1P_1)$, respectively. Again, our final choice of fitted values is such that the statistical error encompasses the systematic uncertainty due to the fit interval. Here, the discrepancy between fits to $(1, l)$ and $(1, 1)$ correlators is much more pronounced than for the S hyperfine splitting. Deviating from [60], where we quoted

range	ΔE_{12}	ΔE_1	ΔE_2
[10, 30]	0.01346(25)	-0.000(70)	-0.000(73)
[12, 30]	0.01346(55)	0.001(85)	0.001(41)
[14, 30]	0.01344(71)	0.00(47)	0.00(48)

Table 5.11. *Example of extended ratio fits for the S hyperfine splitting based on the same data sample as in Table 5.10.*

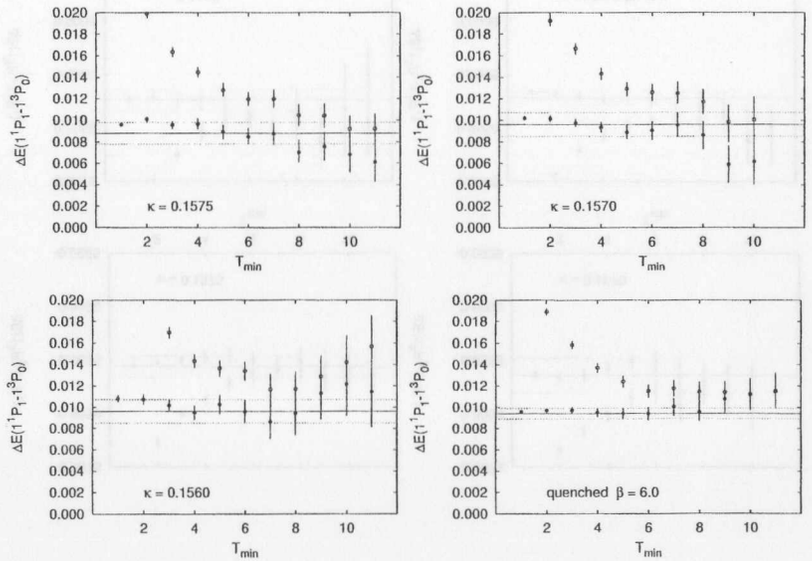

Figure 5.18. *$T_{\min}$ dependence of the fit result for $\Delta E(1^1P_1 - 1^3P_0)$. Open circles indicate smeared-local data, filled circles smeared-smeared data.*

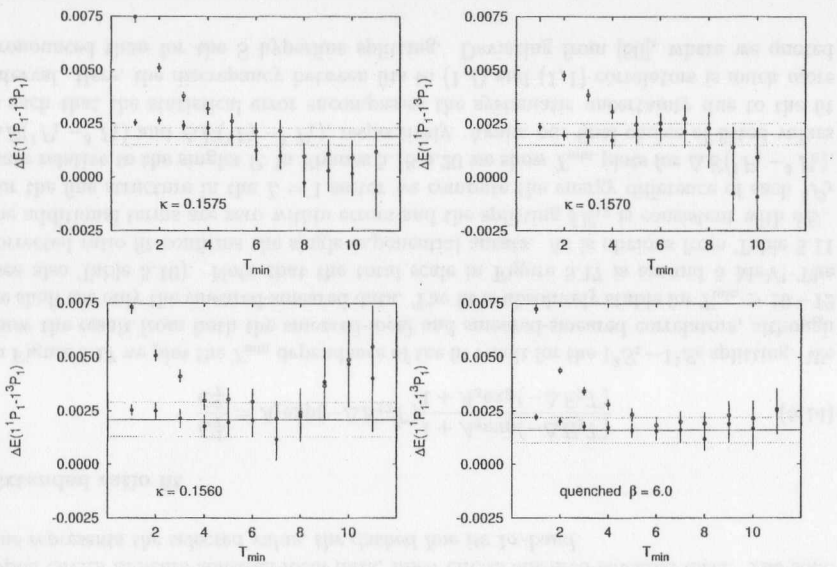

Figure 5.19. *$T_{\min}$ dependence of the fit result for $\Delta E(1^1P_1 - 1^3P_1)$. Open circles indicate smeared-local data, filled circles smeared-smeared data.*

the average fit result from the smeared-local and smeared-smeared data we will take into account only the $(1,1)$ numbers within this analysis. Thus we avoid to run into trouble with fitted numbers that have not yet reached their plateau value. Splittings relative to the spin-averaged triplet P are obtained as follows:

$$
\begin{aligned}
{}^3\bar{P} - {}^3P_0 &= \frac{5}{9}\left({}^3P_2 - {}^1P_1\right) - \frac{3}{9}\left({}^1P_1 - {}^3P_1\right) + \frac{8}{9}\left({}^1P_1 - {}^3P_0\right) \\
{}^3\bar{P} - {}^3P_1 &= \frac{5}{9}\left({}^3P_2 - {}^1P_1\right) + \frac{6}{9}\left({}^1P_1 - {}^3P_1\right) - \frac{1}{9}\left({}^1P_1 - {}^3P_0\right) \\
{}^3\bar{P} - {}^1P_1 &= \frac{5}{9}\left({}^3P_2 - {}^1P_1\right) - \frac{3}{9}\left({}^1P_1 - {}^3P_1\right) - \frac{1}{9}\left({}^1P_1 - {}^3P_0\right) \\
{}^3P_2 - {}^3\bar{P} &= \frac{4}{9}\left({}^3P_2 - {}^1P_1\right) + \frac{3}{9}\left({}^1P_1 - {}^3P_1\right) + \frac{1}{9}\left({}^1P_1 - {}^3P_0\right) . \qquad (5.15)
\end{aligned}
$$

Results in lattice units at fixed sea-quark mass and from the quenched approximation are summarised in Tables 5.12 and 5.13. We proceed as for the radial and orbital splittings and extrapolate the unquenched data linearly in the light quark mass to $M_q = M_s/3$, Figure 5.21. Considering the error bars it is obvious that the slope is consistent with zero except for ${}^3S_1 - {}^1S_0$, see Table 5.14.

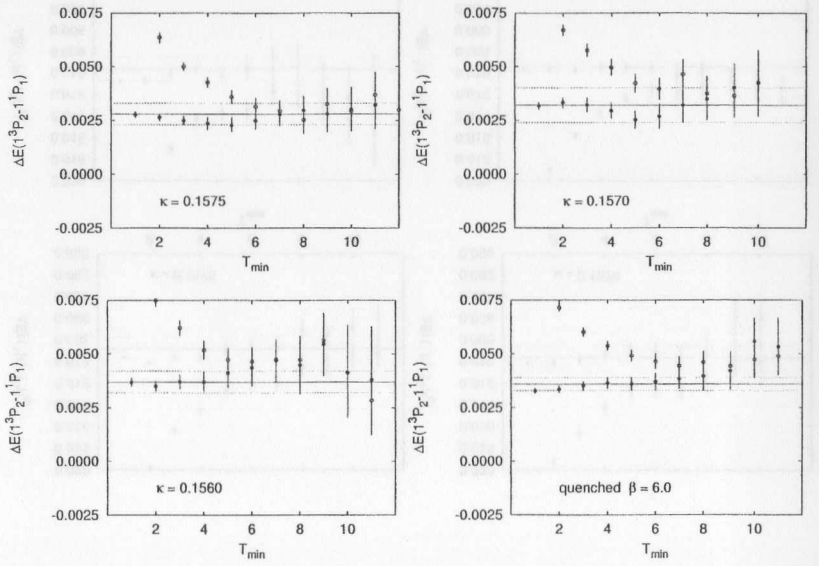

Figure 5.20. *$T_{\min}$ dependence of the fit result for $\Delta E(1^3P_2 - 1^1P_1)$. Open circles indicate smeared-local data, filled circles smeared-smeared data.*

splitting	range	χ^2/dof	ΔE	A
$\kappa = 0.1575$				
$1^3S_1 - 1^1S_0$ {(1,1)}	[10, 30]	20.3/19	0.01346(11)	0.9909(13)
$1^3P_2 - 1^1P_1$ {(1,1)}	[7, 30]	8.0/22	0.0028(5)	1.0035(43)
$1^1P_1 - 1^3P_1$ {(1,1)}	[5, 30]	49.5/24	0.0019(4)	0.9970(23)
$1^1P_1 - 1^3P_0$ {(1,1)}	[7, 30]	29.0/22	0.0088(10)	0.9983(80)
$\kappa = 0.1570$				
$1^3S_1 - 1^1S_0$ {(1,1)}	[20, 30]	3.5/9	0.01416(16)	0.9871(30)
$1^3P_2 - 1^1P_1$ {(1,1)}	[7, 15]	4.5/7	0.0032(8)	1.0031(65)
$1^1P_1 - 1^3P_1$ {(1,1)}	[5, 15]	13.5/9	0.0020(5)	1.0002(29)
$1^1P_1 - 1^3P_0$ {(1,1)}	[7, 15]	11.8/7	0.0096(11)	1.0037(91)
$\kappa = 0.1560$				
$1^3S_1 - 1^1S_0$ {(1,1)}	[16, 31]	5.6/14	0.01613(24)	0.9931(43)
$1^3P_2 - 1^1P_1$ {(1,1)}	[4, 31]	23.4/26	0.0037(5)	1.0029(23)
$1^1P_1 - 1^3P_1$ {(1,1)}	[6, 31]	25.6/24	0.0021(8)	0.9988(60)
$1^1P_1 - 1^3P_0$ {(1,1)}	[6, 31]	14.9/24	0.0096(11)	0.9979(73)
quenched	$\beta = 6.0$			
$1^3S_1 - 1^1S_0$ {(1,1)}	[17, 31]	9.8/13	0.01266(8)	0.9863(16)
$1^3P_2 - 1^1P_1$ {(1,1)}	[5, 31]	24.2/25	0.0036(3)	1.0038(19)
$1^1P_1 - 1^3P_1$ {(1,1)}	[7, 31]	28.6/23	0.0016(6)	0.9975(45)
$1^1P_1 - 1^3P_0$ {(1,1)}	[5, 31]	26.9/25	0.0094(5)	1.0033(31)

Table 5.12. *Results obtained from fitting a single exponential to the ratio of two correlators.*

	$n_f = 2, \beta = 5.6$			$n_f = 0, \beta = 6.0$
Splitting	$\kappa = 0.1560$	$\kappa = 0.1570$	$\kappa = 0.1575$	
$1^3P_2 - 1\bar{P}$	0.0034(4)	0.0032(4)	0.0028(4)	0.0032(3)
$1\bar{P} - 1^3P_1$	0.0024(5)	0.0021(5)	0.0018(3)	0.0020(4)
$1\bar{P} - 1^3P_0$	0.0099(10)	0.0096(11)	0.0087(10)	0.0098(5)
$1\bar{P} - 1^1P_1$	0.0003(4)	0.0000(5)	-0.0001(3)	0.0004(3)

Table 5.13. *Spin splittings relative to the spin-averaged ^3P level for fixed sea-quark mass as well as in the quenched approximation.*

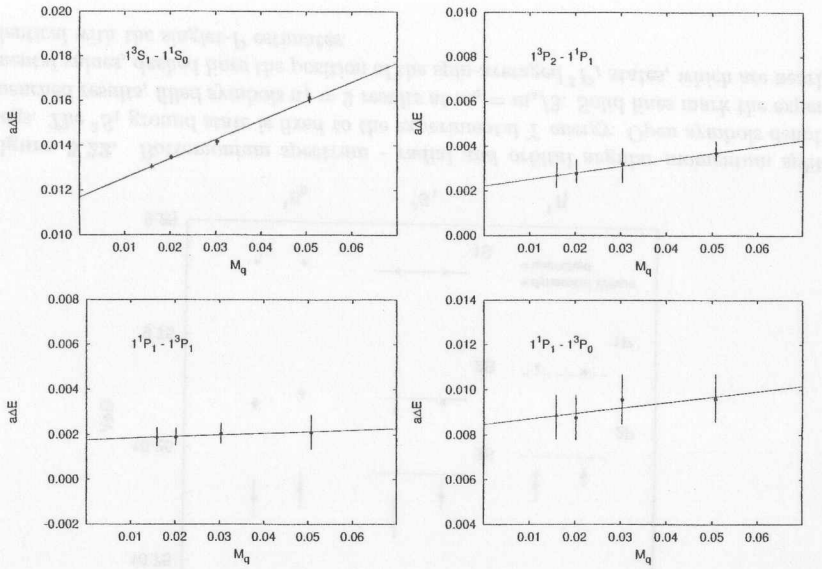

Figure 5.21. *Linear extrapolation of spin splittings in the dynamical quark mass to $m_s/3$.*

splitting	ΔE_0	c	$\Delta E(M_s/3)$	$\Delta E(M_l)$
$1^3\bar{P} - 1^3S_1$	0.163(9)	0.43(27)	0.170(5)	0.164(8)
$1^3S_1 - 1^1S_0$	0.01168(23)	0.086(8)	0.01304(12)	0.01185(22)
$1^3P_2 - 1^1P_1$	0.0022(10)	0.029(26)	0.0027(6)	0.0023(10)
$1^1P_1 - 1^3P_1$	0.0018(9)	0.007(31)	0.0019(4)	0.0018(8)
$1^1P_1 - 1^3P_0$	0.0085(17)	0.024(51)	0.0088(10)	0.0085(17)
$1^3P_2 - 1^3\bar{P}$	0.0025(6)	0.018(19)	0.0028(3)	0.0026(5)
$1^3\bar{P} - 1^3P_1$	0.0015(7)	0.018(21)	0.0018(4)	0.0015(7)
$1^3\bar{P} - 1^3P_0$	0.0082(16)	0.035(45)	0.0087(10)	0.0082(15)
$1^3\bar{P} - 1^1P_1$	-0.0003(7)	0.012(21)	-0.0001(4)	-0.0003(6)

Table 5.14. *Spin splittings extrapolated to the effective quark mass $m_{\text{eff}}/3$ and the light quark mass.*

	Splitting	a^{-1}[GeV]	Average a^{-1}[GeV]	R_{SP}	R_{PP}
$n_f = 0, \beta = 6.0$	$\Upsilon' - \Upsilon$	2.29(11)	2.49(7)	1.49(10)	0.67(11)
	$\bar{\chi} - \Upsilon$	2.68(9)			
$\kappa = 0.1560$	$\Upsilon' - \Upsilon$	2.12(16)	2.25(10)	1.44(10)	0.77(18)
	$\bar{\chi} - \Upsilon$	2.38(8)			
$\kappa = 0.1570$	$\Upsilon' - \Upsilon$	2.34(9)	2.42(6)	1.37(7)	0.70(16)
	$\bar{\chi} - \Upsilon$	2.50(8)			
$\kappa = 0.1575$	$\Upsilon' - \Upsilon$	2.43(8)	2.50(6)	1.35(6)	0.68(12)
	$\bar{\chi} - \Upsilon$	2.57(7)			
$m_s/3$	$\Upsilon' - \Upsilon$	2.49(10)	2.54(6)	1.33(6)	0.66(12)
	$\bar{\chi} - \Upsilon$	2.59(7)			

Table 5.15. *Determination of the lattice spacing from the $2^3S_1 - 1^3S_1$ and $1^3\bar{P} - 1^3S_1$ splittings. We use the average value to convert our results to physical units. R_{SP} is to be compared to the experimental value of 1.28.*

5.5 Physical Results

To convert the splittings computed in the previous section into physical units we have to determine the lattice spacing, a. This presents an easier task in heavy quarkonium than it does in the light hadron sector. It has already been mentioned that the dependence on the sea-quark mass is much less severe for the lowest radial and orbital bottomonium splittings than for the ρ-meson or the nucleon. In addition, these are insensitive to the heavy quark mass. In the absence of an experimental number for the singlet states in bottomonium we shall here use the $2^3S_1 - 1^3S_1$ and $1^3\bar{P} - 1^3S_1$ splittings,

$$a^{-1} = \frac{0.5629\mathrm{GeV}}{aE(2^3S_1) - aE(1^3S_1)|_{M_s/3}}, \quad a^{-1} = \frac{0.4398\mathrm{GeV}}{aE(^3\bar{P}) - aE(1^3S_1)|_{M_s/3}}. \tag{5.16}$$

Results for lattice spacings are summarised in Table 5.15. Note that the average spacing for $\beta = 5.6$, $n_f = 2$ at $M_q = M_s/3$ agrees well with the quenched one at $\beta = 6.0$, so that we can directly compare our results in both theories. In Table 5.16 we list the results in physical units. We have used the average a^{-1} to obtain these numbers and thus distribute the mismatch between both determinations on S and P states.

Gross level structure

Figure 5.22 summarises our results for two and zero flavours from Table 5.16. It is obvious that the gross level structure, i.e. the radial and orbital angular momentum splittings, computed on quenched configurations disagrees with experiment. This is as expected since the coupling constant will run incorrectly between the scales dominating the $L = 0$ and $L = 1$ bound states. There is no effective coupling that gives the correct answer for both the 1P and 2S states within the quenched approximation.
The $n_f = 2$ lattice results are in much closer agreement with the experimental data. This is also evident from Table 5.15 which shows that the lattice spacings from the $2S - 1S$ and the $1S - 1P$ splittings do not agree in the quenched theory whereas they coincide

	Simulation Result [GeV]		Experiment[144]
Splitting	$n_f = 2$, $\beta = 5.6$, $m_s/3$	$n_f = 0$, $\beta = 6.0$	
$2^1S_0 - 1^1S_0$	0.581(21)	0.625(21)	
$3^1S_0 - 1^1S_0$	1.00(7)	1.04(8)	
$2^3S_1 - 1^3S_1$	0.575(14)	0.610(21)	0.5629
$3^3S_1 - 1^3S_1$	0.99(6)	1.09(9)	0.895
$1^1P_1 - 1^3S_1$	0.431(10)	0.407(12)	
$2^1P_1 - 1^1P_1$	0.459(40)	0.528(66)	
$1\bar{P} - 1^3S_1$	0.431(10)	0.408(12)	0.4398
$1^3S_1 - 1^1S_0$	0.0331(9)	0.0315(9)	
$1^3P_2 - 1^1P_1$	0.0068(16)	0.0089(8)	
$1^1P_1 - 1^3P_1$	0.0048(12)	0.0040(15)	
$1^1P_1 - 1^3P_0$	0.0225(27)	0.0234(15)	
$1^3P_2 - 1\bar{P}$	0.0071(9)	0.0079(7)	0.0130
$1\bar{P} - 1^3P_1$	0.0045(10)	0.0050(10)	0.0083
$1\bar{P} - 1^3P_0$	0.0222(26)	0.0244(13)	0.040
$1\bar{P} - 1^1P_1$	-0.0003(10)	0.0010(7)	

Table 5.16. *Overview of our results in physical units. The scale is set by the average $P - S$ and $2S - 1S$ splitting.*

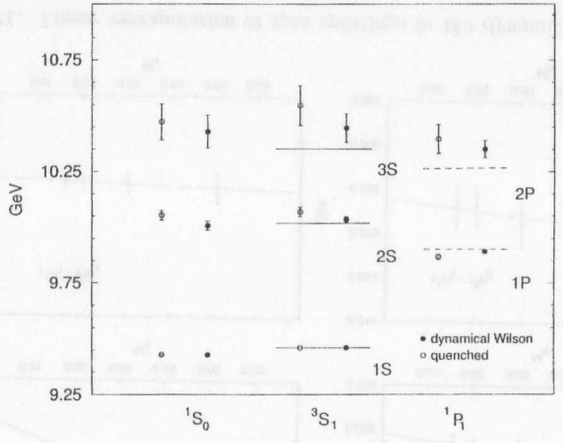

Figure 5.22. *Bottomonium spectrum - radial and orbital angular momentum splittings. The $^3S_1$ ground state is fixed to the experimental Υ energy. Open symbols denote quenched results, filled symbols $n_f = 2$ results at $m_q = m_s/3$. Solid lines mark the experimental values, dashed lines the position of the spin-averaged ^3P_J states, which are nearly identical with the singlet-P estimates.*

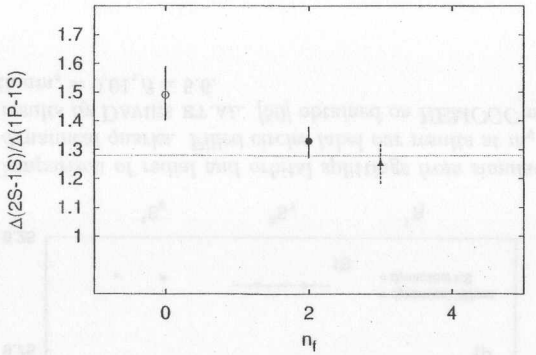

Figure 5.23. *The ratio $R_{SP} = 2^3S_1 - 1^3S_1/1^3\bar{P} - 1^3S_1$ in bottomonium as a function of the number of dynamical flavours.*

when two dynamical quarks are switched on. The ratio of these splittings is plotted in Figure 5.23 as a function of the number of dynamical flavours. Whereas the quenched result is off the experimental number by 1-2 σ, we find a ratio for $n_f = 2$ which is nicely consistent with it. Note, however, that this value moved up by one standard deviation compared to our previous estimate with smaller statistics [60] which may hint at three active flavours rather than two. Figure 5.23 includes the ratio R_{SP} that one obtains by extrapolation to $n_f = 3$. Like the two-flavour result it is in agreement with experiment.

To summarise: in the radial and orbital splittings we observe a clear trend towards experiment, once the vacuum polarisation is partly included. The effect is at the level of one or two standard deviations.

Spin Splittings

We do not observe any significant impact of unquenching on the spin-dependent splittings. In particular, the P fine structure seems to be largely underestimated for both $n_f = 0$ and $n_f = 2$ as shown in Figure 5.24. The S hyperfine splitting, too, remains constant within errors. From a perturbative viewpoint this is perhaps not too unexpected if one recognises that SESAM's investigation of the static quark potential [83] finds unquenching to induce only a small increase of about 10% in the Coulomb coefficient.

We note that the ratio $R_{PP} = \Delta E(1^3P_2 - 1^3P_1)/\Delta E(1^3P_1 - 1^3P_0)$ is in agreement with the experimental value 0.66, Figure 5.25. A similar result was obtained in [48], where R_{PP} has been found to change from 1.11(26) to 0.56(19) when next-to-leading spin-dependent relativistic corrections are included. There is another interesting observation: from potential models one expects that spin-orbit and tensor contributions sum up to zero leading to degeneracy between spin-averaged ^3P and singlet P states

$$E(n\,^3\bar{P}) = E(n\,^1P_1)\,. \tag{5.17}$$

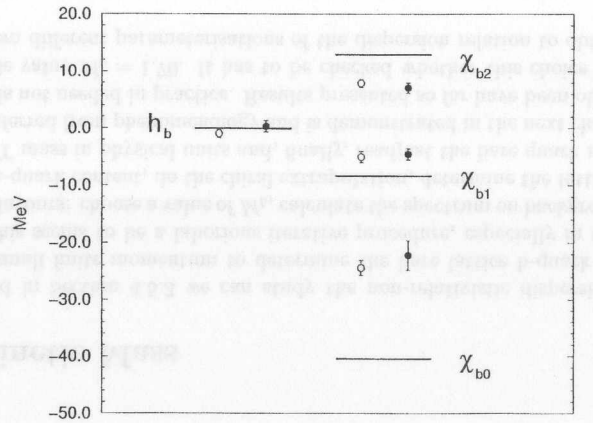

Figure 5.24. *Bottomonium spectrum - P fine structure. Open symbols denote quenched results, filled symbols $n_f = 2$ results at $m_q = m_s/3$. Solid lines mark experimental values for triplet P and the spin average of these since the h_b has not been observed. Note that the unquenched $^1P_1$ data point agrees with $^3\bar{P}$ as predicted by potential models.*

Figure 5.24 reveals that the unquenched $^1P_1$ result confirms this expectation whereas the quenched singlet P state is smaller than $^3\bar{P}$.
It is reasonable to assume that the spin splittings are much more sensitive to the details of the quark action than radial and orbital splittings. Therefore, we will attempt to disentangle the different systematic uncertainties in the next chapter.

Wilson versus Kogut-Susskind Staggered Quarks

We compare our spectrum results with an earlier NRQCD calculation of bottomonium on unquenched gauge field configurations. DAVIES ET.AL. [50] have been the first to include the effects of dynamical quarks applying the Kogut-Susskind staggered discretisation. They analysed HEMCGC configurations with $am = 0.01, 0.025$ using an NRQCD action of $O(m_b v^4)$ and chose $u_0 = u_0^P$. The bare b-quark mass was $M_b = 1.8$ which a posteriori turned out to be slightly too large [138]. Since the statistics for $am_q = 0.025$ was lower than for $am_q = 0.01$, however, there was no lever-arm for an extrapolation in the dynamical quark mass.
In Figure 5.26 we compare the gross level structure obtained in [50] with our results. There is excellent agreement for 2S-1S and 1P-1S. Both simulations also give consistent 3S and 2P energies, although within large errors.
The situation is much less clear for the P fine structure as shown in Figure 5.27. Our

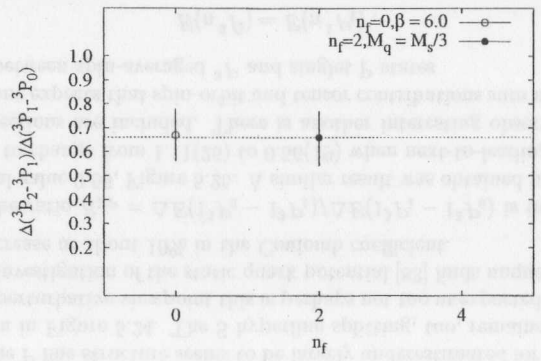

Figure 5.25. *The ratio $R_{PP} = \Delta(1^3P_2 - 1^3P_1)/\Delta(1^3P_1 - 1^3P_0)$ in bottomonium as a function of the number of dynamical flavours. The experimental number 0.66 is indicated by the dashed line.*

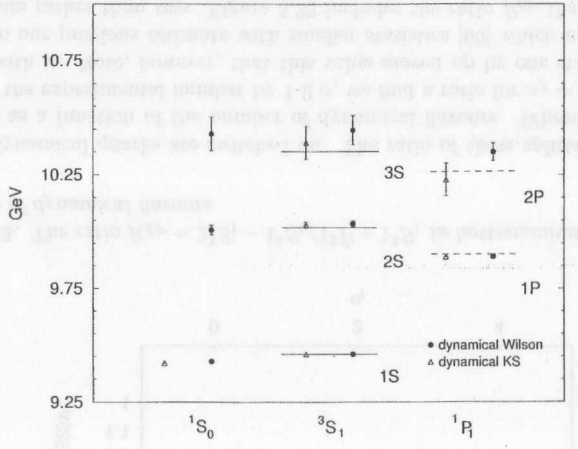

Figure 5.26. *Comparison of radial and orbital splittings from simulations using configurations with dynamical quarks. Filled circles label our results at $m_q = m_s/3$. Open triangles denote results by* DAVIES ET.AL. *[50] obtained on HEMCGC $n_f = 2$ staggered configuration with $am_q = 0.01, \beta = 5.6$.*

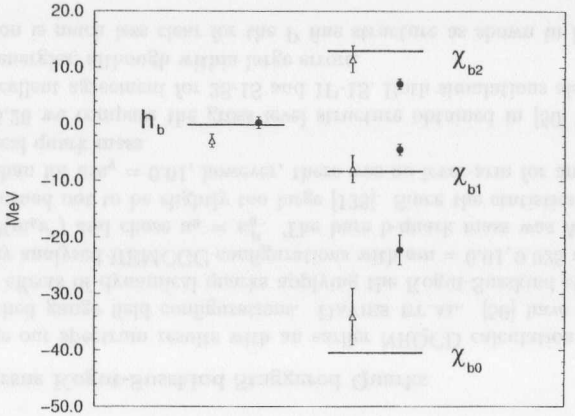

Figure 5.27. *Comparison of the P fine structure from simulations using configurations with dynamical quarks. Same labeling as in Figure 5.26.*

results have smaller errors than the staggered data. We are thus able to reveal a discrepancy between both simulations: whereas the staggered data reproduce the experimental spin splittings quite well, the Wilson result underestimates them considerably. However, no firm conclusion about the fermion formulation can be drawn from Figure 5.27 since the difference in the NRQCD actions do affect the spin splittings. The investigation of systematic errors in the next chapter indicates that the larger splittings obtained with the staggered configurations are more likely due to the lower-order action than to different fermionic discretisation schemes.

5.6 Kinetic Mass

As discussed in Section 4.5.3 we can study the non-relativistic dispersion relation for mesons at small finite momentum to determine the bare lattice b-quark mass, M_b. At first sight this seems to be a laborious iterative procedure, especially in the presence of dynamical flavours: choose a value of M_b, calculate the spectrum on background fields with different sea-quark content, do the chiral extrapolation, determine the lattice spacing and the kinetic Υ mass in physical units and, finally, readjust the bare quark mass. However, it may be inferred from phenomenology and is demonstrated in the next chapter that such fine tuning is not needed in practice. Results presented so far have been obtained entirely with a single value $M_b = 1.70$. It has to be checked whether this choice is appropriate. We apply two different parameterisations of the dispersion relation to obtain the kinetic

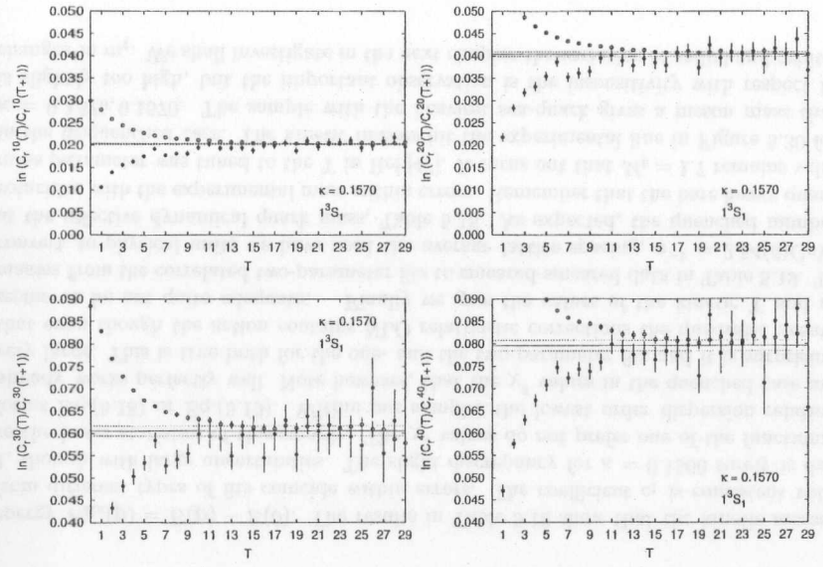

Figure 5.28. *Effective masses belonging to the ratio of finite-momentum correlators to the zero-momentum correlator. Open circles indicate smeared-local data, filled circles smeared-smeared data.*

mass

$$E(\mathbf{p}) - E(0) = \frac{\mathbf{p}^2}{2m_{\text{kin}}} \tag{5.18}$$

$$E(\mathbf{p}) - E(0) = \frac{\mathbf{p}^2}{2m_{\text{kin}}} - c_1 \frac{(\mathbf{p}^2)^2}{8m_{\text{kin}}^3} \,. \tag{5.19}$$

In a relativistic theory m_{kin} equals the rest mass and $c_1 = 1$. The non-relativistic approximation will reproduce this value up to corrections of $O(v^2)$. We choose to extract the splitting between finite-momentum and zero-momentum correlators from single exponential ratio fits

$$C_r^{p0}(T) \equiv \frac{C^p(T)}{C^0(T)} = A\, \mathrm{e}^{-(aE(\mathbf{p})-aE(0))T} + \text{corrections} \,, \tag{5.20}$$

We have computed correlators with momenta $|p| = 1, \sqrt{2}, \sqrt{3}, 2$ in units of $2\pi/16a$ and averaged over all possible polarisations. Figure 5.28 presents effective mass plots for the ratio in Eq. (5.20). Both $(1,l)$ and $(1,1)$ smearings are shown. The results are summarised in Table 5.17. In most cases smeared-smeared correlators give splittings that are smaller than smeared-local ones by about one standard deviation. Only the former are used to determine M_{kin}. We have tried correlated and uncorrelated fits of the kinetic

state	$\lvert p\rvert$	smeared - local			smeared - smeared		
		range	χ^2/dof	aE_{kin}	range	χ^2/dof	aE_{kin}
$\kappa = 0.1575$							
1^1S_0	1	[15, 30]	6.0/14	0.02059(12)	[17, 30]	11.4/12	0.02037(14)
1^1S_0	$\sqrt{2}$	[15, 30]	9.9/14	0.04101(27)	[17, 30]	15.0/12	0.04056(37)
1^1S_0	$\sqrt{3}$	[15, 30]	13.3/14	0.06119(54)	[15, 30]	16.5/14	0.06027(78)
1^1S_0	2	[15, 30]	7.5/14	0.08169(66)	[17, 30]	8.3/12	0.08132(108)
1^3S_1	1	[15, 30]	6.0/14	0.02048(13)	[17, 30]	12.2/12	0.02022(21)
1^3S_1	$\sqrt{2}$	[15, 30]	8.1/14	0.04077(30)	[17, 30]	15.8/12	0.04019(47)
1^3S_1	$\sqrt{3}$	[15, 30]	9.0/14	0.06100(63)	[15, 30]	16.8/14	0.05969(96)
1^3S_1	2	[15, 30]	6.7/14	0.08134(78)	[17, 30]	8.6/12	0.08066(119)
$\kappa = 0.1570$							
1^1S_0	1	[15, 30]	5.4/14	0.02063(11)	[16, 30]	11.6/13	0.02047(14)
1^1S_0	$\sqrt{2}$	[15, 30]	3.7/14	0.04129(25)	[17, 30]	7.3/12	0.04088(37)
1^1S_0	$\sqrt{3}$	[15, 30]	4.8/14	0.06189(61)	[17, 30]	4.9/12	0.06134(84)
1^1S_0	2	[15, 30]	7.5/14	0.08175(62)	[16, 30]	12.1/13	0.08107(83)
1^3S_1	1	[15, 30]	3.1/14	0.02045(13)	[16, 30]	12.9/13	0.02024(20)
1^3S_1	$\sqrt{2}$	[15, 30]	3.2/14	0.04092(33)	[17, 30]	8.3/12	0.04040(49)
1^3S_1	$\sqrt{3}$	[15, 30]	5.9/14	0.06136(72)	[17, 30]	6.1/12	0.06055(113)
1^3S_1	2	[15, 30]	4.0/14	0.08090(75)	[16, 30]	13.5/13	0.07960(116)
$\kappa = 0.1560$							
1^1S_0	1	[15, 31]	15.6/15	0.02037(19)	[16, 31]	11.2/14	0.01999(22)
1^1S_0	$\sqrt{2}$	[15, 31]	19.6/15	0.04051(46)	[15, 31]	8.7/15	0.03950(52)
1^1S_0	$\sqrt{3}$	[15, 31]	25.6/15	0.06051(108)	[15, 31]	11.3/15	0.05889(133)
1^1S_0	2	[15, 31]	18.1/15	0.08082(106)	[15, 31]	15.7/15	0.07952(121)
1^3S_1	1	[15, 31]	14.8/15	0.02023(24)	[10, 31]	10.3/20	0.01959(23)
1^3S_1	$\sqrt{2}$	[15, 31]	14.2/15	0.04005(62)	[10, 31]	11.8/20	0.03894(63)
1^3S_1	$\sqrt{3}$	[15, 31]	15.7/15	0.05987(129)	[10, 31]	17.3/20	0.05839(126)
1^3S_1	2	[15, 31]	12.7/15	0.08134(116)	[10, 31]	14.8/20	0.07894(102)
quenched	$\beta = 6.0$						
1^1S_0	1	[20, 31]	14.0/10	0.02056(11)	[15, 31]	13.0/15	0.02026(12)
1^1S_0	$\sqrt{2}$	[20, 31]	14.6/10	0.04141(27)	[15, 31]	13.3/15	0.04075(30)
1^1S_0	$\sqrt{3}$	[20, 31]	17.5/10	0.06304(68)	[15, 31]	16.8/15	0.06178(61)
1^1S_0	2	[20, 31]	16.9/10	0.08075(75)	[15, 31]	15.5/15	0.07972(67)
1^3S_1	1	[17, 31]	11.6/13	0.02040(12)	[15, 31]	15.3/15	0.02007(15)
1^3S_1	$\sqrt{2}$	[17, 31]	14.8/13	0.04084(31)	[15, 31]	13.6/15	0.04040(34)
1^3S_1	$\sqrt{3}$	[17, 31]	20.6/13	0.06160(65)	[15, 31]	17.5/15	0.06148(75)
1^3S_1	2	[17, 31]	18.1/13	0.08045(68)	[15, 31]	16.5/15	0.07897(81)

Table 5.17. *Results of ratio fits of finite-momentum correlators for singlet-S and triplet-S states.*

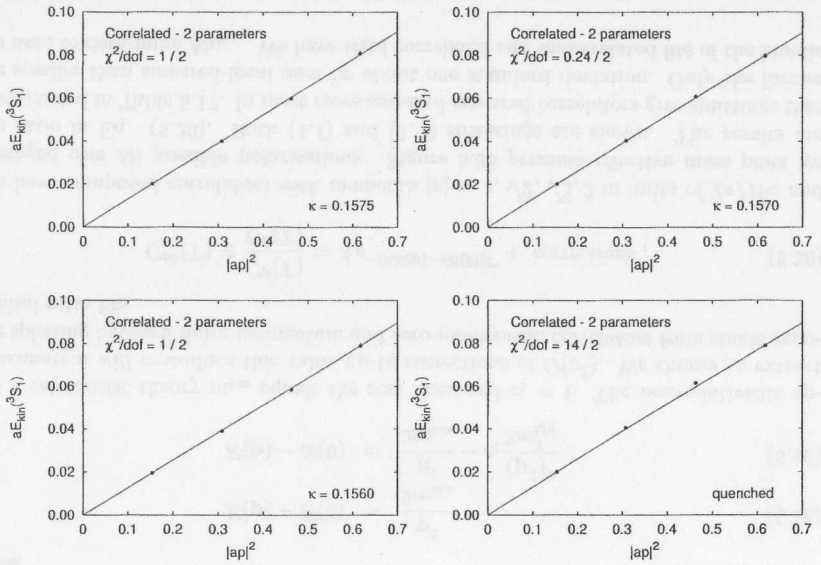

Figure 5.29. *Correlated two-parameter fits of the non-relativistic dispersion relation for ${}^3S_1$ according to Eq.(5.19). The kinetic energy is plotted versus $(2\pi/16)^2|n|^2$ with $n = (1,0,0),(0,1,0),(0,0,1),(1,1,0),(1,0,1),(0,1,1),(1,1,1),(2,0,0),(0,2,0),(0,0,2)$. Note the large χ^2 for the quenched data.*

energy $E_{\rm kin}(\mathbf{p}) = E(\mathbf{p}) - E(0)$. The results in Table 5.18 show that the kinetic masses from different types of fits coincide within errors. The coefficient c_1 is consistent with 1, though with large uncertainties. The slight discrepancy for $\kappa = 0.1560$ surely is due to the lower statistics of this sample. The χ^2 values do not prefer one of the functional forms Eq.(5.18) or Eq.(5.19). Within our samples the lowest order dispersion relation already works perfectly well. Note however, that the χ^2 values in the quenched case are very large. This is true both for the one- and the two-parameter fits and it is surprising that even though the action contains NLO relativistic corrections the quadratic ansatz seems to be not quite adequate. Finally we give the values of the kinetic Υ and η_b masses from the correlated two-parameter fits to smeared-smeared data in Table 5.19. To convert to physical units we have used the average lattice spacing, $a^{-1} = 2.54(6)$GeV, at the effective dynamical quark mass, Table 5.15. As expected, the quenched number coincides with the experimental mass within errors. Remember that the bare heavy quark mass parameter was tuned to the Υ in Ref.[47]. It turns out that $M_b = 1.7$ remains valid in the unquenched case. The kinetic masses hit the experimental line in Figure 5.30 for $\kappa = 0.1575, 0.1570$. The sample with the heaviest sea-quark gives a meson mass that is slightly too high, but the important observation is the insensitivity with respect to changes in m_q. We shall investigate in the next chapter the variation of radial and orbital

state	$N_{\rm par}$	χ^2/dof		$M_{\rm kin}$		c_1	
		U	C	U	C	U	C
$\kappa = 0.1575$							
${}^3S_1$	1	0.82/3	1.6/3	3.832(39)	3.821(36)		
${}^3S_1$	2	0.65/2	1/2	3.813(40)	3.814(39)	0.86(1.2)	0.78(1.1)
${}^1S_0$	1	0.89/3	1.7/3	3.800(33)	3.789(28)		
${}^1S_0$	2	0.65/2	1.2/2	3.782(30)	3.787(29)	0.84(1.1)	0.65(1.0)
$\kappa = 0.1570$							
${}^3S_1$	1	1.1/3	3.7/3	3.825(40)	3.804(36)		
${}^3S_1$	2	0.19/2	0.24/2	3.785(37)	3.790(34)	1.87(97)	1.79(97)
${}^1S_0$	1	0.7/3	2.3/3	3.776(27)	3.763(25)		
${}^1S_0$	2	0.14/2	0.17/2	3.754(26)	3.756(25)	1.05(77)	1.02(76)
$\kappa = 0.1560$							
${}^3S_1$	1	0.95/3	1.4/3	3.935(51)	3.918(46)		
${}^3S_1$	2	0.41/2	1/2	3.957(55)	3.927(49)	-0.97(1.1)	-0.60(1.0)
${}^1S_0$	1	0.82/3	2.5/3	3.881(49)	3.863(44)		
${}^1S_0$	2	0.64/2	1.9/2	3.861(43)	3.853(40)	0.98(1.28)	1.08(1.21)
quenched $\beta = 6.0$							
${}^3S_1$	1	6.3/3	20/3	3.837(32)	3.828(25)		
${}^3S_1$	2	5.7/2	14/2	3.812(26)	3.832(25)	1.13(67)	1.57(66)
${}^1S_0$	1	7.5/3	26/3	3.804(24)	3.779(20)		
${}^1S_0$	2	6.3/2	14/2	3.777(20)	3.790(20)	1.25(54)	1.70(52)

Table 5.18. *Linear and quadratic fits of the non-relativistic dispersion relation based on smeared-smeared finite-momentum data. (C)orrelated and (U)ncorrelated fits work out equally well.*

κ	state	$m_{\rm kin}$ [GeV]
0.1575	${}^3S_1$	9.68(27)
	${}^1S_0$	9.62(26)
0.1570	${}^3S_1$	9.63(24)
	${}^1S_0$	9.54(24)
0.1560	${}^3S_1$	9.97(28)
	${}^1S_0$	9.78(26)
quenched	${}^3S_1$	9.52(26)
	${}^1S_0$	9.42(26)

Table 5.19. *Υ and η_b kinetic masses in physical units. Lattice numbers from correlated two-parameter fits have been converted into physical units using $a^{-1} = 2.54(6)$GeV for $n_f = 2$ data and $a^{-1} = 2.49(7)$GeV in the quenched case.*

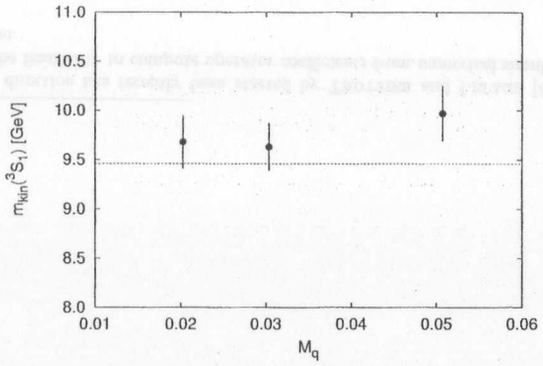

Figure 5.30. *Υ kinetic mass in physical units as a function of the sea-quark mass.*

splittings with $M_{\rm kin}$. We find no visible dependence within a large range of quark masses confirming the experimental observation. Therefore the iterative procedure outlined above is not necessary in practice.

5.7 Summary

We have presented a detailed study of dynamical quark effects in $b\bar{b}$ bound states. We computed radial and orbital angular momentum splittings as well as spin-splittings from a next-to-leading order lattice NRQCD action. With improved smearing techniques clean signals for ground and excited states have been obtained.

We have studied the light quark mass and flavour dependence of the $b\bar{b}$ spectrum. All quantities were linearly extrapolated to $m_s/3$. We are helped in these extrapolations by the fact that $m_s/3$ is very close to our lightest sea-quark mass so that the extrapolated values are easily consistent within errors with the values at $\kappa = 0.1575$. The lattice spacing has been determined after 'chiral extrapolation' with an error of 2-3%, which accounts for the statistical and systematic (fitting) uncertainties.

Comparing to the quenched calculation at similar lattice spacing we find a small unquenching effect in the radial and orbital splittings which can be quantified by the ratio $R_{\rm SP} = 2^3S_1 - 1^3S_1/1^3\bar{P} - 1^3S_1$ determined to be 1.33(6) with two dynamical flavours and 1.49(10) for the quenched case, the experimental value being 1.28.

We have succeeded in determining spin splittings with an accuracy of a few MeV. This allows us to discover even very small vacuum polarisation effects. However, we do not observe any sign of unquenching here. A reasonable expectation is that these quantities are very sensitive to the details of the NRQCD action. Large systematic errors possibly hide unquenching effects. This is clearly indicated by results presented in the next chapter. It seems likely that the spin-dependent sector will come out correctly only if the coefficients

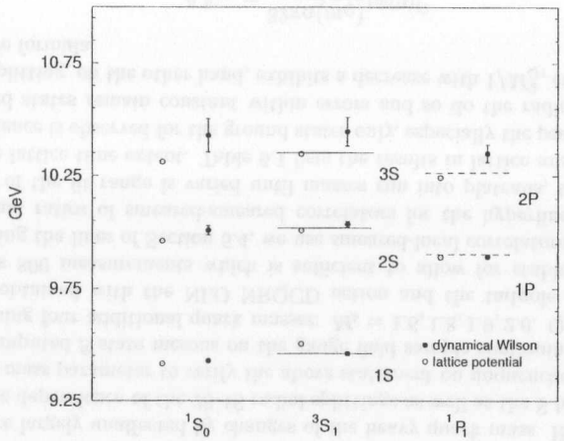

Figure 5.31. *Comparison between the NRQCD results for the $b\bar{b}$ spectrum and the bottomonium energies obtained in Ref. [107] from the $O(v^2)$ corrected lattice heavy quark potential.*

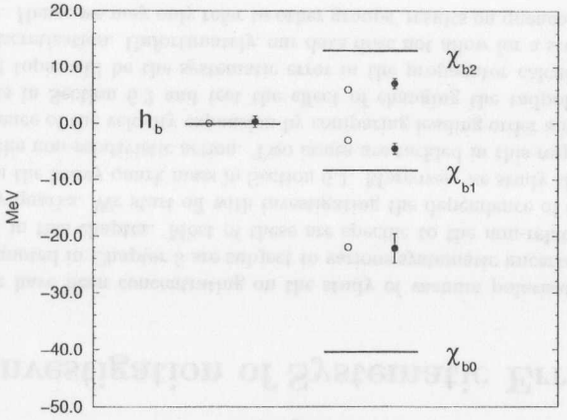

Figure 5.32. *NRQCD results for the P fine structure (filled circles) versus the $O(v^2)$ corrected lattice heavy quark potential (open circles).*

in the action, in particular c_4, are adjusted more accurately.[7]

We have chosen smearing functions that are Schrödinger wave functions calculated from a lattice potential. We conclude this chapter with a comparison of the NRQCD spectrum to the energy eigenvalues belonging to these wave functions as given in Ref. [107]. The authors fix the b-quark mass and the value of the string tension by minimising the squared differences between their potential model predictions and experimental states including all observed bottomonium resonances below the $B\bar{B}$ threshold:

$$\sqrt{\kappa} = 452 \text{ MeV} , \quad m_b = 4.72 \text{ GeV} . \tag{5.21}$$

Here, κ denotes the string tension. Note from Figure 5.31 that radial and orbital splittings from the potential model are somewhat smaller than the NRQCD results, in particular the 2S-1S. If one would freeze the average of the $2^3S_1 - 1^3S_1$ and $1^3\bar{P} - 1^3S_1$ splittings to its experimental value, as we have done in the NRQCD simulation, the potential model would predict larger splittings and the 2P mass would come out to be significantly heavier than experiment, but closer to the NRQCD result [107]. The P fine structure that is obtained from both approaches is in surprisingly good agreement, Figure 5.32.

◇

[7] Work in this direction has recently been started by TROTTIER and LEPAGE [145]. The authors have considered the feasibility to compute operator coefficients from numerical simulations deep in the perturbative region.

Chapter 6

Investigation of Systematic Errors

So far we have been concentrating on the study of vacuum polarisation effects. The results quoted in Chapter 5 are subject to various systematic uncertainties which will be explored in this chapter. Most of these are specific to the non-relativistic treatment of the heavy quarks. We start off with investigating the dependence of quarkonium level splittings on the heavy quark mass in Section 6.1. Moreover, we study their sensitivity to changes of the non-relativistic action. Two issues are tackled in this respect: we examine the convergence of the velocity expansion by comparing leading order and next-to-leading order results in Section 6.2 and test the effect of changing the tadpole factor, Section 6.3. A final topic will be the systematic error in the propagator calculation due to the temporal discretisation. Unfortunately, our data does not allow for a study of the cut-off dependence. Hence we may only refer to other groups' results on quenched configurations to give an idea of the scaling behaviour.

6.1 Dependence on the Heavy Quark Mass

It was shown in Section 5.6, that the bare heavy quark mass $M_b = 1.7$ leads to kinetic Υ masses which are in reasonable agreement with experiment. Remember, we did not tune this parameter, but simply adopted the value adequate in the quenched approximation. In fact, a precise adjustment of M_b is unnecessary because radial and orbital quarkonium splittings are largely unaffected by changes of the heavy quark mass. Here, we explicitly calculate the dependence of the 2S-1S radial splittings as well as the S hyperfine splitting on the bare mass parameter to verify the above statement on unquenched configurations. We have computed S-state mesons on the gauge field sample containing the lightest sea quark choosing four additional quark masses: $M_b = 1.6, 1.8, 1.9, 2.0$. Quark propagators have been obtained with the NLO NRQCD action and the tadpole factor u_0^L. Each set contains 800 measurements which is sufficient to allow for stable two-exponential fits. Following the lines of Section 5.4, we use smeared-local correlators to extract radial splittings and ratios of smeared-smeared correlators for the hyperfine splittings. The lower limit of the fit range is varied until masses run into plateaus, the upper limit is fixed to the lattice time extent. Table 6.1 lists the results in lattice units. A significant M_Q-dependence is observed for the ground states only, especially the pseudoscalar, Figure 6.1. Excited states remain constant within errors and so do the radial splittings. The hyperfine splitting, on the other hand, exhibits a decrease with $1/M_Q^2$, consistent with the perturbative formula

$$\Delta E_{\text{hfs}} = \frac{32\pi\alpha(m_Q)}{9m_Q^2}|\psi(0)|^2 . \tag{6.1}$$

The strong dependence on quark mass shown in Figure 6.2 suggests that it has to be tuned carefully in order to get the spin splittings right. For each bare quark mass we have

M_Q	1.6	1.7	1.8	1.9	2.0
$1\,^3S_1$	0.3577(9)	0.3584(6)	0.3597(8)	0.3600(8)	0.3599(8)
$2\,^3S_1$	0.602(11)	0.590(8)	0.599(10)	0.597(10)	0.594(9)
$2\,^3S_1 - 1\,^3S_1$	0.244(11)	0.232(8)	0.239(10)	0.237(10)	0.234(9)
$1\,^1S_0$	0.3433(8)	0.3448(6)	0.3461(8)	0.3468(8)	0.3470(8)
$2\,^1S_0$	0.598(11)	0.582(10)	0.594(9)	0.592(10)	0.589(9)
$2\,^1S_0 - 1\,^1S_0$	0.255(11)	0.237(10)	0.248(9)	0.245(9)	0.242(9)
$1\,^3S_1 - 1\,^1S_0$	0.01379(23)	0.01346(11)	0.01304(24)	0.01273(24)	0.01244(23)

Table 6.1. *Radial and hyperfine splittings for S states as a function of the bare heavy quark mass. All results are obtained on the sample with the lightest dynamical quark mass, $\kappa = 0.1575$. With exception of column three ($M_Q = 1.7$), fit ranges have been uniformly chosen to be [8,31] for $^1S_0$, $^3S_1$ two-exponential fits and [18,31] for $^3S_1/^1S_0$ ratio fits.*

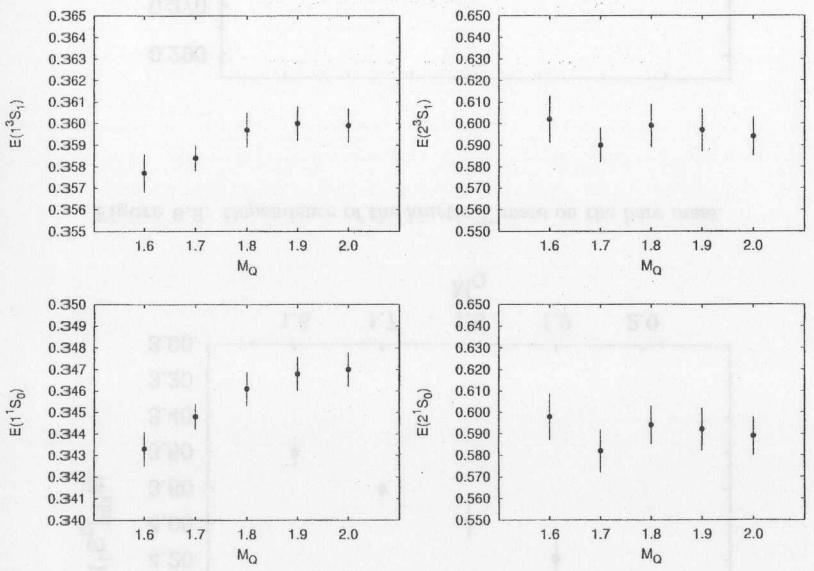

Figure 6.1. *Heavy quark mass dependence of Υ and η_b levels according to Table 6.1. One observes a small increase of ground state energies which is drowned, however, by the error of the excited state when forming mass differences.*

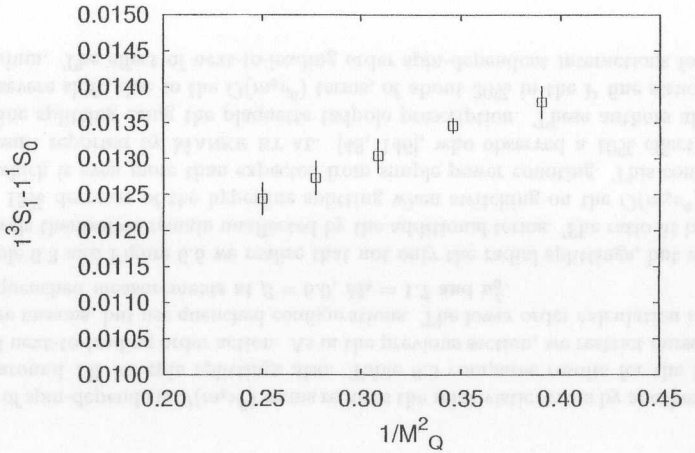

Figure 6.2. *S hyperfine splitting as a function of the inverse bare heavy quark mass.*

M_Q	1.6	1.7	1.8	1.9	2.0
$M_{\rm kin}$	3.60(9)	3.84(5)	3.99(10)	4.19(10)	4.36(8)

Table 6.2. *Results for the Υ kinetic energy for various values of the bare heavy quark mass.*

computed the kinetic Υ mass which is found to vary by 20% over the range $M_Q = 1.6-2.0$, Table 6.2 and Figure 6.3. This causes the 2S-1S splitting to change by less than 10% as can be seen from Figure 6.4 Let us refer back to Figure 5.30 to note that $M_{\rm kin}$ needs to be lowered by at most 2-5% to reproduce the experimental Υ mass exactly. Such a small change will increase the S hyperfine splitting by about 5% whereas the radial S splitting will be affected on the 1-2% level only. For the latter we therefore conclude that the systematic uncertainty due to a slight offset in the kinetic Υ mass is negligible compared to statistical errors.

6.2 Convergence of the Velocity Expansion

A central issue are systematic errors arising from higher order relativistic terms that have been neglected. The velocity expansion is a useful tool only if it converges sufficiently fast so that one is not forced to go beyond next-to-leading order.

Our Lagrangian includes spin-independent interaction terms of $O(m_b v^2)$ and $O(m_b v^4)$. The next order will therefore introduce corrections which are $v^4\times$ kinetic energy, i.e. $\sim 0.01 \times 500$ MeV ~ 5 MeV. This presents a 1% error for radial and orbital splittings. Spin splittings would be affected on a 10% level, however. Naively one expects that the

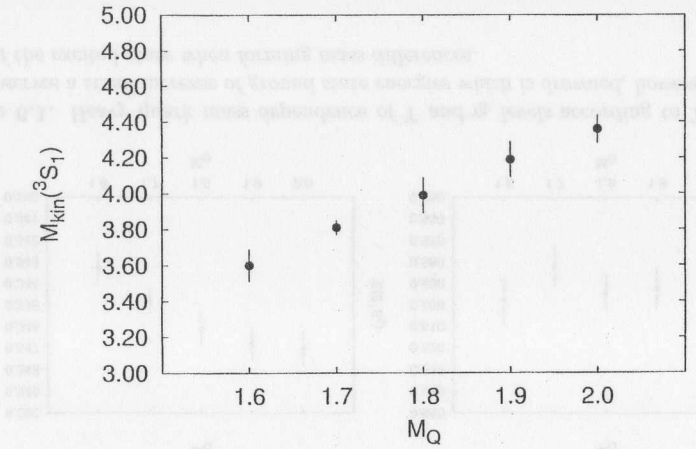

Figure 6.3. *Dependence of the kinetic Υ mass on the bare mass.*

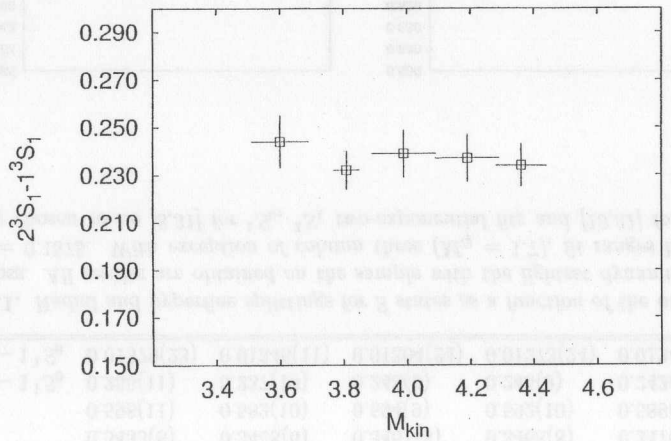

Figure 6.4. *Dependence of $2^3S_1 - 1^3S_1$ radial splitting on the kinetic mass.*

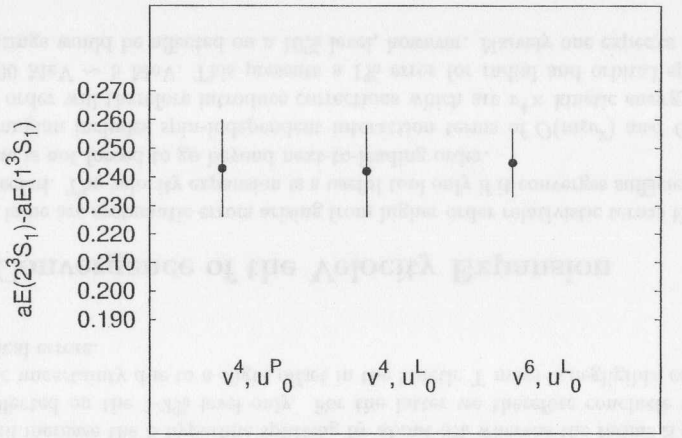

Figure 6.5. *A comparison of the $2^3S_1 - 1^3S_1$ radial splitting for different orders of the NRQCD expansion and different forms of tadpole improvement. Results are for the quenched case at $\beta = 6.0$.*

action	$1\,^1S_0$	$2\,^1S_0$	$1\,^3S_1$	$2\,^3S_1$	$1\,^3S_1 - 1\,^1S_0$
$O(m_b v^4)$	0.3299(6)	0.581(12)	0.3441(7)	0.587(14)	0.01443(23)
$O(m_b v^6)$	0.3309(4)	0.582(12)	0.3438(4)	0.589(12)	0.01266(8)

Table 6.3. *Comparison of quenched Υ and η_b energies obtained with the $O(m_b v^4)$ and $O(m_b v^6)$ actions. Lower order results involve 600 measurements and fit ranges [8,31] for $^3S_1, ^1S_0$ two-exponential fits and [18,31] for $^3S_1/^1S_0$ ratio fits. In both cases simulation parameters are $\beta = 6.0$, $M_b = 1.7$ with tadpole factor u_0^L.*

inclusion of spin-dependent $O(m_b v^6)$ terms reduces the relativistic errors by another factor of v^2 to around 1% for spin splittings also. Table 6.3 compares results for the leading order and next-to-leading order action. As in the previous section, we restrict ourselves to the S-wave mesons, but use quenched configurations. The lower order calculation involves 4×150 quenched measurements at $\beta = 6.0$, $M_b = 1.7$ and u_0^L.

From Table 6.3 and Figure 6.5 we realise that not only the radial splittings, but also the energy levels themselves remain unaffected by the additional terms. The ratio fit however reveals a 15% decrease of the hyperfine splitting when switching on the $O(m_b v^6)$ interactions, which is even more than expected from simple power counting. This confirms a similar result reported by MANKE ET.AL. [48, 146], who observed a 10% effect in the $b\bar{b}$ hyperfine splitting using the plaquette tadpole prescription. These authors also find a rather severe shift, due to the $O(m_b v^6)$ terms, of about 30% in the P fine structure of bottomonium. The effect of next-to-leading order spin-dependent interactions for char-

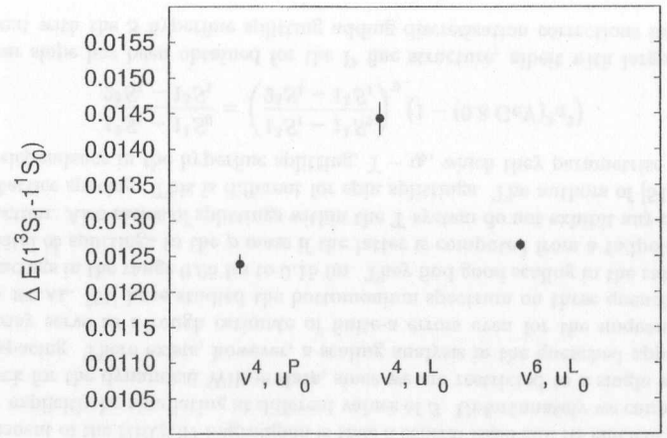

Figure 6.6. *Dependence of the S hyperfine splitting on the order of the NRQCD expansion and the choice of tadpole factor. Compared to the plaquette prescription the splitting increases by about 15% if u_0^L is used. The effect of including spin-dependent $O(m_b v^6)$ terms pushes it down again, surprisingly by the same amount.*

monium has been investigated by TROTTIER [44] and is found to be as large as 60%. All studies therefore come to the conclusion that the first three terms in the velocity expansion for the hyperfine splitting are oscillating in sign with a sizable next-to-leading order contribution. Obviously, the use of an $O(m_b v^6)$-correct action is mandatory to arrive at meaningful results for the spin-splittings in the Υ system.

6.3 Tadpole Scheme Dependence

In addition to the order of the NRQCD expansion, the spin splittings and in particular the S hyperfine splitting will be sensitive to a change of the tadpole renormalisation scheme. One expects them to vary as $1/u_0^4$, since the clover discretisation of the chromomagnetic field contains four link variables. If tadpole improvement is switched off completely ($u_0 = 1$), the spin splittings are badly underestimated by a factor of $\sim 1/2$ [47]. Smaller, but significant changes are expected when different definitions of u_0 are used: the ratio of u_0^4 with the plaquette prescription to that computed from the mean-link in Landau gauge is roughly 10%, see Table 4.2.

To study the influence of u_0 in more detail, we repeat the propagator calculation with the lower-order action ($O(m_b v^4)$) in the quenched approximation choosing this time u_0^P as the tadpole factor. We perform 1400 measurements on S-wave mesons and 600 on P states. Table 6.4 lists the fitted numbers together with results of DAVIES ET.AL. [47] and MANKE ET.AL. [48]. Figure 6.6 confirms the naive expectation that changing u_0

level/splitting	fit result [lattice units]		
	this simulation	Ref. [47]	Ref. [48]
$1\,^1S_0$	0.4418(4)	0.4415(3)	0.4416(3)
$2\,^1S_0$	0.687(13)	0.678(8)	0.679(22)
$1\,^3S_1$	0.4544(5)	0.4537(5)	0.4539(3)
$2\,^3S_1$	0.697(17)	0.686(8)	0.681(20)
$1\,^1P_1$	0.631(9)	0.627(3)	0.635(7)
$2\,^1P_1$	0.839(26)	0.823(14)	
$1\,^3S_1 - 1\,^1S_0$	0.01239(14)	0.01237(14)	0.01227(11)
$1\,^3P_2 - 1\,^3P_0$	0.0159(14)	0.0147(17)	0.0143(34)
$1\,^3P_2 - 1\,^3P_1$	0.0070(10)	0.0078(15)	0.0078(11)
$1\,^3P_1 - 1\,^3P_0$	0.0089(9)	0.0069(12)	0.0070(13)
$1\,^3P_2 - 1\,\bar{P}$	0.0041(5)	0.0042(5)	0.0045(5)
$1\,\bar{P} - 1\,^3P_1$	0.0029(6)	0.0036(8)	0.0036(6)
$1\,\bar{P} - 1\,^3P_0$	0.0118(10)	0.0105(10)	0.0120(17)
$1\,\bar{P} - 1\,^1P_1$	0.0011(5)	0.0008(8)	

Table 6.4. *Simulation results computed with the $O(m_b v^4)$ action and the plaquette tadpole prescription. We compare our results with those of* DAVIES ET.AL. *(third column) and* MANKE ET.AL. *(last column). Each simulation uses quenched configurations at $\beta = 6.0$ and a heavy quark mass of $M_b = 1.7$.*

from u_0^P to the Landau mean-link value affects the hyperfine splitting quite strongly. u_0^L produces an increase of about 15% in the *opposite* direction as adding the higher order relativistic corrections. This result is also found by SHAKESPEARE and TROTTIER [121] who systematically study tadpole renormalisation and relativistic corrections in $c\bar{c}$, $b\bar{c}$ and $b\bar{b}$.

We would like to point out that Table 6.4 also serves as a check of the implementation of the NRQCD code since the results listed have all been obtained on quenched configurations at $\beta = 6.0$ and with the same NRQCD run parameters. We find a remarkable agreement, in particular for the S hyperfine splitting. As we have seen, this quantity is quite sensitive to changes of the action, but can be safely extracted through ratio fits. In addition this comparison explicitly shows that the gauge fixing does not affect the results, since the authors of Ref. [48] do not fix the gauge and apply a completely different smearing technique than we do.

6.4 Stability of the Quark Propagator Solution

The stabilisation parameter in that part of the evolution equation which involves the lowest-order action

$$\left(1 - \frac{aH_0}{2n}\right)^n , \tag{6.2}$$

has been fixed to $n = 2$ so far. This is the minimal choice when using a bare mass of $M_b = 1.7$, Eq. (4.42). Here, we estimate the systematic error due to such a small value

n	1^1S_0	2^1S_0	1^3S_1	2^3S_1	$1^3S_1 - 1^1S_0$
2	0.3448(6)	0.584(8)	0.3584(6)	0.596(8)	0.01345(15)
3	0.3418(9)	0.593(10)	0.3559(9)	0.597(11)	0.01356(25)
5	0.3396(8)	0.591(10)	0.3539(9)	0.595(10)	0.01368(25)

Table 6.5. *Υ and η_b levels for different values of the parameter n on the sample with $\kappa = 0.1575$, 812 measurements. Fit ranges are equally chosen to be [8,31] for ${}^3S_1, {}^1S_0$ two-exponential fits and [18,31] for ${}^3S_1/{}^1S_0$ ratio fits.*

of n. Table 6.5 lists results for two additional values, $n = 3, 5$. They are graphically represented in Figures 6.7 and 6.8.
Ground states are measured accurately enough to exhibit a decrease with n. This is taking place on a scale which is encompassed by the statistical error of the corresponding radial excitation. We thus arrive at a similar statement as in the previous section: for the physically relevant quantities, the mass splittings, no change is observed within errors and the choice of the minimal parameter, $n = 2$ turns out to be adequate. Further evidence for this conclusion comes from the hyperfine splitting. It remains constant within errors of less than 5%.

6.5 Scaling

As discussed in Chapter 4 no continuum extrapolation can be done for Lattice NRQCD. Physical, i.e. continuum results may be obtained at a fixed cut-off if the appropriate operators necessary to achieve a desired accuracy are included into the action. One then has to demonstrate that the spectrum is independent of the lattice spacing within a certain window to prove that the matching to QCD is properly done. For the non-relativistic b-quarks considered here, discretisation errors are likely to be larger than in the light hadron spectrum, although these are not determined by the heavy-quark mass, but by the typical momentum exchanged between the quarks inside the bound state. The improvement of the NRQCD Lagrangian is thus a central issue and its efficiency has to be checked explicitly by simulating at different values of β. Unfortunately we cannot perform this check for the dynamical Wilson data, since we are restricted to a single value of the lattice spacing. There exists, however, a scaling analysis in the quenched approximation which may serve as a rough estimate of finite-a errors even for the unquenched data. DAVIES ET.AL. [51] have studied the bottomonium spectrum on three quenched lattices with spacings in the range 0.05 fm to 0.15 fm. They find good scaling in the ratio of radial and orbital $b\bar{b}$ splittings to the ρ mass if the latter is computed from a tadpole-improved clover action. Also ratios of splittings within the Υ system do not exhibit any dependence on the lattice spacing. This is different for spin splittings. The authors of [51] observe a clear a-dependence in the hyperfine splitting, $\Upsilon - \eta_b$, which they parametrise as

$$\frac{1^3S_1 - 1^1S_0}{2^3S_1 - 1^3S_1} = \left(\frac{1^3S_1 - 1^1S_0}{2^3S_1 - 1^3S_1}\right)_0 \left(1 - (0.8\ \mathrm{GeV})^2 a^2\right) . \qquad (6.3)$$

A similar slope has been obtained for the P fine structure, albeit with large errors. In agreement with the S hyperfine splitting adding discretisation corrections increases the

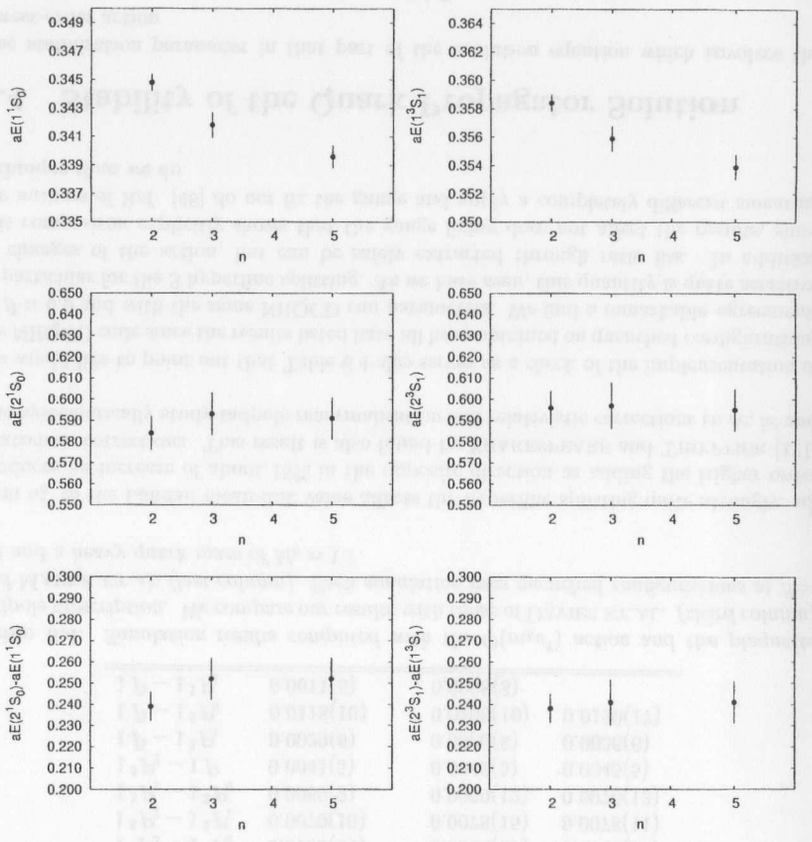

Figure 6.7. *Dependence of Υ and η_b levels on the parameter n.*

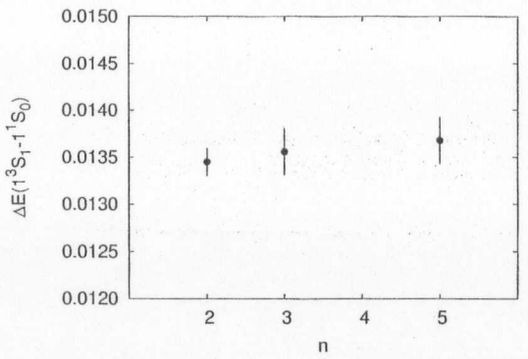

Figure 6.8. *Dependence of the hyperfine splitting on the parameter n.*

splittings and thus acts in the opposite direction to the relativistic corrections.
These results are quite encouraging with respect to the radial and orbital splittings. They also confirm the conclusion that the spin-dependent quantities have to be treated with much greater care. Clearly, dynamical Wilson fermions introduce additional scaling violations, so that we end up with results that are subject to quite different finite-a errors:

- $O(a)$ from dynamical Wilson fermions,
- $O(a^2)$ from the Wilson gauge action,
- $O(a^4)$ from the valence NRQCD quarks.

Eventually, it will be necessary to perform simulations at different lattice spacings to reveal the influence of $O(a)$ errors from the quark part of the action.

6.6 Summary

We have investigated different sources of systematic uncertainties in the calculation of the $b\bar{b}$ spectrum. Tuning the quark mass parameter is common to any lattice QCD approach. In the heavy quark system, however, radial and orbital angular momentum splittings are insensitive to variations in the constituent's mass. This was explicitly checked on the unquenched sample with $\kappa = 0.1575$. We concluded that the error induced by a small offset in the Υ mass is negligible compared to the statistical errors. The hyperfine splitting on the other hand, strongly depends on the b-quark mass, as is anticipated by perturbation theory, and thus requires a precise determination of the kinetic mass. It is plausible that an insufficient tuning of M_b in part explains the inconclusive result for quenching effects in the spin splittings. We have estimated the systematic error arising due to two different choices of the tadpole improvement factor u_0; whereas spin-independent quantities remain unaffected by changes in u_0, the hyperfine splitting increases when using the Landau mean-link prescription. Interestingly, we find this effect to be of the same magnitude as, but of opposite direction to switching on the spin-dependent $O(m_b v^6)$ corrections. Our

results confirm that the next-to-leading order terms in the action are indispensable for calculating the hyperfine splittings. Note, however, that unknown radiative corrections from lower order terms, e.g. $O(\alpha_S)$ contributions to c_4 beyond tadpole improvement can produce effects of the same size as the additional terms, so we do not really perform a complete next-order simulation. As expected, the determination of the lattice spacing a^{-1} (as used, for example, in the analysis of α_S , Chapter 7) remains unaffected by changing tadpole schemes or including $O(m_b v^6)$ terms. Finally, we have studied the accuracy of the propagator evolution with respect to the iteration parameter, n. Though ground states reveal a small decrease with increasing n, the splittings, including the hyperfine splitting, remain unaltered. This justifies the use of $n = 2$ in the simulation.

Chapter 7

The Strong Coupling Constant in Unquenched QCD

The determination of Standard Model parameters presents a major task and challenge for the lattice formulation of QCD. The obvious strategy to compute the strong coupling constant in particular, is to define α_S within a hadronic scheme and evolve it non-perturbatively to high energies. Once the perturbative running of the coupling is identified, one may determine the corresponding Λ parameter and then switch to any other perturbative scheme to calculate scattering processes. This provides a connection between the low-energy regime of hadronic bound states and high-energy jet physics verifying that one and the same theory describes both phenomena. The tools to realise these steps exist and have been applied to the pure gauge sector [147]. But dynamical fermions render the calculations rather expensive so that a treatment of QCD is still lacking.
In this chapter we follow a short-cut to determine the strong coupling constant in QCD based on the spectrum results for $b\bar{b}$ bound states. The method is similar to those employed in determinations of α_S from high-energy processes as it relies on the validity of the perturbative expansion.

7.1 Introduction

The strong need for a precise knowledge of the QCD coupling constant is motivated by the following considerations[148]:
(1) Compared to the electroweak couplings, α and $sin^2\Theta_W$, which have been determined experimentally with a precision of about 0.1%, the strong coupling is presently known only to about 5%. A main limitation on Standard Model tests at LEP for example, is set by the relative inaccuracy of α_s. The same holds for attempts to constrain Grand Unified models from the convergence of the Standard Model couplings at a GUT scale. (2) The determination of α_s from processes which probe perturbative and non-perturbative phenomena yields a fundamental test of QCD. Obviously, such a test is only meaningful if the values of the coupling under consideration are given with similar accuracy. (3) A precise study of the variation of the coupling with momentum over a wide Q^2 range will provide evidence for the QCD β-function and constrain models with additional coloured particles, such as light gluinos.
Most determinations of α_s rely on perturbation theory, where it is common to use the modified minimal subtraction scheme ($\overline{\rm MS}$) of dimensional regularisation. One usually chooses the mass of the Z boson, m_Z, as a reference scale because of the large amount of data that has been taken in e^+e^- annihilation at the Z resonance. However, it has to be remembered that $\alpha_{\overline{\rm MS}}$ is a rather 'unnatural' choice which is only defined operationally in perturbation theory. In many cases the dominant source of uncertainty originates from theoretical systematic errors that are generally difficult to estimate. Extracting α_s

from a perturbative expansion necessarily requires the truncation at a rather low order and thus introduces a significant dependence on the renormalisation scale. It has been demonstrated that this dependence is weakened by an appropriate resummation of the leading and next-to-leading logarithms. But still, one should bear in mind that the nature of the perturbation series is unknown and that the non-perturbative contribution is a priori unclear.
As the formulation of QCD requires a non-perturbative regularisation, it is desirable to define the running coupling non-perturbatively and calculate it in a numerical simulation (reviews are given in [149, 150, 151]). The basic ingredients in such a calculation are:

(a) A non-perturbative definition of a renormalised coupling which can be accurately measured on the lattice and is easily accessible to perturbative calculations.
(b) A precise determination of a reference scale. This is obtained by comparing a computed hadron mass to its experimental value.
(c) An accurate match to perturbation theory and a proper continuum extrapolation.

Two main directions have been followed: the first one actually studies the running of the coupling with momentum; the second estimates $\alpha_{\overline{\rm MS}}$ at relatively low energy and assumes the applicability of perturbative renormalisation group running to evolve the coupling to m_Z.

Direct studies of the running coupling

An intuitive definition of a non-perturbative coupling uses the force $F(r)$, felt by a static quark-antiquark pair at separation r,

$$\alpha_{q\bar{q}}(q) \equiv \frac{1}{C_F} r^2 F(r), \quad q = \frac{1}{r}, \quad C_F = \frac{4}{3}. \tag{7.1}$$

The force is obtained as the derivative of the static potential, $V(r)$ which is calculated from the large-time limit of Wilson loops with spatial extent r. To control perturbative errors when matching to other schemes it is desirable to reach energy scales of order 10 GeV corresponding to very small quark-antiquark separations. Resolving such small distances, on the other hand, requires a small lattice spacing. Finally, the box size L has to be kept big enough to avoid finite volume effects. Therefore one ends up with the following approximate constraints [151]

$$L \gg 1/0.4\ \text{GeV} \gg 1/q \sim 1/10\ \text{GeV} \gg a\,, \tag{7.2}$$

where the string tension is chosen as the confinement scale. (7.2) implies that the number of lattice points in each dimension needs to be much larger than about 25 which is not in reach of present simulations. The interquark force is nevertheless useful to compute the running of the coupling provided one carefully corrects for lattice artefacts. Practically, the $1/r$ ansatz for the static potential stemming from the continuum one-gluon exchange is replaced by the Fourier transform of the lattice gluon propagator. Simulations have been performed in the pure gauge theory. They cover an energy range of a few GeV [152, 153, 102]. Present unquenched lattices are too coarse for this method, however.

A sophisticated approach has been suggested in Refs.[154, 155] where a box-size dependent renormalised coupling is introduced. It is based on the Schrödinger functional which is the partition function on a finite volume with periodic boundary conditions in the spatial directions and Dirichlet boundary conditions in the time direction. The coupling is defined - in a rather exotic way - as the derivative of the free energy of the gauge field in the box with respect to a parameter characterising the (abelian) boundary field[1]. This choice has various practical advantages like small finite-a errors and quark-mass independence. A coupling that runs with the volume allows for a scale variation by several orders of magnitude which is impossible for a single-lattice technique. Furthermore, there is a well-controlled extrapolation to the continuum limit. Once the coupling has been evolved non-perturbatively to high energies, one can safely convert to the $\overline{\rm MS}$ scheme. This technique was first applied to the O(3) σ-model [154] and subsequently to SU(2) gauge theory [158] and SU(3) gauge theory [147]. So far, it has been restricted to the pure gauge sector. Once such simulations become available with dynamical fermions included, they should yield the most accurate lattice results on α_S with an uncertainty below 1%.

Short-cut approach

The above methods have not yet been applied to the unquenched theory. To obtain estimates of $\alpha_{\overline{\rm MS}}$ in QCD one may take a short-cut which defines a renormalised coupling through short distance lattice quantities like small Wilson loops or Creutz ratios [159, 160, 18]. The idea is to measure a physical scale from a quarkonium splitting at a given bare coupling and obtain a value of a suitably defined renormalised coupling at that scale by comparing the measured value of the plaquette, for instance, with its perturbative expansion. This procedure will be applied in the following sections to obtain a value of $\alpha^{(5)}_{\overline{\rm MS}}(m_Z)$ from our simulation with dynamical Wilson fermions.

7.2 The Coupling Constant from the Plaquette

7.2.1 Definition of the Coupling

We determine the coupling by matching the perturbative expansion of the plaquette to the numerical Monte Carlo result as proposed by LEPAGE and MACKENZIE [18]. The 1×1 Wilson loop is the smallest gauge-invariant object in pure lattice gauge theory. Therefore, on the lattice it is expected to be a suitable ultraviolet quantity with negligible non-perturbative contamination. Assuming that the leading non-perturbative contribution is due to the gluon condensate [138],

$$\delta W_{11} = -\frac{\pi a^4}{36}\langle \alpha_S F^2\rangle \approx -9\cdot 10^{-5}\,, \tag{7.3}$$

one estimates a 0.02%-correction to $-\ln W_{11}$ for $\langle \alpha_S F^2\rangle \approx 0.042$ GeV^4 and an inverse lattice spacing of $a^{-1} = 2.5$ GeV. The irrelevance of non-perturbative parts is also

[1] An alternative definition is based on the ratio of correlations of Polyakov loops where the gauge field obeys twisted boundary conditions [156, 157].

supported numerically. The authors of Refs. [50, 49, 138] directly compare the couplings determined from the four smallest Wilson loops. They find complete consistency once the values are evolved to a common scale. In [18] the logarithm of the plaquette is used instead of the plaquette itself, since its expansion is better behaved:

$$-\ln\langle\frac{1}{3}\Re\mathrm{Tr}\Box\rangle = \frac{4\pi}{3}\alpha_V\left(\frac{3.41}{a}\right)\left[1-(1.1870+0.0249\,n_f)\,\alpha_V+O(\alpha_V^2)\right]\,. \tag{7.4}$$

α_V is a physically motivated coupling defined via the static $Q\bar{Q}$-potential [161]

$$\alpha_V(q)\equiv-\frac{1}{4\pi}C_F^{-1}q^2V(q)\,,\qquad C_F=4/3\,. \tag{7.5}$$

The coefficient of n_f here is specific to Wilson fermions. By a slight modification of Eq.(7.4) DAVIES ET.AL. [50] introduced a coupling α_P, which is directly related to the plaquette and coincides with α_V through second order

$$-\ln\langle\frac{1}{3}\Re\mathrm{Tr}\Box\rangle = \frac{4\pi}{3}\alpha_P\left(\frac{3.41}{a}\right)\left[1-(1.1870+0.0249\,n_f)\,\alpha_P\right]\,,\quad \alpha_P(q)=\alpha_V(q)+O(\alpha_V^3)\,. \tag{7.6}$$

It just amounts to a shift of truncation errors in α_V to the conversion into standard couplings later on. The scale $3.41/a$ is the average gluon momentum in the first-order contribution to $-\ln W_{11}$ as described in [162, 18][2] .

7.2.2 Setting the Lattice Scale

An accurate way to fix the lattice spacing is through the Sommer scale, r_0 which is computed from the static potential at intermediate quark-antiquark separations [164]. It is the proper choice when comparing different lattice calculations and – unlike the string tension – also applies to full QCD. However, it is not directly accessible to experiment. Therefore, in the light hadron sector one generally prefers the scale set by the ρ-meson mass, though the ρ is not stable in the presence of dynamical quarks and, more important, the extrapolation to the chiral limit introduces large errors as pointed out in Section 5.4. An alternative choice would be the pion decay constant. Here, an additional systematic uncertainty arises because of the renormalisation factor Z_A.

[2] $q^*=3.41/a$ corresponds to the momentum scale which is characteristic to the plaquette. It is proposed in [18, 163] that for a quantity whose first order contribution has the form

$$\alpha_V(q^*)\int_{-\pi/a}^{\pi/a}d^4q f(q)\,, \tag{7.7}$$

the typical scale should be computed as

$$\ln(q^*)=\frac{\int_{-\pi/a}^{\pi/a}d^4q f(q)\ln(q)}{\int_{-\pi/a}^{\pi/a}d^4q f(q)}\,. \tag{7.8}$$

β	n_f	M_q	$-\ln\langle\frac{1}{3}\Re\mathrm{Tr}\Box\rangle$	$\alpha_P^{(n_f)}(\frac{3.41}{a})$	$\frac{3.41}{a}$ [GeV]	
					$\bar{\chi}-\Upsilon$	$\Upsilon'-\Upsilon$
5.6	2	$M_s/3$	0.5570	0.1677	8.84(44)	8.48(46)
	2	M_l	0.5546	0.1668	9.16(83)	9.09(101)
6.0	0	∞	0.5214	0.1518	9.13(50)	7.82(54)

Table 7.1. *Results for $\alpha_P\,(3.41/a)$ extracted from the measured plaquette value.*

Much better suited are the low-lying onium splittings, especially the 1P-1S and, less accurate, the 2S-1S splittings. In the previous chapters we gave numerical evidence for the phenomenological assumption that they are quite insensitive to the mass of the light quarks and for the empirical observation that they depend very little on the heavy-quark mass.

7.2.3 Numerical Results

In Table 7.1 we summarise the couplings, α_P obtained from Eq.(7.6) as well as the scales determined from the 1P-1S ($\bar{\chi}-S$) and 2S-1S ($\Upsilon'-\Upsilon$) splittings. In the unquenched case we quote values both for $M_q=M_s/3$ and $M_q=M_l$, to expose the systematic effect connected to the finite and degenerate sea-quark mass. Note that the plaquette values have been linearly extrapolated in M_q. We do not quote an error on $-\ln\langle\frac{1}{3}\Re\mathrm{Tr}\Box\rangle$ and $\alpha_P^{(n_f)}(3.41/a)$ in Table 7.1 since it is negligible compared to the uncertainty in the scale. Subsequently these couplings are evolved to a common scale using the universal two-loop β function

$$\alpha(\mu)=\alpha^{(1)}(\mu)+\alpha^{(2)}(\mu)+O(\alpha^3)\,, \tag{7.9}$$

where

$$\alpha^{(1)}(\mu)=\frac{\alpha(\mu_0)}{1+\alpha(\mu_0)\beta_0 t(\mu)}\,,\quad \alpha^{(2)}(\mu)=-\left(\alpha^{(1)}(\mu)\right)^2 b_1\ln\left(\frac{\alpha(\mu_0)}{\alpha^{(1)}(\mu)}\right)\,. \tag{7.10}$$

Here we follow [165] and define

$$t(\mu)\equiv\frac{1}{4\pi}\ln\left(\frac{\mu^2}{\mu_0^2}\right)\,,\quad b_1\equiv\frac{\beta_1}{4\pi\beta_0}\,, \tag{7.11}$$

where the scheme-independent coefficients of the β-function are

$$\beta_0=11-\frac{2}{3}n_f\,,\quad \beta_1=102-\frac{38}{3}n_f\,. \tag{7.12}$$

Choosing $\mu=9.0$ GeV and $\mu_0=3.41/a$ we end up with the numbers listed in Table 7.2. The error in the evolution is negligible as the momentum range is very small. For instance, using just the one-loop evolution results in a deviation much less than 1%.

Splitting	$\alpha_P^{(0)}(9.0\,\mathrm{GeV})$	$\alpha_P^{(2)}(9.0\,\mathrm{GeV})$		$\alpha_P^{(3)}(9.0\,\mathrm{GeV})$	
		$M_q = M_s/3$	$M_q = M_l$	$M_q = M_s/3$	$M_q = M_l$
$\bar{\chi} - \Upsilon$	0.1524(25)	0.1669(24)	0.1676(43)	0.1752(41)	0.1764(74)
$\Upsilon' - \Upsilon$	0.1457(28)	0.1649(25)	0.1672(53)	0.1766(47)	0.1805(97)

Table 7.2. *Plaquette couplings at the reference scale $\mu = 9.0$ GeV. The last two columns are the result of an extrapolation in the flavour number.*

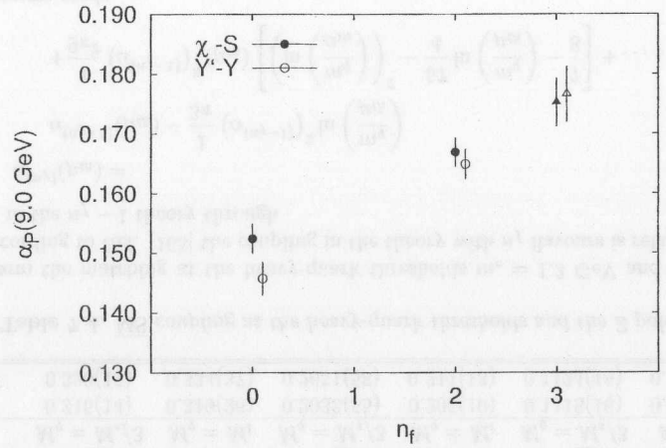

Figure 7.1. *The plaquette coupling α_P as a function of the number of dynamical flavours. Filled circles denote values extracted from the $\bar{\chi} - S$ splitting, open circles are chosen for values extracted from the $\Upsilon' - \Upsilon$ splitting. The triangles result from an extrapolation in the inverse flavour number. Error bars include statistical errors as well as systematic errors stemming from $O(v^4)$ corrections and the tadpole improvement uncertainty.*

7.2.4 Flavour Extrapolation

The plaquette couplings in the quenched and unquenched theory can now be extrapolated to the active number of light quark flavours which is expected to be $n_f = 3$ in the case of the low-lying $b\bar{b}$ bound states. Guided by the perturbative evolution, we extrapolate α_P^{-1} linearly in n_f, rather than α_P itself. The dependence on n_f is plotted in Figure 7.1. Obviously the mismatch between α_P-values obtained from different splittings in the quenched approximation disappears, once the dynamical quarks are switched on. This is a reformulation of our spectrum results in terms of the coupling constant. Note that the possibility of extrapolating in the number of dynamical flavours is quite a progress compared to the earliest lattice determinations of α_S. These were solely based on quenched data and thus yielded results which are 20% smaller than obtained for the 'correct' n_f. This deviation was perturbatively compensated by evolving down to q_Υ (compare Chapter 5), switching to $n_f = 3$ and evolving back to the plaquette energy scale [3]. Corrections obtained this way are as large as 15-20%. Clearly, it would be a further step forward if one actually had simulation results with $n_f > 2$ so that even the extrapolation could be avoided.

7.3 Conversion to the $\overline{\mathrm{MS}}$-Scheme

To make the connection with the $\overline{\mathrm{MS}}$-scheme one invokes

$$\alpha_{\overline{\mathrm{MS}}}^{(n_f)}\left(\mathrm{e}^{-5/6}Q\right) = \alpha_P^{(n_f)}(Q)\left[1 + \frac{2}{\pi}\alpha_P^{(n_f)} + C_2(n_f)\alpha_P^2 + \ldots\right], \tag{7.14}$$

where the scale factor $e^{-5/6}$ is chosen to eliminate the n_f dependence in the second-order coefficient of the expansion [162]. The two-loop coefficient C_2 has been calculated by LÜSCHER and WEISZ in the quenched theory, $C_2 = 0.96$, $n_f = 0$ [166, 167]. Following Ref. [138], we use this value also in the unquenched calculation and take the whole size of the quenched two-loop contribution as an error estimate for the $\alpha_P - \alpha_{\overline{\mathrm{MS}}}$ conversion. The couplings are evolved to the Z mass applying third-order perturbative evolution, i.e. the next order is included in Eq.(7.9),

$$\alpha^{(3)}(\mu) = \left(\alpha^{(1)}(\mu)\right)^3\left[b_1^2\ln\left(\frac{\alpha(\mu_0)}{\alpha^{(1)}(\mu)}\right)\left[\ln\left(\frac{\alpha(\mu_0)}{\alpha^{(1)}(\mu)}\right) - 1\right] - (b_1^2 - b_2)\left(1 - \frac{\alpha(\mu_0)}{\alpha^{(1)}(\mu)}\right)\right], \tag{7.15}$$

with

$$b_2 = \frac{\beta_2}{(4\pi)^2\beta_0}, \quad \beta_2 = \frac{1}{2}\left(2857 - \frac{5033}{9}n_f + \frac{325}{27}n_f^2\right). \tag{7.16}$$

[3] Since we fix the lattice spacing by setting the Υ splittings, which probe momentum scales $q_\Upsilon \sim 0.5 - 1$ GeV, to their correct physical values, the coupling is given its correct value at q_Υ (see [138]):

$$\alpha_P^{(0)}(q_\Upsilon) = \alpha_P^{(2)}(q_\Upsilon) = \alpha_P^{(3)}(q_\Upsilon). \tag{7.13}$$

n_f		$\bar{\chi} - \Upsilon$	$\Upsilon' - \Upsilon$
	μ [GeV]	$\alpha_{\overline{\rm MS}}(\mu)$	$\alpha_{\overline{\rm MS}}(\mu)$
3	3.91	0.1998(53)	0.2016(61)
3	1.30	0.3153(141)	0.3202(165)
4	1.30	0.3150(141)	0.3198(165)
4	4.10	0.2033(55)	0.2051(63)
5	4.10	0.2032(55)	0.2051(63)
5	91.00	0.1118(16)	0.1124(18)

Table 7.3. *Evolution of $\alpha_{\overline{\rm MS}}$ and matching at the heavy-quark thresholds for $M_q = M_s/3$.*

Splitting	$\alpha_{\overline{\rm MS}}(1.3\,{\rm GeV})$		$\alpha_{\overline{\rm MS}}(4.1\,{\rm GeV})$		$\alpha_{\overline{\rm MS}}(91.2\,{\rm GeV})$	
	$M_q = M_s/3$	$M_q = M_l$	$M_q = M_s/3$	$M_q = M_l$	$M_q = M_s/3$	$M_q = M_l$
$\bar{\chi} - \Upsilon$	0.315(14)	0.319(26)	0.2033(55)	0.205(10)	0.1118(16)	0.1123(29)
$\Upsilon' - \Upsilon$	0.320(15)	0.334(37)	0.2051(58)	0.211(13)	0.1124(18)	0.1139(39)

Table 7.4. *$\overline{\rm MS}$ coupling at the heavy-quark thresholds and the Z pole.*

We perform the matching at the heavy-quark thresholds $m_c = 1.3$ GeV and $m_b = 4.1$ GeV. According to Ref. [165] the coupling in the theory with n_f flavours is related to the coupling in the $n_f - 1$ theory through

$$\alpha^{(n_f)}(\mu_{th}) = \alpha^{(n_f-1)}(\mu_{th}) - \frac{1}{3\pi}\left(\alpha^{(n_f-1)}\right)^2 \ln\left(\frac{m_q}{\mu_{th}}\right) + \frac{1}{9\pi^2}\left(\alpha^{(n_f-1)}\right)^3(\mu_{th})\left[\left(\ln\left(\frac{m_q}{\mu_{th}}\right)\right)^2 - \frac{57}{4}\ln\left(\frac{m_q}{\mu_{th}}\right) - \frac{7}{8}\right] + \dots , \quad (7.17)$$

and its inverse reads

$$\alpha^{(n_f-1)}(\mu_{th}) = \alpha^{(n_f)}(\mu_{th}) + \frac{1}{3\pi}\left(\alpha^{(n_f)}\right)^2 \ln\left(\frac{m_q}{\mu_{th}}\right) + \frac{1}{9\pi^2}\left(\alpha^{(n_f)}\right)^3(\mu_{th})\left[\left(\ln\left(\frac{m_q}{\mu_{th}}\right)\right)^2 + \frac{57}{4}\ln\left(\frac{m_q}{\mu_{th}}\right) + \frac{7}{8}\right] + \dots . \quad (7.18)$$

Table 7.3 lists the values of $\alpha_{\overline{\rm MS}}$ (for the data at $M_q = M_s/3$) at the individual steps of the evolution starting at $\mu = {\rm e}^{-5/6} \cdot 9{\rm GeV} \sim 3.91{\rm GeV}$. First, the coupling is evolved down to the charm mass, then one switches to $n_f = 4$ and runs upward again. The final value at the Z scale is quite insensitive to the location of the matching points when third-order evolution is applied. This becomes apparent from Figure 7.2 where we have varied the b-threshold from three to five GeV. A similar result emerges if the charm threshold is changed.

In Table 7.4 we compare the results obtained with $M_q = M_s/3$ and $M_q = M_l$. The difference between central values is taken as an estimate of the error due to the dynamical

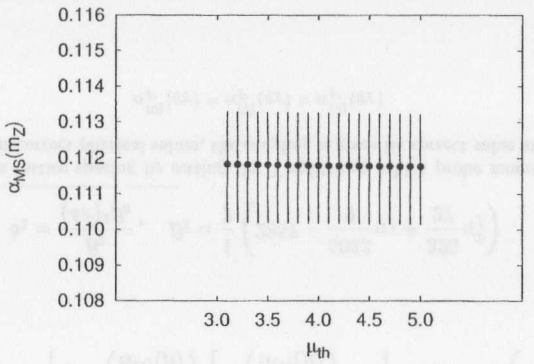

Figure 7.2. *Dependence of $\alpha^{(5)}_{\overline{\rm MS}}(m_Z)$ on the choice of the b-threshold for third-order evolution. Obviously the final result is unaffected within comfortable ranges of the matching point.*

valence quarks	scale	$\alpha^{(5)}_{\overline{\rm MS}}(m_Z)$	reference
NRQCD	$\bar{\chi}_b - \Upsilon$	0.1174(24)	DAVIES ET.AL. [138]
TI Clover	$\bar{\chi}_b - \Upsilon$	0.1159(30)	FNAL/SCRI [139]
Wilson	$\bar{\chi}_c - J/\Psi$	0.111(6)	WINGATE ET.AL. [168]
Wilson	$\bar{\chi}_c - J/\Psi$	0.112(5)	AOKI ET.AL. [169]

Table 7.5. *Previous lattice estimates of $\alpha^{(5)}_{\overline{\rm MS}}(m_Z)$ from the short-cut method, all of which use configurations with $n_f = 2$ staggered fermions.*

quark mass. The largest systematic error is introduced by the unknown n_f dependence of the two-loop coefficient C_2 in the conversion formula (7.14). It produces an uncertainty of ± 0.002 on $\alpha^{(5)}_{\overline{\rm MS}}(m_Z)$. We thus arrive at our final results

$$\alpha^{(5)}_{\overline{\rm MS}}(m_Z) = \begin{cases} 0.1118 & (16)(5)(20) \quad \bar{\chi} - \Upsilon \\ 0.1124 & (18)(15)(20) \quad \Upsilon' - \Upsilon \end{cases} . \quad (7.19)$$

The first error includes the statistical uncertainty and the systematic errors due to the influence of relativistic corrections and changes in u_0 on the lattice scale. The second error quantifies the sea-quark mass dependence and the last one the truncation error in the conversion.

7.4 Discussion

How does our result compare to other lattice estimates? In Figure 7.3 we have collected data from different groups that have applied the same short-cut method to calculate the strong coupling constant, but have determined the lattice scale in different ways. The

corresponding references are listed in Table 7.5. Our analysis closely parallels the calculation by DAVIES ET.AL. [138]. Therefore the first two data points are directly comparable. Both use the 1P-1S and 2S-1S bottomonium splittings calculated in NRQCD to set the scale (in Figure 7.3 only results from 1P-1S are shown since these are more accurate). The NRQCD simulations differ slightly in the choice of action. It has been $O(m_b v^4)$-accurate in Ref.[138] and was tadpole improved with the average plaquette prescription whereas we have included the $O(m_b v^6)$ spin-dependent terms and used u_0 from the link expectation value in Landau gauge. Systematic effects due to higher orders in the velocity expansion and due to u_0 are included in the quoted errors. The most important difference between both simulations is the choice of dynamical fermions. The authors of Ref.[138] used two flavours of staggered quarks whereas SESAM includes Wilson quarks. The configurations with dynamical staggered quarks have been generated by HEMCGC [170]. It is a bit worrying that we cannot confirm the staggered result but obtain a value of $\alpha^{(5)}_{\overline{\rm MS}}(m_Z)$ which is smaller by two standard deviations. There is some controversy about the correct way to determine the lattice scale in an unquenched simulation. Whereas SESAM's strategy is to set a^{-1} in the chiral limit, one may also think of a^{-1} as a function of M_q. A priori it is conceivable that the value of α_P would be larger if it were determined on each ensemble and then extrapolated in m_q. However, as we have pointed out several times, we observe a very mild dependence of the 1P-1S splitting on the quark mass, so that different extrapolation methods do not produce a big effect. Another objection is that it would be inconsistent to apply the perturbative formula valid in the chiral limit to lattice data at a finite, rather large quark mass. A closer comparison reveals that we see a smaller α_P to start with, Figure 7.4. We have evolved our data to $\mu = 8.2$ GeV which is the scale used in Ref.[138]. There is a clear discrepancy at $n_f = 2$ (and consequently at $n_f = 3$) which is somewhat smoothed by the logarithmic evolution to m_Z, so that we end up with a mismatch of two σ instead of three or four. Obviously, the distinct α_P results originate from a difference between staggered and Wilson plaquette values which is larger than expected from perturbation theory, while the scales in both simulations are comparable. Unfortunately, this issue has not yet been resolved.

Recently there has been some progress concerning the neglected n_f dependence in the conversion formula Eq.(7.14). ALLES ET.AL [171] have calculated the expansion of the average plaquette in QCD with Wilson fermions up to third order, albeit for finite quark masses, see Appendix B. A similar result in the chiral limit could be combined with the known two-loop relation between the lattice coupling and the $\overline{\rm MS}$ coupling to reduce the perturbative uncertainty.

The third data point in Figure 7.3 has been taken from Ref.[139]. The author used a result for a^{-1} from the Υ 1P-1S splitting computed by the SCRI group on the same $n_f = 2$ staggered dynamical configurations as in Ref.[138], however with a tadpole improved clover action. The corresponding α_P was then combined with a quenched clover result from the Fermilab group to perform the flavour extrapolation. $\alpha^{(5)}_{\overline{\rm MS}}$ obtained this way is nicely consistent both with the SESAM point and the result by DAVIES ET.AL.. The remaining two measurements are based on charmonium. WINGATE ET.AL. [168] calculated heavy Wilson fermions in a quenched and a dynamical gauge field background. Once more, the staggered configurations of HEMCGC have been used. This result carries significantly larger errors mainly because of rather noisy P-wave data. A similar analysis

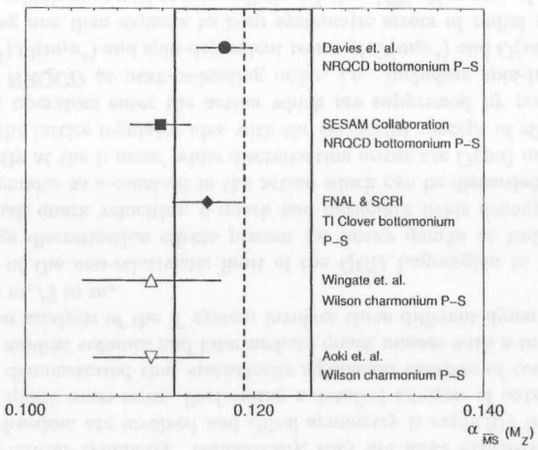

Figure 7.3. *Comparison of results for $\alpha^{(5)}_{\overline{\rm MS}}(m_Z)$ that have been obtained by the same technique, but from different sets of data. Numbers extracted from the bottomonium spectrum have filled symbols, those from charmonium have open symbols. References are given in Table 7.5.*

involving two flavours of dynamical staggered quarks on a somewhat larger lattice and smaller lattice spacing has been performed by AOKI ET.AL. [169]. Both charmonium values are in agreement.

7.5 Summary

We have estimated the strong coupling constant $\alpha^{(5)}_{\overline{\rm MS}}(m_Z)$ from the average plaquette expanded in powers of α_P. The only inputs needed are the measured value of the plaquette and the scale at which α_P is determined. The latter is taken from the bottomonium 1P-1S and 2S-1S splittings. Our result turns out to be somewhat smaller than previous estimates within NRQCD. In particular, α_P computed with configurations including dynamical Wilson quarks differs from the value obtained in the staggered background by approximately three standard deviations leading to a discrepancy in $\alpha^{(5)}_{\overline{\rm MS}}(m_Z)$ of two σ. The problem can be traced back to a deviation between the staggered and Wilson plaquette expectation values which is not balanced by a shift in the lattice scale. Our result for the $\overline{\rm MS}$ coupling is

$$\alpha^{(5)}_{\overline{\rm MS}}(m_Z) = 0.1118(16)(5)(20)\,, \tag{7.20}$$

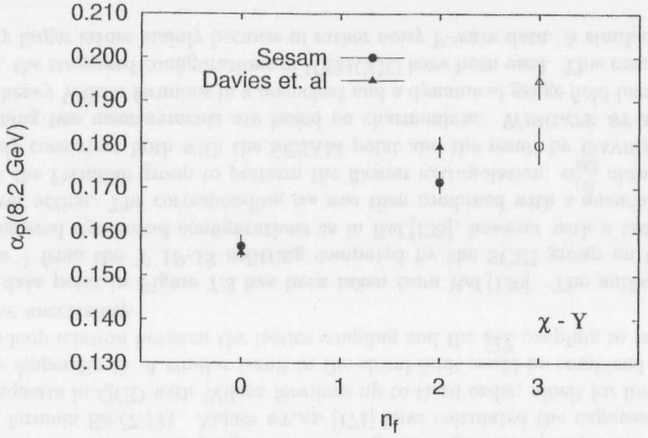

Figure 7.4. *A comparison between α_P extracted from the 1P-1S bottomonium splitting in a dynamical staggered (filled circles) and a dynamical Wilson background (filled triangles).*

where the first error includes the statistical uncertainty and the systematic errors induced by the NRQCD expansion. The second estimates the uncertainty from the sea-quark mass dependence and the final error is due to the truncation of the $\alpha_P - \alpha_{\overline{\rm MS}}$ conversion formula. All lattice calculations prefer values of α_S that are lower than the world average. In particular, the precise $b\bar{b}$ data would clearly exclude a value of 0.122 as obtained from τ decays. We are however not able to make such a statement until the apparent discrepancy between the NRQCD results has been understood.

$\diamond$

Chapter 8

Summary

Wilson's original motivation to formulate QCD on a space-time lattice was to study the confinement phenomenon. Still, the primary goal is to provide a precise test of QCD in the low-energy regime of the strong interaction, with the calculation of hadronic spectra in a prominent place. Lattice simulations aim to quantify the non-perturbative inputs that are necessary for the determination of fundamental Standard Model parameters and thus contribute to the eventual verification or falsification of the theory. In view of the substantial effort which has been invested both in theoretical research and the development of more and more powerful computing facilities during the last 20 years, it is important to point out that progress too has been steady and substantial. It is not too keen to state that the quenched approximation has been solved for those quantities which are easily accessible by the lattice method and that realistic simulations of the full theory are well under way.

In this thesis we have studied $b\bar{b}$ bound states below the B-meson threshold within the framework of Lattice NRQCD beyond the quenched approximation. We briefly outlined the generation of gauge field configurations with dynamical quark content as part of SESAM's program to investigate sea-quark effects in spectral quantities and matrix elements. The project involves a large-scale lattice simulation of Wilson's QCD action for both the gauge part and the fermionic interaction. From a physical viewpoint Wilson fermions represent a more natural discretisation than Kogut-Susskind staggered fermions since they preserve flavour symmetry. Numerically, they are more expensive, however, as more degrees of freedom are involved and chiral symmetry is explicitly broken, even in the absence of a quark mass term. Performing a detailed analysis of autocorrelation times, SESAM has demonstrated that statistically significant samples of configurations can be obtained on modest volumes and intermediate quark masses with a total effort of $O(100)$ Tflopsh. Our analysis of the Υ system involves three different dynamical quark masses in the range $m_s/2$ to m_s.

We have made use of the non-relativistic limit of the QCD Lagrangian to get around the problem of large discretisation effects present for heavy quarks at today's lattice resolutions. For small quark velocities, v quark and antiquark fields decouple and the b-quark mass, m_b remains as a constant in the action which can be discarded. Thus one may simulate 'directly at the b mass' while discretisation errors are $O(\mathrm{p}a)$ only. Lattice NRQCD combines the lattice regulator idea with the successful concept of effective field theories. Irrelevant operators enter the action which are suppressed by powers of v^2. We have employed NRQCD at next-to-leading order, i.e. including spin-independent operators of $O(m_b v^2)$,$O(m_b v^4)$ and spin-dependent terms of $O(m_b v^4)$ and $O(m_b v^6)$. From naive power counting one then expects to keep systematic errors of radial and orbital angular momentum splittings as well as spin splittings below 10%. However, the matching is incomplete. We rely on the recipe of tadpole improvement to account for the bulk of loop contributions and otherwise stick to tree-level couplings. Whereas in lattice simulations of

light quarks one is almost always restricted to the ground-state energy, heavy quarkonia offer the possibility to extract radial and orbital excitations, too, since their wave functions can be estimated quite accurately. We have employed Schrödinger wave functions obtained from a lattice heavy-quark potential to construct meson operators that project on radial and orbital states. Without tuning the smearing functions these operators yielded clean signals.

As an important improvement compared to existing NRQCD simulations we have been able to study the sea-quark mass dependence of bottomonium level splittings and have performed a 'chiral extrapolation' to set the lattice scale at the effective mass of $m_s/3$. We have chosen to use an average a^{-1} from the $2^3S_1 - 1^3S_1$ and $1^3\bar{P} - 1^3S_1$ splittings. These were found to depend very little on the dynamical (light) quark mass. Our strategy in searching for vacuum polarisation effects then has been to compare the extrapolated dynamical results with those of a quenched simulation at nearly equal lattice spacing. Our quenched data for the gross level structure is in clear disagreement with the experimental spectrum which confirms previous studies. Switching on dynamical quarks shifts the data points closer to experiment, so that both splittings, $2^3S_1 - 1^3S_1$ and $1^3\bar{P} - 1^3S_1$ lead to one and the same lattice spacing. The effect is however rather small, so that the statistical accuracy does not suffice to 'measure' the number of active flavours in the sea that enter bottomonium dynamics. On the other hand the 3S and 2P levels hint at three active flavours but they have sizable errors and may be significantly affected by finite volume effects.

Results for spin splittings are somewhat puzzling. Compared to an earlier NRQCD simulation (with staggered dynamical configurations) we have managed to reduce the statistical error on these quantities by more than a factor of two. This permits us to detect very small vacuum polarisation effects. The spin splittings however remain unaffected by the inclusion of dynamical quarks within errors of a few MeV. In particular, the experimentally known P fine structure is largely underestimated for both $n_f = 0$ and $n_f = 2$. A reasonable explanation is that spin splittings are much more sensitive to the details of the NRQCD action so that vacuum polarisation is likely to be covered under sizable systematic errors.

The latter have been investigated in a series of lower-statistics runs. We explicitly checked that radial splittings remain largely untouched by a variation of the bare heavy-quark mass. The S hyperfine splitting, on the other hand, exhibits a strong M_Q dependence. We have estimated the effect of different choices of the tadpole improvement factor u_0. Again there is no visible change in the radial splittings, but the S hyperfine splitting is shown to increase using the Landau mean-link prescription. This increase is nearly compensated by the inclusion of $O(m_b v^6)$ relativistic corrections which have the same magnitude but carry opposite sign.

Based on the spectroscopic results we have given a lattice estimate of the strong coupling constant in full QCD. The determination of α_S utilises the perturbative expansion of the plaquette in the coupling α_P and thus in many ways parallels the procedure applied in high-energy physics. The 'measured' plaquette value is the analogue of some jet cross section or decay rate. The only input from the bottomonium calculation is the lattice scale a^{-1} from either the $1^3\bar{P} - 1^3S_1$ or $2^3S_1 - 1^3S_1$ splitting. We find disparate α_P values from these two splittings in the quenched approximation. They approach each other in the

$n_f = 2$ theory and fully merge after extrapolation to three flavours. Yet our statistics is not high enough to unambiguously determine the number of active flavours that dominate Υ dynamics. The characteristic momentum scale of the plaquette of approximately 9 GeV is considered large enough for perturbation theory to be reliable. Therefore one may safely convert to the $\overline{\text{MS}}$-scheme and evolve to the reference scale m_Z. Our final result is $\alpha^{(5)}_{\overline{\text{MS}}}(m_Z) = 0.1118(26)$.

Appendix A

The Non-Relativistic Lagrangian at Tree Level

We explicitly perform the Foldy-Wouthuysen transformation to decouple the upper and lower components of the Dirac spinor which is natural in a cut-off theory that excludes relativistic Q and $\bar{Q}$ states. The calculation is carried out in *Minkowski space* but the index on gamma matrices will be suppressed: $\gamma^\mu \equiv \gamma^\mu_{(M)}$. We closely follow the notation in [172].

The heavy quark part of the relativistic Lagrangian is

$$\mathcal{L}(x) = \bar{\Psi}_Q \left(i\gamma^\mu D_\mu - m_Q\right) \Psi_Q \tag{A.1}$$

with the covariant derivative defined as $D_\mu \equiv \partial_\mu + igA_\mu$ and $A_\mu = A^B_\mu T^B$. Now we distinguish between *even* operators that do not mix upper and lower spinor components and *odd* operators which do:

$$\mathcal{L} = \Psi^\dagger_Q \left(\mathcal{E} + \mathcal{O} - \gamma^0 m_Q\right) \Psi_Q \,, \tag{A.2}$$

where

$$\mathcal{O} = i\gamma^0\gamma^j D_j \,, \qquad \mathcal{E} = iD_0 \,. \tag{A.3}$$

Now we transform the spinor field with a unitary operator

$$\Psi'_Q = \mathrm{e}^A \Psi_Q \,, \tag{A.4}$$

with $A = -\gamma^0\mathcal{O}/2m_Q$ antihermitian. The Lagrangian becomes

$$\mathcal{L}_Q = \Psi'^\dagger_Q \, \mathrm{e}^A \, K \, \mathrm{e}^{-A} \, \Psi'_Q \equiv \Psi'^\dagger_Q \, K' \, \Psi'_Q \,. \tag{A.5}$$

Here we have introduced the abbreviation $K \equiv \mathcal{E} + \mathcal{O} - \gamma^0 m_Q$. K' can be evaluated using the commutator expansion

$$\mathrm{e}^A K \mathrm{e}^{-A} = \sum_{n=0}^{\infty} \frac{1}{n!} [A, K]_{(n)} \,. \tag{A.6}$$

The commutators $[A, K]_{(n)}$ are recursively defined through:

$$[A, K]_{(0)} = K \,, \qquad [A, K]_{(n)} = [A, [A, K]_{(n-1)}] \,. \tag{A.7}$$

The commutators have the general form

$$[A, K]_{(2i+1)} = (-1)^{i+1} \left[\frac{1}{m_Q^{2i}} \mathcal{O}^{2i+1} + \frac{\gamma^0}{m_Q^{2i+1}} \mathcal{O}^{2i+2} + \frac{\gamma^0}{(2m_Q)^{2i+1}} [\mathcal{O}, \mathcal{E}]_{(2i+1)} \right] \tag{A.8}$$

$$[A, K]_{(2j)} = (-1)^{j} \left[-\frac{\gamma^0}{m_Q^{2j-1}} \mathcal{O}^{2j} + \frac{1}{m_Q^{2j}} \mathcal{O}^{2j+1} + \frac{1}{(2m_Q)^{2j}} [\mathcal{O}, \mathcal{E}]_{(2j)} \right] \tag{A.9}$$

with $i, j = 0, 1, 2, \ldots$. According to the velocity-scaling rules, $[A, K]_{(i)}$ contains terms of order $m_Q v^i$, $m_Q v^{i+1}$ and $m_Q v^{i+2}$. We restrict ourselves to the non-relativistic Lagrangian of order $m_Q v^6$. Therefore we have to include $[A, K]_{(i)}$ for $i = 1, \ldots, 4$, the first two terms in $[A, K]_{(5)}$ and the first term in $[A, K]_{(6)}$:

$$K' \equiv \mathcal{E}' + \mathcal{O}' - \gamma^0 m_Q \tag{A.10}$$

with

$$\begin{aligned}
\mathcal{E}' &= \mathcal{E} - \frac{\gamma^0}{2m_Q}\mathcal{O}^2 - \frac{1}{8m_Q^2}[\mathcal{O}, \mathcal{E}]_{(2)} + \frac{\gamma^0}{8m_Q^3}\mathcal{O}^4 + \frac{1}{384m_Q^4}[\mathcal{O}, \mathcal{E}]_{(4)} \\
&\quad - \frac{\gamma^0}{144m_Q^5}\mathcal{O}^6 + O(m_Q v^8) \qquad (A.11) \\
\mathcal{O}' &= -\frac{\gamma^0}{2m_Q}[\mathcal{O}, \mathcal{E}]_{(1)} - \frac{1}{3m_Q^2}\mathcal{O}^3 + \frac{\gamma^0}{48m_Q^3}[\mathcal{O}, \mathcal{E}]_{(3)} + \frac{1}{30m_Q^4}\mathcal{O}^5 + O(m_Q v^7)\,. \qquad (A.12)
\end{aligned}$$

Now we repeat the transformation, yielding

$$\mathcal{E}'' = \mathcal{E}' - \frac{\gamma^0}{2m_Q}\mathcal{O}'^2 + O(m_Q v^8)\,, \qquad \mathcal{O}'' = -\frac{\gamma^0}{2m_Q}[\mathcal{O}', \mathcal{E}']_{(1)} + O(m_Q v^7)\,. \tag{A.13}$$

In a final step all odd terms up to order $m_Q v^7$ are removed and the Lagrangian then reads

$$\begin{aligned}
\mathcal{L} &= \Psi_Q'''^{\dagger} K''' \Psi_Q''' \\
&\equiv \Psi_Q'''^{\dagger} \left[\mathcal{E}''' + \mathcal{O}''' - \gamma^0 m_Q\right] \Psi_Q''' \\
&= \Psi_Q'''^{\dagger} \left[\mathcal{E}'' - \gamma^0 m_Q + O(m_Q v^7)\right] \Psi_Q''' \qquad (A.14)
\end{aligned}$$

We can now express the operators in $\mathcal{E}''$ in terms of the chromoelectric and chromomagnetic fields. Only those operators are considered that really enter the evolution equation later on. These are spin-independent interaction terms including $O(m_Q v^4)$ and spin-dependent interactions including $O(m_Q v^6)$.

$$\begin{aligned}
\mathcal{O}^2 &= (i\gamma^0\gamma^i D_i)(i\gamma^0\gamma^j D_j) \\
&= -\mathbb{1}_2 \otimes (\delta_{ij} + i\epsilon_{ijk}\sigma_k) D_i D_j \\
&= -\mathbb{1}_2 \otimes \left(\mathbf{D}^2 + i\epsilon_{ijk}\sigma_k (ig\partial_i A_j - g^2 A_i A_j)\right) \\
&\equiv -\mathbb{1}_2 \otimes \left(\mathbf{D}^2 + g\vec{\sigma}\cdot\mathbf{B}\right)\,. \qquad (A.15)
\end{aligned}$$

Here we have defined the B field as

$$\begin{aligned}
B_k &\equiv \epsilon_{kij}\left(-\partial_i A_j - igA_i A_j\right) \\
&= -\frac{1}{2}\epsilon_{kij}\left[\partial_i A_j - \partial_j A_i + igA_i A_j - igA_j A_i\right] \\
&= -\frac{1}{2}\epsilon_{kij} F_{ij} \qquad (A.16)
\end{aligned}$$

$$\begin{aligned}
\mathcal{O}^4 &= (\vec{\alpha}\cdot\mathbf{D})^4 \\
&= \mathbb{1}_2 \otimes \left(\mathbf{D}^2 + g\vec{\sigma}\cdot\mathbf{B}\right)^2 \\
&= \mathbb{1}_2 \otimes \left(\mathbf{D}^4 + g\{\vec{\sigma}\cdot\mathbf{B}, \mathbf{D}^2\} + g^2(\vec{\sigma}\cdot\mathbf{B})^2\right) \qquad (A.17)
\end{aligned}$$

$$\begin{aligned}
[\mathcal{O}, [\mathcal{O}, \mathcal{E}]] &= [i\gamma^0\gamma^i D_i, [i\gamma^0\gamma^j D_j, iD_0]] \\
&= -g\gamma^i\gamma^j D_i F_{j0} + gF_{j0}\gamma^j\gamma^i D_i \\
&= \mathbb{1}_2 \otimes g\left(D_i F_{i0} - F_{i0} D_i\right) + \mathbb{1}_2 \otimes g\left(i\epsilon_{ijk}\sigma_k D_i F_{j0} - F_{j0} i\epsilon_{jik}\sigma_k D_i\right) \\
&= \mathbb{1}_2 \otimes g\left(D_i E_i - E_i D_i\right) + \mathbb{1}_2 \otimes g\left(i\epsilon_{ijk}\sigma_k D_i E_j - E_j i\epsilon_{jik}\sigma_k D_i\right) \\
&= \mathbb{1}_2 \otimes g\left(\mathbf{D}\cdot\mathbf{E} - \mathbf{E}\cdot\mathbf{D}\right) + \mathbb{1}_2 \otimes ig\vec{\sigma}\left(\mathbf{D}\times\mathbf{E} - \mathbf{E}\times\mathbf{D}\right) \qquad (A.18)
\end{aligned}$$

$$\begin{aligned}
[\mathcal{O}, \mathcal{E}]^2 &= g^2\gamma^j\gamma^i F_{j0} F_{i0} \\
&= -\mathbb{1}_2 \otimes g^2\left(E_i E_i + i\epsilon_{jik}\sigma_k E_j E_i\right) \\
&= -\mathbb{1}_2 \otimes g^2\left(\mathbf{E}^2 + i\vec{\sigma}\cdot\mathbf{E}\times\mathbf{E}\right) \qquad (A.19)
\end{aligned}$$

$$\begin{aligned}
\mathcal{O}^6 &= \mathbb{1}_2 \otimes \Big(\left(\mathbf{D}^2\right)^3 + \{\left(\mathbf{D}^2\right)^2, g(\sigma\cdot\mathbf{B})\} + \mathbf{D}^2 g(\sigma\cdot\mathbf{B})\mathbf{D}^2 + \{\mathbf{D}^2, g^2(\sigma\cdot\mathbf{B})^2\} \\
&\quad + g(\sigma\cdot\mathbf{B})\mathbf{D}^2 g(\sigma\cdot\mathbf{B}) + g^3(\sigma\cdot\mathbf{B})^3\Big) \qquad (A.20)
\end{aligned}$$

The chromoelectric field has been defined as

$$E_i \equiv F_{i0}\,. \tag{A.21}$$

We finally arrive at separate Lagrangians for quark and antiquark fields. Defining

$$\Psi_Q''' \equiv \begin{pmatrix} \psi \\ \chi \end{pmatrix}\,, \qquad \mathcal{L} \equiv \mathcal{L}_Q + \mathcal{L}_{\bar{Q}}\,, \tag{A.22}$$

we find

$$\begin{aligned}
\mathcal{L}_Q = \psi^\dagger\Big[&-m_Q \\
&+iD_0 + \frac{1}{2m_Q}\mathbf{D}^2 \\
&+\frac{g}{2m_Q}\vec{\sigma}\cdot\mathbf{B} - \frac{g}{8m_Q^2}\left(\mathbf{D}\cdot\mathbf{E} - \mathbf{E}\cdot\mathbf{D}\right) - \frac{ig}{8m_Q^2}\vec{\sigma}\cdot\left(\mathbf{D}\times\mathbf{E} - \mathbf{E}\times\mathbf{D}\right) + \frac{1}{8m_Q^3}(\mathbf{D}^2)^2 \\
&+\frac{1}{8m_Q^3}\{\mathbf{D}^2, g\vec{\sigma}\cdot\mathbf{B}\} - \frac{ig^2}{8m_Q^3}\vec{\sigma}\cdot(\mathbf{E}\times\mathbf{E}) - \frac{3ig}{64m_Q^4}\{\mathbf{D}^2, \vec{\sigma}\cdot\left(\mathbf{D}\times\mathbf{E} - \mathbf{E}\times\mathbf{D}\right)\} \\
&+ \text{higher orders}\Big]\psi\,, \qquad (A.23)
\end{aligned}$$

and for the antiquark fields

$$\begin{aligned}\mathcal{L}_{\bar{Q}} &= \chi^\dagger [m_Q \\ &+iD_0 - \frac{1}{2m_Q}\mathbf{D}^2 \\ &-\frac{g}{2m_Q}\vec{\sigma}\cdot\mathbf{B} - \frac{g}{8m_Q^2}(\mathbf{D}\cdot\mathbf{E} - \mathbf{E}\cdot\mathbf{D}) - \frac{ig}{8m_Q^2}\vec{\sigma}\cdot(\mathbf{D}\times\mathbf{E} - \mathbf{E}\times\mathbf{D}) - \frac{1}{8m_Q^3}(\mathbf{D}^2)^2 \\ &-\frac{1}{8m_Q^3}\{\mathbf{D}^2, g\vec{\sigma}\cdot\mathbf{B}\} + \frac{ig^2}{8m_Q^3}\vec{\sigma}\cdot(\mathbf{E}\times\mathbf{E}) - \frac{3ig}{64m_Q^4}\{\mathbf{D}^2, \vec{\sigma}\cdot(\mathbf{D}\times\mathbf{E} - \mathbf{E}\times\mathbf{D})\} \\ &+ \text{higher orders}\,]\,\chi\,. \end{aligned} \tag{A.24}$$

The heavy quark mass can now be eliminated from (A.23) and (A.24) by rescaling the quark and antiquark fields, respectively.

◇

Appendix B

Collection of Perturbative Expansions

B.1 Expansion of the average plaquette in the bare lattice coupling

The expansion of the average plaquette up to order g^4 in the bare lattice coupling has been known for a long time. For the pure gauge theory, SU(N), it was computed by DiGiacomo et.al. in Refs. [173, 174]. The calculation of the leading-order fermionic contribution in the chiral limit for Kogut-Susskind and Wilson discretisation were carried out in [175, 176]. Alles et.al. added the third-order coefficient in pure SU(N) [177, 171]. We consider the expansion

$$\langle 1 - \frac{1}{N}\mathrm{ReTr}\Box\rangle = c_1\, g^2 + c_2\, g^4 + c_3\, g^6 + \dots\,, \tag{B.1}$$

and distinguish the pure gauge and fermionic contributions to the coefficients $c_i \equiv c_i^g + c_i^f$:

$$\begin{aligned} c_1^g &= \frac{N^2-1}{8N}\,, \\ c_2^g &= \left(N^2-1\right)\left(w_1 - \frac{1}{128N^2}\right)\,, \\ c_3^g &= \left(N^2-1\right)\left(\frac{w_2}{N^3} - \frac{w_3}{N} + w_4 N\right)\,, \end{aligned} \tag{B.2}$$

with

$$\begin{aligned} w_1 &= 0.0051069297\,, \\ w_2 &= 0.0023152583(50)\,, \\ w_3 &= 0.002265487(17)\,, \\ w_4 &= 0.000794223(19)\,. \end{aligned} \tag{B.3}$$

$$\begin{aligned} c_1^f &= 0\,, \\ c_{2,\mathrm{Wilson}}^f &= -6.92920\cdot 10^{-4}\,\frac{(N^2-1)}{N}\,n_f\,, \\ c_{2,\mathrm{staggered}}^f &= -6.12401\cdot 10^{-4}\,\frac{(N^2-1)}{N}\,n_f\,. \end{aligned} \tag{B.4}$$

For massive Wilson fermions the quark contribution has recently been computed up to third order [171]:

$$\begin{aligned} c_{2,\mathrm{Wilson}}^f &= h_2\,\frac{(N^2-1)}{N}\,n_f\,, \\ c_{3,\mathrm{Wilson}}^f &= (N^2-1)\left(h_{30}n_f + h_{31}\frac{n_f}{N^2} + h_{32}\frac{n_f^2}{N}\right)\,, \end{aligned} \tag{B.5}$$

κ	0.1560	0.1575
$h_2 \times 10^3$	-1.957882(14)	-2.017993(24)
$h_{30} \times 10^3$	-0.256620(43)	-0.270560(43)
$h_{31} \times 10^3$	0.306132(22)	0.322111(22)
$h_{32} \times 10^3$	0.0327854(66)	0.034772(11)

Table B.1. *Parametrisation of c_i^f for Wilson $r = 1$.*

and the constants are listed in Table B.1 for $\kappa = 0.1560$ and $\kappa = 0.1575$.

B.2 Expansion of $-\ln\langle\frac{1}{3}\mathrm{ReTr}\Box\rangle$ in α_V

From (B.1) we obtain

$$-\ln\langle\frac{1}{N}\mathrm{ReTr}\Box\rangle = c_1\,(4\pi\alpha_0) + \left(c_2 + \frac{c_1^2}{2}\right)(4\pi\alpha_0)^2 + \dots\,. \tag{B.6}$$

To arrive at the equivalent expansion in α_V we need to know the perturbative series of the static potential in the bare lattice coupling [178] (we now set $N = 3$).

$$\begin{aligned} V(q) &= \frac{4}{3}\frac{g^2}{q^2}\left[1 + g^2\left(2\beta_0 \ln\left(\frac{\pi}{aq}\right) + d\right)\right] + \dots \\ &\equiv \frac{4}{3}\frac{g_V^2}{q^2}\,, \end{aligned} \tag{B.7}$$

where d has an n_f dependent piece which is different between Wilson and staggered

$$d = 3\left(\frac{31 - 66\ln\pi}{144\pi^2} + p\right) - \frac{1}{24} - n_f\left(\frac{10 - 12\ln\pi}{144\pi^2} + p_4\right)\,, \tag{B.8}$$

$$\begin{aligned} p &= 0.1699956 \\ p_4^{\text{Wilson}} &= 0.0068870 \\ p_4^{\text{staggered}} &= 0.0026248\,. \end{aligned} \tag{B.9}$$

Using Eq.(B.7) we trade g^2 for g_V^2 in Eq.(B.6)and obtain the following expansions

$$\begin{aligned} -\ln\langle\frac{1}{3}\mathrm{ReTr}\Box\rangle &= \frac{4\pi}{3}\alpha_V(\frac{3.41}{a})\left[1 - (1.1870 + 0.0703\,n_f)\,\alpha_V + O(\alpha_V^2)\right] \quad \text{staggered} \\ -\ln\langle\frac{1}{3}\mathrm{ReTr}\Box\rangle &= \frac{4\pi}{3}\alpha_V(\frac{3.41}{a})\left[1 - (1.1870 + 0.0249\,n_f)\,\alpha_V + O(\alpha_V^2)\right] \quad \text{Wilson} \end{aligned} \tag{B.10}$$

B.3 Relation between $\alpha_{\overline{\mathrm{MS}}}$ and the bare lattice coupling in QCD with Wilson fermions

The expansion of $\alpha_{\overline{\mathrm{MS}}}$ in the bare lattice coupling α_0 is known to two loops. It has been calculated by LÜSCHER and WEISZ [167, 166] in pure SU(3) and extended to QCD with Wilson fermions by CHRISTOU ET.AL. [179]:

$$\alpha_{\overline{\mathrm{MS}}}(\mu) = \alpha_0 + d_1\,(a\mu)\,\alpha_0^2 + d_2\,(a\mu)\,\alpha_0^3 \dots \tag{B.11}$$

$$\begin{aligned} d_1\,(a\mu) &= -\frac{1}{2\pi}\left(\frac{11}{3}N - \frac{2}{3}n_f\right)\ln\,(a\mu) - \frac{\pi}{2N} + k_1 N - k_2 n_f \\ &= -\frac{11}{6\pi}N\ln\,(a\mu) - \frac{\pi}{2N} + k_1 N + \left(\frac{1}{3\pi}\ln\,(a\mu) - k_2\right)n_f \\ &\equiv d_1^g\,(a\mu) + d_1^f\,(a\mu) \end{aligned} \tag{B.12}$$

$$\begin{aligned} d_2\,(a\mu) &= d_1^2\,(a\mu) - \frac{1}{24\pi^2}\left[34N^2 - n_f\left(N - \frac{1}{3N}\right)\right]\ln\,(a\mu) \\ &\quad + \frac{3\pi^2}{8N^2} - k_3 + k_4 N^2 - n_f\left[\frac{k_5}{N} - k_6 N\right] \\ &= d_1^{g2}\,(a\mu) - \frac{17}{12\pi^2}N^2\ln\,(a\mu) + \frac{3\pi^2}{8N^2} - k_3 + k_4 N^2 \\ &\quad + 2d_1^g d_1^f + d_1^{f2} + \left[\frac{1}{24\pi^2}\left(N - \frac{1}{3N}\right)\ln\,(a\mu) - \frac{k_5}{N} + k_6 N\right]n_f \\ &\equiv d_2^g + d_2^f \end{aligned} \tag{B.13}$$

In (B.12) we have separated gluonic and fermionic contributions. The numerical result for the constants is

$$\begin{aligned} k_1 &= 2.13573007 \\ k_2 &= 0.08414443(8) \\ k_3 &= 2.8626216 \\ k_4 &= 1.2491158 \\ k_5 &= 0.10924(22) \\ k_6 &= 0.14033(26) \end{aligned} \tag{B.14}$$

Inverting (B.11) we obtain the bare coupling expanded in the renormalised coupling:

$$\alpha_0 = \alpha_{\overline{\mathrm{MS}}}(\mu) - d_1\,(a\mu)\,\alpha_{\overline{\mathrm{MS}}}^2(\mu) + \left(2d_1^2\,(a\mu) - d_2\,(a\mu)\right)\alpha_{\overline{\mathrm{MS}}}^3(\mu) + \dots \tag{B.15}$$

◇

List of Tables

List of Figures

Bibliography

[1] H. D. Politzer. Reliable perturbative results for strong interactions? *Phys. Rev. Lett.*, 30:1346, 1973.

[2] D. J. Gross and F. Wilczek. Ultraviolet behavior of nonabelian gauge theories. *Phys. Rev. Lett.*, 30:1343, 1973.

[3] D. J. Gross and F. Wilczek. Asymptotically free gauge theories. i. *Phys. Rev.*, D8:3633, 1973.

[4] G. 't Hooft. The confinement phenomenon in quantum field theory. In 't Hooft, G. (ed.): Under the spell of the gauge principle 514-546, and in Cargese 1981, Proceedings, Fundamental Interactions 639-671.

[5] S. Mandelstam. *Phys. Rep.*, 23:245, 1976.

[6] H. D. Politzer. Asymptotic freedom: An approach to strong interactions. *Phys. Rept.*, 14:129–180, 1974.

[7] N. Seiberg and E. Witten. Electric - magnetic duality, monopole condensation, and confinement in N=2 supersymmetric Yang-Mills theory. *Nucl. Phys.*, B426:19–52, 1994.

[8] N. Seiberg and E. Witten. Monopoles, duality and chiral symmetry breaking in N=2 supersymmetric QCD. *Nucl. Phys.*, B431:484–550, 1994.

[9] M. A. Shifman, A. I. Vainshtein, and V. I. Zakharov. QCD and resonance physics. Nonperturbative effects in operator expansion. *Nucl. Phys.*, B147:385, 1979.

[10] M. A. Shifman, A. I. Vainshtein, and V. I. Zakharov. QCD and resonance physics. Vector nonet. *Nucl. Phys.*, B147:448, 1979.

[11] M. Shifman. Snapshots of hadrons or the story of how the vacuum medium determines the properties of the classical mesons which are produced, live and die in the QCD vacuum. 1998. hep-ph/9802214.

[12] S. Weinberg. Phenomenological lagrangians. *Physica*, 96A:327, 1979.

[13] J. Gasser and H. Leutwyler. Quark masses. *Phys. Rept.*, 87:77–169, 1982.

[14] H. Leutwyler. How about m (u) = 0? *Nucl. Phys.*, B337:108, 1990.

[15] K. G. Wilson. Confinement of quarks. *Phys. Rev.*, D10:2445–2459, 1974.

[16] M. Peardon. Coarse lattice results for glueballs and hybrids. *Nucl. Phys. Proc. Suppl.*, 63:22, 1998.

[17] C. J. Morningstar and M. Peardon. Efficient glueball simulations on anisotropic lattices. *Phys. Rev.*, D56:4043–4061, 1997.

[18] G. P. Lepage and P. B. Mackenzie. On the viability of lattice perturbation theory. *Phys. Rev.*, D48:2250–2264, 1993.

[19] M. Lüscher, S. Sint, R. Sommer, P. Weisz, and U. Wolff. Nonperturbative O(a) improvement of lattice QCD. *Nucl. Phys.*, B491:323–343, 1997.

[20] T. DeGrand, A. Hasenfratz, P. Hasenfratz, and F. Niedermayer. The classically perfect fixed point action for SU(3) gauge theory. *Nucl. Phys.*, B454:587–614, 1995.

[21] W. Bietenholz and U. J. Wiese. Perfect lattice actions for quarks and gluons. *Nucl. Phys.*, B464:319–352, 1996.

[22] P. Hasenfratz. Prospects for perfect actions. *Nucl. Phys. Proc. Suppl.*, 63:53, 1998.

[23] H. Wittig. Verification of O(a) improvement. *Nucl. Phys. Proc. Suppl.*, 63:47, 1998.

[24] S. Aoki et al. Hadron spectroscopy and static quark potential in full QCD: A comparison of improved actions on the CP-PACS. *Nucl. Phys. Proc. Suppl.*, 63:221, 1998.

[25] M. Talevi. A first taste of dynamical fermions with an O(a) improved action. *Nucl. Phys. Proc. Suppl.*, 63:227, 1998.

[26] K. G. Wilson. Quarks and strings on a lattice. Presented at Erice School of Physics, Erice, Sicily, Jul 11-31, 1975.

[27] H. B. Nielsen and M. Ninomiya. Absence of neutrinos on a lattice. 1. proof by homotopy theory. *Nucl. Phys.*, B185:20, 1981.

[28] F. Butler, H. Chen, J. Sexton, A. Vaccarino, and D. Weingarten. Hadron masses from the valence approximation to lattice QCD. *Nucl. Phys.*, B430:179–228, 1994.

[29] T. Yoshie. Light hadron spectroscopy. *Nucl. Phys. Proc. Suppl.*, 63:3, 1998.

[30] S. Aoki et al. CP-PACS results for quenched QCD spectrum with the Wilson action. *Nucl. Phys. Proc. Suppl.*, 60A:14, 1998.

[31] J. M. Flynn and C. T. Sachrajda. Heavy quark physics from lattice QCD. 1997. hep-lat/9710057.

[32] S. Güsken. Heavy quark physics on the lattice. 1996. hep-ph/9612371.

[33] S. Nussinov and W. Wetzel. Comparison of exclusive decay rates for b $\rightarrow$ u and b $\rightarrow$ c transitions. *Phys. Rev.*, D36:130, 1987.

[34] M. A. Shifman and M. B. Voloshin. On annihilation of mesons built from heavy and light quark and anti-B0 - B0 oscillations. *Sov. J. Nucl. Phys.*, 45:292, 1987.

[35] M. A. Shifman and M. B. Voloshin. On production of D and D^* mesons in B meson decays. *Sov. J. Nucl. Phys.*, 47:511, 1988.

[36] N. Isgur and M. B. Wise. Weak decays of heavy mesons in the static quark approximation. *Phys. Lett.*, B232:113, 1989.

[37] N. Isgur and M. B. Wise. Weak transition form-factors between heavy mesons. *Phys. Lett.*, B237:527, 1990.

[38] H. Georgi. An effective field theory for heavy quarks at low- energies. *Phys. Lett.*, B240:447, 1990.

[39] G. P. Lepage. Simulating heavy quarks. *Nucl. Phys. Proc. Suppl.*, 26:45–56, 1992.

[40] B. Sheikholeslami and R. Wohlert. Improved continuum limit lattice action for QCD with Wilson fermions. *Nucl. Phys.*, B259:572, 1985.

[41] A. X. El-Khadra, A. S. Kronfeld, and P. B. Mackenzie. Massive fermions in lattice gauge theory. *Phys. Rev.*, D55:3933–3957, 1997.

[42] B. A. Thacker and G. Peter Lepage. Heavy quark bound states in lattice QCD. *Phys. Rev.*, D43:196–208, 1991.

[43] G. P. Lepage, L. Magnea, C. Nakhleh, U. Magnea, and K. Hornbostel. Improved nonrelativistic QCD for heavy quark physics. *Phys. Rev.*, D46:4052–4067, 1992.

[44] H. D. Trottier. Quarkonium spin structure in lattice NRQCD. *Phys. Rev.*, D55:6844–6851, 1997.

[45] C. T. H. Davies et al. Precision charmonium spectroscopy from lattice QCD. *Phys. Rev.*, D52:6519–6529, 1995.

[46] S. M. Catterall, F. R. Devlin, I. T. Drummond, R. R. Horgan, and A. D. Simpson. Nonrelativistic QCD for heavy quark systems. *Phys. Lett.*, B300:393–399, 1993.

[47] C. T. H. Davies et al. Precision upsilon spectroscopy from nonrelativistic lattice QCD. *Phys. Rev.*, D50:6963–6977, 1994.

[48] T. Manke, I. T. Drummond, R. R. Horgan, and H. P. Shanahan. Upsilon spectrum from NRQCD with improved action. *Phys. Lett.*, B408:308–314, 1997.

[49] C. T. H. Davies et al. Update on quarkonium spectroscopy and alpha(strong) from NRQCD. *Nucl. Phys. Proc. Suppl.*, 47:409, 1996.

[50] C. T. H. Davies et al. A precise determination of alpha-s from lattice QCD. *Phys. Lett.*, B345:42–48, 1995.

[51] C. T. H. Davies et al. Scaling of the upsilon spectrum in lattice NRQCD. 1998. hep-lat/9802024.

[52] P. Lepage. Perturbative improvement for lattice QCD: An update. *Nucl. Phys. Proc. Suppl.*, 60A:267, 1998.

[53] SESAM Collaboration, U. Glässner, S. Güsken, H. Hoeber, T. Lippert, X.Q. Luo, G. Ritzenhöfer, K. Schilling, and G. Siegert. QCD with dynamical Wilson fermions: First results from SESAM. *Nucl. Phys. Proc. Suppl.*, 47:386, 1996.

[54] SESAM Collaboration, N. Eicker, U. Glässner, S. Güsken, H. Hoeber, T. Lippert, G. Ritzenhöfer, K. Schilling, G. Siegert, A. Spitz, P. Ueberholz, and J. Viehoff. Full QCD with Wilson fermions: Recent results from the SESAM collaboration. 1996. hep-ph/9611464.

[55] T. Lippert et al. SESAM and $T_\chi L$ results for Wilson action: A status report. *Nucl. Phys. Proc. Suppl.*, 60A:311, 1998.

[56] R. Gupta et al. QCD with dynamical Wilson fermions. *Phys. Rev.*, D40:2072, 1989.

[57] R. Gupta et al. QCD with dynamical Wilson fermions. 2. *Phys. Rev.*, D44:3272–3292, 1991.

[58] G. Ritzenhöfer. Flavour singlet operators: A first calculation of quark-loop insertions in full QCD. *Ph.D. thesis*, Bergische Universität, WUB-DIS 96-12, 1997.

[59] C. Davies. The heavy hadron spectrum. *Springer Lecture Notes in Physics*, 512:1–64, 1998. Proceedings of the 36. Internationale Universitätswochen fuer Kern- und Teilchenphysik, Schladming 1997.

[60] SESAM Collaboration, N. Eicker, J. Fingberg, S. Güsken, H. Hoeber, T. Lippert, K. Schilling, A. Spitz, and J. Viehoff. Improved upsilon spectrum with dynamical Wilson fermions. *Phys. Rev.*, D57:4080–4090, 1997.

[61] SESAM Collaboration, A. Spitz, et al. Bottomonium from NRQCD with dynamical Wilson fermions. *Nucl. Phys. Proc. Suppl.*, 63:317, 1998.

[62] S. Güsken. Dynamical quark effects in QCD. *Nucl. Phys. Proc. Suppl.*, 63:16, 1998.

[63] SESAM Collaboration, A. Spitz, et al. An unquenched estimate of α_s. to appear in the proceedings of the International Symposium on Lattice Field Theory 1998, Boulder CO.

[64] M. Creutz. *Quarks, Gluons and Lattices.* Cambridge University Press, Cambridge, 1983.

[65] H. J. Rothe. *Lattice Gauge Theories: an Introduction.* World Scientific, Singapore, 1992.

[66] I. Montvay and G. Münster. *Quantum Fields on a Lattice.* Cambridge University Press, Cambridge, 1994.

[67] S. R. Sharpe. Phenomenology from the lattice. 1994. Lectures given at Theoretical Advanced Study Institute in Elementary Particle Physics (TASI 94): CP Violation and the limits of the Standard Model, Boulder, CO, 29 May - 24 Jun 1994.

[68] R. Gupta. Introduction to lattice QCD: Course. 1997. Lectures given at Les Houches Summer School in Theoretical Physics, Session 68: Probing the Standard Model of Particle Interactions, Les Houches, France, 28 Jul - 5 Sep 1997.

[69] U. Glässner. Das leichte Spektrum der Quantenchromodynamik mit dynamischen Wilson-Fermionen. *Ph.D. thesis*, Bergische Universität, WUB-DIS 97-3, 1997.

[70] X.-Q. Luo, S.-H. Guo, H. Kröger, and D. Schütte. Improving the lattice QCD Hamiltonian. *Nucl. Phys. Proc. Suppl.*, 63:931–933, 1998.

[71] X.-Q. Luo, S.-H. Guo, H. Kröger, and D. Schütte. Improved lattice gauge field Hamiltonian. 1998. hep-lat/9804029.

[72] D. Schütte, A. Wichmann, and C. Weichmann. Application of the coupled cluster method to a Hamiltonian lattice field theory. 1998. hep-lat/9805011.

[73] D. Schütte, A. Spitz, and V. Zota. Exp S Methods and Lattice QCD with Fermions. *Nucl. Phys. Proc. Suppl. B*, 42:832–834, 1995.

[74] K. Osterwalder and R. Schrader. Axioms for euclidean Green's functions. *Commun. Math. Phys.*, 31:83–112, 1973.

[75] K. Osterwalder and R. Schrader. Axioms for euclidean Green's functions. 2. *Commun. Math. Phys.*, 42:281, 1975.

[76] S. Duane, A. D. Kennedy, B. J. Pendleton, and D. Roweth. Hybrid Monte Carlo. *Phys. Lett.*, B195:216, 1987.

[77] SESAM, $T_\chi L$ Collaborations, T. Lippert, et al. Critical dynamics of the Hybrid Monte Carlo algorithm. *Nucl. Phys. Proc. Suppl.*, 63:946, 1998.

[78] T. A. DeGrand and P. Rossi. Conditioning techniques for dynamical fermions. *Comput. Phys. Commun.*, 60:211, 1990.

[79] S. Fischer et al. A parallel SSOR preconditioner for lattice QCD. *Comp. Phys. Commun.*, 98:20–34, 1996.

[80] S. Fischer et al. A parallel SSOR preconditioner for lattice QCD. *Nucl. Phys. Proc. Suppl.*, 53:990–992, 1997.

[81] R. C. Brower, T. Ivanenko, A. R. Levi, and K. N. Orginos. Chronological inversion method for the Dirac matrix in Hybrid Monte Carlo. *Nucl. Phys.*, B484:353–374, 1997.

[82] P. B. Mackenzie. An improved Hybrid Monte Carlo method. *Phys. Lett.*, B226:369, 1989.

[83] SESAM Collaboration, U. Glässner, S. Güsken, H. Hoeber, T. Lippert, G. Ritzenhöfer, K. Schilling, G. Siegert, A. Spitz, and A. Wachter. First evidence of N(f) dependence in the QCD interquark potential. *Phys. Lett.*, B383:98–104, 1996.

[84] O. Philipsen and H. Wittig. String breaking in nonabelian gauge theories with fundamental matter fields. 1998. hep-lat/9807020.

[85] F. Knechtli and R. Sommer. String breaking in SU(2) gauge theory with scalar matter fields. 1998. hep-lat/9807022.

[86] H. Leutwyler. The ratios of the light quark masses. *Phys. Lett.*, B378:313–318, 1996.

[87] J. Bijnens, J. Prades, and E. de Rafael. Light quark masses in QCD. *Phys. Lett.*, B348:226–238, 1995.

[88] J. J. Aubert et al. Experimental observation of a heavy particle J. *Phys. Rev. Lett.*, 33:1404, 1974.

[89] J. E. Augustin et al. Discovery of a narrow resonance in e+ e- annihilation. *Phys. Rev. Lett.*, 33:1406–1408, 1974.

[90] S. W. Herb et al. Observation of a dimuon resonance at 9.5-GeV in 400-GeV proton - nucleus collisions. *Phys. Rev. Lett.*, 39:252, 1977.

[91] T. Appelquist and H. D. Politzer. Heavy quarks and e+ e- annihilation. In Lichtenberg, D. B. (Ed.), Rosen, S. P. (Ed.): Developments In The Quark Theory Of Hadrons, Vol. 1, 352- 354. (Phys. Rev. Lett. 34 (1975) 43-45).

[92] C. Quigg. Top-ology. *Phys. Today*, 50:20, 1997.

[93] E. Braaten. Introduction to the NRQCD factorization approach to heavy quarkonium. 1996. hep-ph/9702225.

[94] M. Beneke. Nonrelativistic effective theory for quarkonium production in hadron collisions. 1997. hep-ph/9703429.

[95] E. Eichten et al. The spectrum of charmonium. *Phys. Rev. Lett.*, 34:369–372, 1975.

[96] J. L. Richardson. The heavy quark potential and the upsilon, J / ψ systems. *Phys. Lett.*, 82B:272, 1979.

[97] A. Martin. A fit of upsilon and charmonium spectra. *Phys. Lett.*, 93B:338, 1980.

[98] W. Buchmuller and S. H. H. Tye. Quarkonia and quantum chromodynamics. *Phys. Rev.*, D24:132, 1981.

[99] C. Quigg and J. L. Rosner. Quarkonium level spacings. *Phys. Lett.*, 71B:153, 1977.

[100] C. Quigg. Realizing the potential of quarkonium. 1997. hep-ph/9707493.

[101] G. S. Bali and K. Schilling. Static quark - anti-quark potential: Scaling behavior and finite size effects in SU(3) lattice gauge theory. *Phys. Rev.*, D46:2636–2646, 1992.

[102] G. S. Bali and K. Schilling. Running coupling and the lambda parameter from SU(3) lattice simulations. *Phys. Rev.*, D47:661–672, 1993.

[103] E. Eichten and F. Feinberg. Spin dependent forces in QCD. *Phys. Rev.*, D23:2724, 1981.

[104] C. Michael and P. E. L. Rakow. Spin dependence of interquark forces from lattice gauge theory. *Nucl. Phys.*, B256:640, 1985.

[105] P. de Forcrand and J. D. Stack. Spin dependent potentials in SU(3) lattice gauge theory. *Phys. Rev. Lett.*, 55:1254, 1985.

[106] G. S. Bali, K. Schilling, and A. Wachter. Ab initio calculation of relativistic corrections to the static interquark potential. 1: SU(2) gauge theory. *Phys. Rev.*, D55:5309–5324, 1997.

[107] G. S. Bali, K. Schilling, and A. Wachter. Complete O(v**2) corrections to the static interquark potential from SU(3) gauge theory. *Phys. Rev.*, D56:2566–2589, 1997.

[108] L. L. Foldy and S. A. Wouthuysen. On the Dirac theory of spin 1/2 particle and its nonrelativistic limit. *Phys. Rev.*, 78:29–36, 1950.

[109] W. E. Caswell and G. P. Lepage. Effective lagrangians for bound state problems in QED, QCD, and other field theories. *Phys. Lett.*, 167B:437, 1986.

[110] G. T. Bodwin, E. Braaten, and G. P. Lepage. Rigorous QCD analysis of inclusive annihilation and production of heavy quarkonium. *Phys. Rev.*, D51:1125–1171, 1995.

[111] A. Wachter. Eine genaue Bestimmung relativistischer Korrekturen zum zentralen $q\bar{q}$-Potential in der SU(3)-Eichtheorie. *Ph.D. thesis*, Bergische Universität, WUB-DIS 96-21, 1996.

[112] A. Barchielli, E. Montaldi, and G. M. Prosperi. On a systematic derivation of the quark - anti-quark potential. *Nucl. Phys.*, B296:625, 1988.

[113] A. Barchielli, N. Brambilla, and G. M. Prosperi. Relativistic corrections to the quark - anti-quark potential and the quarkonium spectrum. *Nuovo Cim.*, 103A:59, 1990.

[114] S. Güsken. *Ph.D. thesis*, Bergische Universität, WUB-DIS 89-7, 1989.

[115] C. Alexandrou, S. Gusken, F. Jegerlehner, K. Schilling, and R. Sommer. The static approximation of heavy - light quark systems: A systematic lattice study. *Nucl. Phys.*, B414:815, 1994.

[116] P. de Forcrand and R. Gupta. *Nucl. Phys. Proc. Suppl. B*, 9:516, 1989.

[117] H. Suman and K. Schilling. First lattice study of ghost propagators in SU(2) and SU(3) gauge theories. *Phys. Lett.*, B373:314–318, 1996.

[118] H. Suman and K. Schilling. A comparative study of gauge fixing procedures on the Connection Machines CM2 and CM5. 1993. hep-lat/9306018.

[119] G. Parisi. Recent progresses in gauge theories. Presented at 20th Int. Conf. on High Energy Physics, Madison, Wis., Jul 17-23, 1980.

[120] G. P. Lepage. Redesigning lattice QCD. 1996. Proceedings of the 35. Internationale Universitätswochen fuer Kern- und Teilchenphysik, Schladming. hep-lat/9607076.

[121] N. H. Shakespeare and H. D. Trottier. Tadpole renormalization and relativistic corrections in lattice NRQCD. 1998. hep-lat/9802038.

[122] C. T. H. Davies. New results on heavy hadron spectroscopy with NRQCD. *Nucl. Phys. Proc. Suppl.*, 63:320, 1998.

[123] C. J. Morningstar. The heavy quark selfenergy in nonrelativistic lattice QCD. *Phys. Rev.*, D48:2265–2278, 1993.

[124] SESAM Collaboration, N. Eicker, U. Glässner, S. Güsken, H. Hoeber, P. Lacock, T. Lippert, G. Ritzenhöfer, K. Schilling, A. Spitz, T. Struckmann, P. Ueberholz, and J. Viehoff. Light and strange hadron spectroscopy with dynamical Wilson fermions. 1998. hep-lat/9806027.

[125] SESAM Collaboration, T. Lippert, et al. Full QCD with dynamical Wilson fermions on a 24**3 x 40 lattice: A feasibility study. 1996.

[126] F. R. Brown and T. J. Woch. Overrelaxed heat bath and Metropolis algorithms for accelerating pure gauge Monte Carlo calculations. *Phys. Rev. Lett.*, 58:2394, 1987.

[127] R. Gupta, G. W. Kilcup, A. Patel, S. R. Sharpe, and P. de Forcrand. Comparison of update algorithms for pure gauge SU(3). *Mod. Phys. Lett.*, A3:1367, 1988.

[128] M. Creutz. Overrelaxation and Monte Carlo simulation. *Phys. Rev.*, D36:515, 1987.

[129] N. Cabibbo and E. Marinari. A new method for updating SU(N) matrices in computer simulations of gauge theories. *Phys. Lett.*, 119B:387, 1982.

[130] G. P. Lepage. The analysis of algorithms for lattice field theory. Invited lectures given at TASI'89 Summer School, Boulder, CO, Jun 4-30, 1989.

[131] W. H. Press et al. *Numerical Recipes in C.* Cambridge University Press, second edition, 1992.

[132] C. Michael. Fitting correlated data. *Phys. Rev.*, D49:2616–2619, 1994.

[133] C. Michael and A. McKerrell. Fitting correlated hadron mass spectrum data. *Phys. Rev.*, D51:3745–3750, 1995.

[134] B. Efron. *Ann. Stat..*, 7:1, 1979.

[135] B. Efron. The jackknife, the bootstrap and other resampling plans. *SIAM*, 1982.

[136] C. Davies. private communication. 1998.

[137] B. Grinstein and I. Z. Rothstein. Errors in lattice extractions of alpha-s due to use of unphysical pion masses. *Phys. Lett.*, B385:265, 1996.

[138] C. T. H. Davies et al. Further precise determinations of alpha-s from lattice QCD. *Phys. Rev.*, D56:2755–2765, 1997.

[139] J. Shigemitsu. Quarkonium physics and alpha-strong from quarkonia. *Nucl. Phys. Proc. Suppl.*, 53:16–22, 1997.

[140] SESAM Collaboration, N. Eicker, U. Glässner, S. Güsken, H. Hoeber, P. Lacock, T. Lippert, G. Ritzenhöfer, K. Schilling, G. Siegert, A. Spitz, P. Ueberholz, and J. Viehoff. Light quark masses with dynamical Wilson fermions. *Phys. Lett.*, B407:290–296, 1997.

[141] SESAM Collaboration, H. Hoeber, et al. Light and strange quark masses with dynamical Wilson fermions. *Nucl. Phys. Proc. Suppl.*, 64:238, 1998.

[142] SESAM Collaboration, H. Hoeber, et al. Light quark physics with dynamical Wilson fermions. *Nucl. Phys. Proc. Suppl.*, 63:218, 1998.

[143] $T_\chi L$ Collaboration, L. Conti, , L. Giusti, U. Glässner, S. Güsken, H. Hoeber, P. Lacock, T. Lippert, G. Martinelli, F. Rapuano, G. Ritzenhöfer, K. Schilling, A. Spitz, T. Struckmann, P. Ueberholz, and J. Viehoff. In preparation.

[144] Particle Data Group. *Phys. Rev.*, D50, 1994.

[145] H. D. Trottier and G. P. Lepage. Perturbative coefficients for improved actions by monte carlo at large beta. *Nucl. Phys. Proc. Suppl.*, 63:865, 1998.

[146] T. Manke, I. T. Drummond, R. R. Horgan, and H. P. Shanahan. Hybrid quarkonia with high statistics from NRQCD. *Nucl. Phys. Proc. Suppl.*, 63:332, 1998.

[147] M. Lüscher, R. Sommer, P. Weisz, and U. Wolff. A precise determination of the running coupling in the SU(3) Yang-Mills theory. *Nucl. Phys.*, B413:481–502, 1994.

[148] P. N. Burrows et al. Prospects for the precision measurement of alpha-s. 1996. hep-ex/9612012.

[149] C. Michael. The QCD spectrum. *Nucl. Phys. Proc. Suppl.*, 42:147, 1995.

[150] P. Weisz. Lattice investigations of the running coupling. 1995. hep-lat/9511017.

[151] R. Sommer. Nonperturbative renormalization of QCD. *Springer Lecture Notes in Physics*, 512:65–114, 1998. Proceedings of the 36. Internationale Universitätswochen fuer Kern- und Teilchenphysik, Schladming 1997.

[152] C. Michael. The running coupling from lattice gauge theory. *Phys. Lett.*, B283:103–106, 1992.

[153] S. P. Booth et al. The running coupling from SU(3) lattice gauge theory. *Phys. Lett.*, B294:385–390, 1992.

[154] M. Lüscher, P. Weisz, and U. Wolff. A numerical method to compute the running coupling in asymptotically free theories. *Nucl. Phys.*, B359:221–243, 1991.

[155] M. Lüscher, R. Narayanan, P. Weisz, and U. Wolff. The Schrödinger functional: A renormalizable probe for nonabelian gauge theories. *Nucl. Phys.*, B384:168–228, 1992.

[156] G. M. de Divitiis, R. Frezzotti, M. Guagnelli, and R. Petronzio. A definition of the running coupling constant in a twisted SU(2) lattice gauge theory. *Nucl. Phys.*, B422:382–396, 1994.

[157] G. M. de Divitiis, R. Frezzotti, M. Guagnelli, and R. Petronzio. Nonperturbative determination of the running coupling constant in quenched SU(2). *Nucl. Phys.*, B433:390–402, 1995.

[158] M. Lüscher, R. Sommer, U. Wolff, and P. Weisz. Computation of the running coupling in the SU(2) Yang-Mills theory. *Nucl. Phys.*, B389:247–264, 1993.

[159] A. X. El-Khadra, G. Hockney, A. S. Kronfeld, and P. B. Mackenzie. A determination of the strong coupling constant from the charmonium spectrum. *Phys. Rev. Lett.*, 69:729–732, 1992.

[160] A. X. El-Khadra, G. M. Hockney, A. S. Kronfeld, and P. B. Mackenzie. Determining alpha-s using lattice gauge theory. Presented at 26th International Conference on High Energy Physics (ICHEP 92), Dallas, TX, 6-12 Aug 1992.

[161] L. Susskind. Coarse grained quantum chromodynamics. 1977. in R. Balian and C. H. LLewellyn Smith (eds.), *Weak and electromagnetic interactions at high energy*, Proceedings of the Les Houches Summer School.

[162] S. J. Brodsky, G. P. Lepage, and P. B. Mackenzie. On the elimination of scale ambiguities in perturbative quantum chromodynamics. *Phys. Rev.*, D28:228, 1983.

[163] G. P. Lepage. Lattice QCD for small computers. 1994. hep-lat/9403018.

[164] R. Sommer. A new way to set the energy scale in lattice gauge theories and its applications to the static force and alpha-s in SU(2) Yang-Mills theory. *Nucl. Phys.*, B411:839, 1994.

[165] G. Rodrigo and A. Santamaria. QCD matching conditions at thresholds. *Phys. Lett.*, B313:441–446, 1993.

[166] M. Lüscher and P. Weisz. Two loop relation between the bare lattice coupling and the $\overline{MS}$ coupling in pure SU(N) gauge theories. *Phys. Lett.*, B349:165–169, 1995.

[167] M. Lüscher and P. Weisz. Computation of the relation between the bare lattice coupling and the $\overline{MS}$ coupling in SU(N) gauge theories to two loops. *Nucl. Phys.*, B452:234–260, 1995.

[168] M. Wingate, T. DeGrand, S. Collins, and U. M. Heller. From spectroscopy to the strong coupling constant with heavy Wilson quarks. *Phys. Rev.*, D52:307–319, 1995.

[169] S. Aoki et al. Manifestation of sea quark effects in the strong coupling constant in lattice QCD. *Phys. Rev. Lett.*, 74:22–25, 1995.

[170] K. M. Bitar et al. QCD hadron spectroscopy with staggered dynamical quarks at beta = 5.6. *Nucl. Phys. Proc. Suppl.*, 26:259–261, 1992.

[171] B. Alles, A. Feo, and H. Panagopoulos. Asymptotic scaling corrections in QCD with Wilson fermions from the three loop average plaquette. *Phys. Lett.*, B426:361–366, 1998.

[172] J. D. Bjorken and S. D. Drell. *Relativistic Quantum Mechanics.* McGraw-Hill, New York, 1964.

[173] A. Di Giacomo and G. C. Rossi. Extracting the vacuum expectation value of the quantity alpha / pi g g from gauge theories on a lattice. *Phys. Lett.*, 100B:481, 1981.

[174] A. Di Giacomo and G. Paffuti. Precise determination of vacuum expectation value of alpha x g**2 / pi from lattice gauge theories. *Phys. Lett.*, 108B:327, 1982.

[175] U. Heller and F. Karsch. Finite temperature SU(2) lattice gauge theory with dynamical fermions. *Nucl. Phys.*, B258:29, 1985.

[176] H. Hamber and C. M. Wu. Perturbative fermion contribution to the average plaquette. *Phys. Lett.*, 127B:119, 1983.

[177] B. Alles, M. Campostrini, A. Feo, and H. Panagopoulos. Lattice perturbation theory by computer algebra: A three loop result for the topological susceptibility. *Nucl. Phys.*, B413:553–566, 1994.

[178] C. T. H. Davies. 1998. private communication.

[179] C. Christou, A. Feo, H. Panagopoulos, and E. Vicari. The three loop beta function of SU(N) lattice gauge theories with wilson fermions. *Nucl. Phys.*, B525:387, 1998.

Danksagung

An erster Stelle möchte ich mich bei meinem Doktorvater Prof. Dr. Klaus Schilling ganz herzlich bedanken. Er hat mich auf ein phenomenologisch sehr interessantes Thema aufmerksam gemacht. Sein ständiges Interesse, seine stete Diskussionsbereitschaft und viele physikalische Ideen waren wesentliche Voraussetzungen für den erfolgreichen Verlauf dieser Arbeit.

Außerordentlich großen Anteil daran hat Dr. Henning Hoeber. Sein Engagement und seine Ideen haben dieses Promotionsprojekt erst möglich gemacht.

In ungezählten Diskussionen mit Dr. Stephan Güsken und Dr. Jochen Fingberg habe ich profitiert von ihrem physikalischen Verständnis und ihrer langjährigen Erfahrung auf dem Gebiet der Gitterphysik.

Besonders bedanken möchte ich mich bei allen Mitgliedern der SESAM-Kollaboration, neben den bereits genannten vor allem bei Dr. Uwe Glässner, Dr. Dr. Thomas Lippert, Dr. Gero Ritzenhöfer und Dr. Gabriele Siegert. Sie haben mich in die Arbeit an dem Computerprojekt der Kollaboration einbezogen zu einem Zeitpunkt, da bereits wesentliche Vorarbeiten geleistet waren und die physikalische Auswertung beginnen konnte.

Großen Dank schulde ich Prof. Dr. Christine Davies, die diese Arbeit mit motivierender Aufmerksamkeit verfolgt hat und deren fachliche Kompetenz auf dem Gebiet der nicht-relativistischen Gitter-QCD mir über viele Probleme hinweghalf.

Weiterhin bin ich dankbar für anregende Diskussionen mit Dr. Arifa Ali Khan, Dr. Gunnar Bali, Dr. Joachim Hein, Dr. Thomas Manke, Prof. Dr. Junko Shigemitsu.

Dr. Armin Wachter danke ich für die Überlassung einiger Routinen zur Berechnung von Wellenfunktionen.

Für die kritische Durchsicht des Manuskripts danke ich Dr. Pierre Lacock und Dr. Mike Peardon. Ihre Anmerkungen haben diese Arbeit entscheidend verbessert.

Herrn Prof. Dr. Achiman möchte ich für die Übernahme des Zweitgutachtens danken.

Für die Überwindung der Fülle kleiner Computerprobleme bedanke ich mich bei Norbert Eicker . Er stand mit Rat und Tat zur Seite und ersparte mir manches Mal das Studium der Manuals. Es ist das Verdienst von Dr. Peer Ueberholz, daß die Wuppertaler CM5 - trotz starker Auslastung - reibungslos funktionierte. Dank geührt ebenfalls den Mitarbeitern des Rechenzentrums der Universität Erlangen, die mir die intensive Nutzung ihrer Connection Machine ermöglichten.

Ich danke der Deutschen Forschungsgemeinschaft für die finanzielle Unterstützung im Rahmen eines Stipendiums des Graduiertenkollegs '*Feldtheoretische und Numerische Methoden in der Elementarteilchen- und Statistischen Physik*' sowie für die Finanzierung der Reisen nach Kopenhagen, Hamburg, München und Schladming.

In gleichem Maße bedanke ich mich für die Förderung durch das Deutsche Elektronen-Synchrotron (DESY), das auch die Teilnahme an den Konferenzen in Edinburgh und Boulder sowie an der Sommerschule in Les Houches ermöglichte.

Ein Dankeschön auch an alle Mitstreiter und ehemaligen Mitstreiter aus F10.06 für die angenehme Arbeitsatmosphäre in den vergangenen drei Jahren: Francisco Alba, Susanne Bielefeld, Thorsten Greiner und Guido Arnold.

Dies ist auch der Zeitpunkt, meinen Eltern Danke zu sagen für ihre große Unterstützung und das Verständnis, welches sie meinen Interessen und meiner Arbeit entgegengebracht haben.

Schließlich möchte ich dem mir wichtigsten Menschen danken, meiner Lebensgefährtin Nuschin Morakkabati. Ihre Zuwendung gibt mir Motivation zur Arbeit und Freude am Leben.

Achim Spitz

Wuppertal, September 1998